X-660-74-368
PREPRINT

NASA TM X- 70808

SOLAR GAMMA RAYS

R. RAMATY
B. KOZLOVSKI
R. E. LINGENFELTER

DECEMBER 1974

GSFC
GODDARD SPACE FLIGHT CENTER
GREENBELT, MARYLAND

For information concerning availability
of this document contact:

Technical Information Division, Code 250
Goddard Space Flight Center
Greenbelt, Maryland 20771

(Telephone 301-982-4488)

SOLAR GAMMA RAYS

R. Ramaty and B. Kozlovsky*
Laboratory for High Energy Astrophysics
NASA-Goddard Space Flight Center
Greenbelt, Maryland, U.S.A.

R. E. Lingenfelter**
Department of Astronomy and Department of Planetary and Space Science
University of California
Los Angeles, California, U.S.A.

* NAS-NRC Resident Research Associate. Present address: Physics Department, Tel Aviv University, Israel.

** Research supported by the National Science Foundation under Grant GP 31620.

Abstract

The theory of gamma-ray production in solar flares is treated in detail. Both lines and continuum are produced. The strongest line predicted at 2.225 MeV with a width of less than 100 eV and detected at 2.24 $\pm$ 0.02 MeV, is due to neutron capture by protons in the photosphere. Its intensity is dependent on the photospheric ^{3}He abundance. The neutrons are produced in nuclear reactions of flare accelerated particles which also produce positrons and prompt nuclear deexcitation lines. The strongest prompt lines are at 4.43 MeV from ^{12}C and at ~6.2 from ^{16}O and ^{15}N. These lines result from both direct excitation and spallation. The widths of individual prompt lines are determined by nuclear kinematics. The width of the 4.43 MeV line is ~100 keV and that of the 6.3 MeV feature is ~300 keV. Both these lines have been observed from a solar flare. Other potentially observable lines are predicted at 0.845 and 1.24 MeV from ^{56}Fe, at 1.63 MeV principally from ^{14}N and ^{20}Ne, at 1.78 MeV from ^{28}Si, at ~5.3 MeV from ^{15}O and ^{15}N, and at 7.12 MeV from ^{16}O. The widths of the iron lines are only a few keV, while those of the other lines are about 100 keV. The only other observed line is at 0.511 MeV from positron annihilation. The width of this line is determined by the temperature, and its temporal variation depends on the density of the ambient medium in the annihilation region. Positrons can also annihilate from the ^{3}S state of positronium to produce a 3-photon continuum below 0.511 MeV. In addition, the lines of ^{7}Li and ^{7}Be at 0.478 keV and 0.431 keV, which have kinematical widths of ~30 keV, blend into a strong feature just below the 0.511 MeV line.

From the comparison of the observed and calculated intensities of the line at 4.4 MeV to that of the 2.2 MeV line it is possible to obtain information on the spectrum of accelerated nuclei in flares. Moreover, from the

absolute intensities of these lines the total number of accelerated nuclei at the Sun and their heating of the flare region can be estimated. We find that about 10^{33} protons of energies greater than 30 MeV were produced in the 1972, August 4 flare.

The gamma-ray continuum, produced by electron bremsstrahlung, allows the determination of the spectrum and number of accelerated electrons in the MeV region. From the comparison of the line and continuum intensities we find a proton-to-electron ratio of about 10 to 10^2 at the same energy for the 1972, August 4 flare. For the same flare the protons above 2.5 MeV which are responsible for the gamma-ray emission produce a few percent of the heat generated by the electrons which make the hard x-rays above 20 keV.

1. INTRODUCTION

Measurements of accelerated charged particles near the Earth clearly indicate that such particles are produced in great profusion in solar flares. These particles consist of both electrons and nuclei. But until the advent of solar gamma-ray astronomy, observations in the radio and x-ray bands had revealed only the existence of the electronic component in the flare region itself. In the hopes of finding some measure of the properties of accelerated protons and heavier nuclei in flares, a variety of theoretical studies of the possible nuclear reactions of such particles in the flare region have been made by Biermann et al. (1951), Morrison (1958), Lapointe (1960), Hess (1962), Chupp (1964), Lingenfelter et al. (1965a,b), Dolan and Fazio (1965), Bland (1966), Lingenfelter and Ramaty (1967), Ito et al. (1968), Kuzhevskii (1968), Ito and Okazoe (1969), Lingenfelter (1969) and Cheng (1972).

In a previous paper (Lingenfelter and Ramaty 1967) we treated in considerable detail the nuclear reactions produced by accelerated charged particles in solar flares and we showed that in large flares these reactions produce detectable lines in the gamma-ray region. We found that the strongest lines should be at 0.5, 2.2, 4.4, and 6.1 MeV resulting from position annihilation, neutron capture on hydrogen, and deexcitation of excited states in ^{12}C and ^{16}O, respectively.

The recent observations by Chupp et al. (1973) of the first gamma-ray lines from solar flares confirm these predictions. During the flash phase of the 1972, August 4 flare all of these lines were observed with relative intensities essentially consistent with our calculations.

Since these observations became available, several additional studies on gamma-ray line production in solar flares have been undertaken: Ramaty and Lingenfelter (1973a) have investigated the consistency of the observations with the theory of nuclear reactions in flares; these authors also considered the effects of positronium formation and neutron propagation in the solar atmosphere (Ramaty and Lingenfelter 1973b); Reppin et al. (1973) treated the time dependence of the 2.2 MeV line; Wang and Ramaty (1974) have done a detailed calculation on neutron propagation and 2.2 MeV line formation and they pointed out the importance of photospheric ^3He as a nonradiative sink for the neutrons; Kozlovsky and Ramaty (1974a) have pointed out that $\alpha\alpha$ reactions produce the ^7Li and ^7Be lines at 478 keV and 431 keV which could be observable from flares; and Suri et al. (1975) have measured the continuum in the gamma-ray region for the 1972, August 4 flare and discussed its significance in terms of two stages of particle acceleration.

In the present paper we wish to summarize the above material and to present updated calculations on the production of gamma rays in solar flares. In Section 2 we define the interaction models that we use in our calculations; in Section 3 we consider neutron production and 2.2 MeV line formation; in Section 4 we consider the production of prompt gamma-ray lines; in Section 5 we treat the continuum emission; in Section 6 we compare the results of Section 3, 4 and 5 with data for the 1972, August 4 flare and we deduce the number and spectrum of accelerated particles at the Sun and the energy that they deposit in the solar atmosphere; in Section 7 we treat problems concerning the formation of

the 0.51 MeV line; in Section 8 we provide estimates for the expected high-energy gamma-ray and neutron fluxes at Earth; and we summarize our results in Section 9. Some of the material contained in the present paper has been recently given in two symposium proceedings (Ramaty and Lingenfelter 1975a,b).

2. INTERACTION MODELS

We consider an interaction volume in which a population of accelerated particles interacts with the ambient medium assumed to be uniform throughout this volume. For the composition of this medium we use the abundances of Cameron (1973). The instantaneous production rate of secondary particles is given by

$$q(E_s,t) = n\int_{o}^{\infty} dE\ N(E,t)\ c\beta\ \sigma(E)\ f(E,E_s) \quad , \tag{1}$$

where n is the number density of the ambient medium, N(E,t) is the instantaneous number of accelerated particles per unit energy per nucleon at time t; E and E_s are the energies per nucleon of the primary and secondary particles; $c\beta$ is the velocity of the primary particles; $\sigma(E)$ is the cross section for the production of secondaries as a function of E; and $f(E,E_s)dE_s$ is the probability that a secondary particle produced by a primary particle of energy per nucleon E will have energy per nucleon in dE_s around E_s.

If we assume that the primary particles are produced in the interaction volume at a rate $\dot{N}(E,t)$, and if they can only lose energy or escape from this volume, then the instantaneous number N(E,t) is related to the source function $\dot{N}(E,t)$ by the continuity equation

$$\frac{\partial N(E,t)}{\partial t} + \frac{\partial}{\partial E}\left[\dot{E}(E,t)\ N(E,t)\right] + \frac{1}{t_1}\ N(E,t) = \dot{N}\ (E,t), \tag{2}$$

where $\dot{E}$ is the rate of energy loss and t_1 is the mean escape time. Both these functions can depend on energy and time, but we shall assume that they are only energy dependent. The solution of equation (2) can then be written as

$$N(E,t) = \dot{E}^{-1}\int_{E}^{\infty} dE'\ \dot{N}\left[E',t'\right]\ \exp\left[-\int_{E}^{E'} \frac{1}{T}\frac{dE''}{\dot{E}(E'')}\right], \tag{3}$$

where

$$t' = t - \int_{E}^{E'} \frac{dE''}{\dot{E}(E'')} \tag{4}$$

(e.g. Syrovatkii 1959, Lingenfelter and Ramaty 1967)

Equation (3) can be reduced to simpler forms in two limiting cases. In the thin-target model, the particles escape rapidly from the interaction volume. For this model to be valid, the escape time has to be sufficiently short so that $\dot{N}$ does not vary appreciably over a time interval of order t_1 and an energy interval from E' to E, where E'-E is the energy lost during t_1. Also $T\dot{E}$ must remain essentially constant from E' to E. Equation (3) can then be written as

$$N(E,t) = t_1(E)\ \dot{N}(E,t). \tag{5}$$

In the thick-target model the particles lose energy and stop in the interaction volume, i.e. $t_1 \gg t - t'$ at all energies of interest. Equation (3) then simplifies to

$$N(E,t) = \dot{E}^{-1} \int_{E}^{\infty} dE'\ \dot{N}(E',t'), \tag{6}$$

where t' is given by equation (4).

We can now substitute equations (5) or (6) into equation (1). For the thin-target model we obtain

$$q(E_s,t) = n \int_{0}^{\infty} dE\ c\beta\sigma(E)\ f(E,E_s)\ t_1(E)\ \dot{N}(E,t), \tag{7}$$

while for the thick-target model we get

$$q(E_s,t) = n \int_{0}^{\infty} dE\ c\beta\sigma(E)\ f(E,E_s)\ \dot{E}^{-1} \int_{E}^{\infty} dE'\ \dot{N}(E',t'). \tag{8}$$

Since equation (7) is of the same form as equation (1) which is the more general of the two, we shall use the latter in our subsequent calculations

for thin-targets. If the conditions for a thin target are fulfilled, we can relate, by equation (5), the instantaneous spectrum N(E) to the source spectrum $\dot{N}(E)$. But even if these conditions are not satisfied, we can still use the thin-target calculations provided that N is interpreted only as the instantaneous number of accelerated particles in the interaction region.

Equation (8) can be further simplified by considering the time-integrated production rate

$$Q(E_s) = \int_{-\infty}^{\infty} q(E_s,t) = n \int_0^{\infty} dE c\beta\sigma(E) f(E,E_s) \dot{E}^{-1} \int_E^{\infty} dE' \bar{N}(E'), \qquad (9)$$

where

$$\bar{N}(E') = \int_{-\infty}^{\infty} dt' \dot{N}(E',t'). \qquad (10)$$

Because the inner integral in equation (9) is just the integral spectrum of $\bar{N}(E)$, we have

$$Q(E_s) = A \int_0^{\infty} dE \frac{dx}{dE} \sigma(E) f(E,E_s) \bar{N}(>E). \qquad (11)$$

where $\frac{dE}{dx} = \dot{E}A/(\pi c\beta)$, and A is Avogadro's number. If we are not interested in the energy of the secondary particle we can integrate both equations (1) and (11) over E_s. This yields

$$q = n \int_0^{\infty} dE \, c\beta\sigma(E) \, N(E) \qquad (12)$$

and

$$Q = A \int_0^{\infty} dE \frac{dx}{dE} \sigma(E) \bar{N}(>E) \qquad (13)$$

We shall use equations (12) and (13) in our subsequent calculations of nuclear reactions where we do not need the energy of the secondary particles. In the thin-target formula (12), N(E) is the instantaneous number of accelerated particles in the interaction region per unit

energy per nucleon at E. In the thick-target formula (13), $\bar{N}$ (>E) is the total number of accelerated particles of energies per nucleon greater than E that stop in the interaction region. For both N(E) and $\bar{N}$ (>E) we use power-law and exponential spectra. These are

$$N_i(E) \text{ or } \bar{N}_i(E) = (k_i \text{ or } \bar{k}_i)\, E^{-s} \tag{14}$$

and

$$N_i(>E) \text{ or } \bar{N}_i(>E) = (k'_i \text{ or } \bar{k}'_i)\, \exp(-P/Po). \tag{15}$$

Here i denotes the chemical or isotopic species of the particles; P is particle rigidity; the k's are constants determined by normalizing the particle numbers to 1 proton of energy greater than 30 MeV, using the composition of the ambient solar atmosphere; and s and Po are, respectively, the spectral index and characteristic rigidity assumed to be the same for all charged particle components.

Before proceeding with the calculations, we wish to comment on the assumed abundances for both the accelerated particles and the ambient medium. As we shall see, the prompt deexcitation lines are produced mainly by reactions induced by protons. Hence their intensities relative to each other depend on the relative abundances of nuclei with A≥12 (mainly ^{12}C and ^{16}O), and these are reasonably well known in the solar atmosphere. Neutron production, however, depends strongly on the helium abundance. From the data of Cameron (1973) we have that He/H = 0.069 and He/(C+N+O) = 60. If the abundance of He relative to both H and CNO is larger, then more neutrons, and 2.2 MeV photons, are produced relative to the prompt lines than indicated by our calculations. In particular if He/H = 0.1, the intensity of the 2.2 MeV line relative to that of the 4.4 MeV line will be increased by about 40%.

3. Neutron and 2.23 MeV Gamma Ray Production

Neutron production by accelerated charged particles was treated by Lingenfelter et al. (1965a) and Lingenfelter and Ramaty (1967). In the present paper we have updated the cross sections used by these authors and we have added data at low energies including α-particle induced reactions.

The most important neutron producing reactions and their threshold energies are listed in Table 1. The cross sections for reaction (1) are the same as given by Lingenfelter and Ramaty (1967). Below the multiple π production threshold these cross sections are obtained by subtracting from the total proton-proton inelastic cross section (Hess 1958) the cross section for the reaction $^1H(p,\pi^+)^2H$ (see Ramaty and Lingenfelter 1969). At higher energies, the neutron production cross section is assumed to be

$$\sigma_{pp} = (2 - k_p)\ \sigma_{pp}^{inelas}, \tag{16}$$

where σ_{pp}^{inelas} is the total inelastic cross section, approximately equal to a constant at 27 mb at these energies, and k_p is the proton multiplicity having approximately a constant value of 1.25 (see Lingenfelter and Ramaty 1967).

The cross sections for the reactions (2) are from Meyer (1972). Above a few hundred MeV, these reactions include also the formation of pions. The cross sections for reactions (3), (4), (5) and (6) above about 15 MeV are from Lingenfelter and Ramaty (1967). At lower energies most of the neutrons from proton induced processes are from the reactions $^{13}C(p,n)^{13}N$, $^{18}O(p,n)^{18}F$, $^{14}N(p,n)^{14}O$, and $^{56}Fe(p,n)^{56}Co$ which have very

low threshold energies. The cross sections for these reactions are from Gibbons and Macklin (1959), Bair (1973), Audouze et al. (1967), and Tanaka and Furukawa (1959). The cross sections for the fusion reaction (8) were summarized by Kozlovsky and Ramaty (1974b).

The cross section for (α,n) reactions on ^{12}C, ^{13}C, ^{18}O, ^{22}Ne, ^{25}Mg, ^{26}Mg and ^{29}Si are known experimentally at low energies. The cross section for $^{12}C(\alpha,n)^{15}O$ is from Nelson et al. (1963); the cross section for ^{13}C $(\alpha,n)^{16}O$ was taken from Walton et al. (1957), Sekharan et al. (1967), and Bair and Haas (1973); the cross section for $^{18}O(\alpha,n)^{21}Ne$ is from Bair and Willard (1962) and Bair and Haas (1973); the cross section for $^{22}Ne(\alpha,n)^{25}Mg$ is from Ashery (1969) and from Haas and Bair (1973); the cross section for $^{26}Mg(\alpha,n)^{29}Si$ is from Bair and Willard (1962) and we assumed the same cross section for $^{25}Mg(\alpha,n)^{28}Si$; the cross section for $^{29}Si(\alpha,n)^{32}S$ is from Gibbons and Macklin (1959). There are no data for the reactions $^{14}N(\alpha,n)^{17}F$, $^{16}O(\alpha,n)^{19}Ne$, and $^{20}Ne(\alpha,n)^{23}Mg$. By assuming that these reactions have the same cross sections as that of the reaction $^{12}C(\alpha,n)^{15}O$ (Nelson et al. 1963), we find that (α,n) reactions on ^{14}N and ^{16}O do not contribute significantly to neutron production in any energy region. The reaction $^{16}O(\alpha,pn)^{18}F$ for which the cross section was measured by Furukawa and Tanaka (1961) does contribute significantly to neutron production by incident α-particles of about 10 MeV/nucleon.

The cross section for the reaction $Fe(\alpha,n)$ was estimated theoretically. Above the threshold for this reaction the emission of neutrons becomes the dominant reaction and therefore $\sigma(\alpha,n) \simeq \sigma_c(\alpha)$

where $\sigma_c(\alpha)$ is the cross section for forming the compound nucleus with an alpha particle. For Fe the value of $\sigma_c(\alpha)$ in the few MeV/nucleon range can be obtained by using the continuum theory (Blatt and Weisskopf 1952). Our numerical values are from Blatt and Weisskopf's Table 4.1 (p.353), averaged for $r_o = 1.3 \times 10^{-13}$ and 1.5×10^{-13}cm.

The resultant cross sections are given in Figure 1 as functions of energy per nucleon E. Here pp, pα, $\alpha\alpha$, pCNO and αCNO indicate neutron production in proton-hydrogen, proton-helium, alpha particle-helium, proton-heavy nuclei, and α particle-heavy nuclei reactions, respectively. The pCNO and αCNO cross section are defined as

$$\sigma_{pCNO} = \sum_i \sigma_{pi} \left[\frac{n_i}{\Sigma n_k} \right] \tag{17}$$

$$\sigma_{\alpha CNO} = \sum_i \sigma_{\alpha i} \left[\frac{n_i}{\Sigma n_k} \right] , \tag{18}$$

where n_i is the abundance of isotope i; σ_{pi} and $\sigma_{\alpha i}$ are the cross sections for neutron production by protons and alpha particles on isotope i; and the summations are over all isotopes equal to or heavier than ^{12}C. The cross sections for the inverse reactions αp, CNOp and CNOα are the same as those for the direct reactions at the same energy per nucleon.

The instantaneous neutron production rates in the thin-target model for power-law and exponential spectra are shown in Figures 2 and 3, respectively. The various production modes are: pp (proton-hydrogen), pα (proton-helium), αp (α particle-hydrogen), $\alpha\alpha$ (α particle-helium), pCNO (proton-heavy nuclei), CNOp (heavy nuclei-hydrogen), αCNO (α particle-heavy nuclei), and CNOα (heavy nuclei-helium). As can be seen for flatter spectra (smaller values of s or larger values of P_o) the

neutrons are produced mainly in pα, pp and αp reactions. For power-law spectra (Figure 2) neutron production at large values of s is mainly due to αCNO and CNOα reactions; the contribution of pCNO and CNOp reactions is small at all values of s ; and αα reactions make a major contribution around s=4. For exponential spectra, (Figure 3) almost all of the neutrons are produced in pα reactions at values of Po≥25 MV. In this case the relative contributions of reactions induced by α-particles and heavy nuclei are lower than for power-law spectra. Because particles with $Z \geq 2$ have larger rigidities than protons, it follows from equation (15) that their fluxes relative to the proton flux at the same energy per nucleon is lower than in the power-law case given by equation (14). Since the nuclear cross sections are the same for the direct and inverse reactions at the same energy per nucleon, for particle spectra which are exponential in rigidity more neutrons are produced by a proton induced reaction than by the corresponding inverse process.

The total neutron production rates in the thin-target model, q, and the total neutron yields in the thick-target model, Q, are shown in Figure 4 for power-law and exponential spectra. In the thin-target model, for flat primary spectra the neutron production rates are about the same for the exponential and power-law cases. This result is due simply to the fact that for such spectra most of the neutrons are produced in pα reactions with effective threshold around 30 MeV/nucleon and all of the assumed spectra are normalized of 1 proton above this energy. But because a power-law spectrum contains a much larger number of low-energy particles than an exponential spectrum with this same normalization, the steep power-law spectrum can yield orders of magnitude more neutrons

from αCNO and CNOα reactions which have thresholds more than an order of magnitude below 30 MeV/nucleon.

Similar effects are evident also in the thick-target model except that here the relative contribution of the low-energy particles in general is diminished because of their shorter range.

Having considered the production of neutrons, let us now discuss their propagation and the ensuing gamma-ray line production. Wang and Ramaty (1974) considered in detail the effects of neutron propagation in the solar atmosphere on the production of gamma rays by the reaction

$$n + p \rightarrow d + \gamma. \qquad (19)$$

In their treatment a distribution of neutrons was released in the chromosphere or corona, and the path of each neutron after its release was followed by a computer Monte-Carlo simulation. If the neutrons are released above the photosphere, any initially upward moving neutron escapes from the Sun. Some of the downward moving neutrons can also escape after being backscattered elastically by ambient protons, but most of these neutrons either are captured or decay at the Sun. Because the probability for elastic scattering is much larger than the capture probability, the majority of the neutrons are thermalized before they get captured. Since the thermal speed in the photosphere (where most of the captures take place) is much smaller than the speed of light, the gamma-rays from reaction (19) are essentially at at 2.225 MeV and the Doppler-broadened width of this line is negligible ($\lesssim$ 100 eV).

The bulk of neutrons at the Sun are captured either on H or on ^{3}He.

Whereas capture on H yields a 2.2 MeV photon, capture on ^{3}He proceeds via the radiationless transition

$$n + {}^3\mathrm{He} \rightarrow {}^3\mathrm{H} + p, \tag{20}$$

and hence produces no photons. The cross sections for reactions (19) and (20) are $2.2 \times 10^{-30}\ \beta^{-1}\ \mathrm{cm}^2$ and $3.7 \times 10^{-26}\beta^{-1}\mathrm{cm}^2$, respectively, where β is the velocity of the neutron (for details see Wang and Ramaty 1974). Thus, if the ^{3}He/H ratio in the photosphere is $\sim 5 \times 10^{-5}$ comparable to that observed in the solar wind, nearly equal numbers of neutrons are captured on ^{3}He as on H.

The results of the Monte-Carlo calculations of Wang and Ramaty (1974) are presented in Figures 5 and 6 for two assumptions on the photospheric ^{3}He abundance: $^3\mathrm{He/H} = 0$ and $^3\mathrm{He/H} = 5 \times 10^{-5}$. In these calculations an isotropic distribution of monoenergetic neutrons of energy E_n is released above the photosphere. The solid lines are the probabilities for the various indicated processes. As can be seen, the capture and loss probabilities increase with increasing energy, because higher energy neutrons penetrate deeper into the photosphere. This reduces their escape probability and leads to a shorter capture time, thereby reducing the decay probability. When $^3\mathrm{He/H} = 5 \times 10^{-5}$, the probability for loss on ^{3}He almost equals the capture probability on protons. The escape probability is greater than 0.5, because all initially upward moving neutrons escape from the Sun. Note that the sum of all probabilities equals 1.

The dashed lines in Figures 5 and 6 are photon yields per neutron, $f(\theta, E_n)$, as a function of E_n for various gamma-ray emission angles, θ, between the

earth-sun line and the vertical to the solar surface.

At low neutron energies and θ near zero, f is close to the capture probability on protons. This means that gamma rays from low-energy neutrons observed close to the vertical escape essentially unattenuated from the Sun. At higher energies and at larger angles, however, there is significant attenuation of the gamma rays due to Compton scattering in the photosphere. Even though f does depend on θ, for flares sufficiently close to longitude and latitude zero on the Sun we can neglect its angular dependence. This approximation is quite valid for the flare of 1972, August 4 since its longitude and latitude were E08 and N14.

Using Figures 5 and 6, Wang (1975) has evaluated the average photon yield per neutron, $\bar{f}$, by integrating $f(E_n)$ over the neutron production energy spectra of the various interaction models discussed above. Such neutron spectra were evaluated by Lingenfelter and Ramaty (1967). Recently, Wang (1975) has revised these calculations, and some of his results are shown in Figure 7 and 8. The values of $\bar{f}$ obtained by using these spectra are shown in Figure 9. The upper and lower 4 curves are for $^3He/H = 0$ and $^3He/H = 5 \times 10^{-5}$, respectively. In terms of these average photon yields per neutron, the average 2.2 MeV photon flux at Earth in the thin-target model, ϕ, and the total 2.2 MeV photon flux $\bar{\phi}$ in the thick-target model are given by

$$\phi_{2.2} = q\bar{f}/(4\pi R^2) \tag{21}$$

and

$$\bar{\phi}_{2.2} = Q\bar{f}/(4\pi R^2) \tag{22}$$

where R = 1 A.U.

We finally note that equation (21) is valid for the average neutron flux only, because the instantaneous 2.2 MeV flux lags behind the instantaneous neutron production rate. This lag is almost entirely due to the finite neutron capture time in the photosphere. Wang and Ramaty (1974) have investigated this effect, and some of their results are given in Table 2. Here $\langle n \rangle$ is the most probable density in the photosphere where the captures take place, τ_c is the mean capture time, and τ_d is the neutron decay mean life. In terms of the parameter $\lambda = \tau_c^{-1} + \tau_d^{-1}$, the time profile of the 2.2 MeV photon flux from a monoenergetic burst of neutrons released at t_o can be approximated (Wang and Ramaty 1974) by

$$\phi \text{ (2.2 MeV)} \propto \exp[-\lambda(t-t_o)]. \qquad (23)$$

4. Prompt Gamma Ray Lines

The various prompt gamma-ray lines that can be produced in solar flares are listed in Table 3. These lines result from the deexcitation of nuclear levels in isotopes which either are abundant in the solar atmosphere or are easily produced in nuclear reactions of energetic protons and alpha particles with the abundant constituents. Since ^{1}H, ^{3}He and ^{4}He have no excited states which decay mainly by γ-emission (Meyerhof and Tombrello 1968, Kozlovsky and Ramaty 1974c), the first group of nuclei consists of the isotopes ^{12}C, ^{14}N, ^{16}O, ^{20}Ne, ^{24}Mg, ^{28}Si, ^{56}Fe; the second group is comprised of isotopes such as ^{6}Li, ^{7}Li, ^{7}Be, ^{10}B, ^{11}B, ^{11}C, ^{13}C, ^{15}N. In order to determine the strongest lines which might be expected, we considered laboratory experiments in which line emission was directly observed from proton and α-particle bombardment of targets which are abundant in the solar atmosphere. Such experiments were done by Clegg et al. (1961), Foley et al. (1962), and Zobel et al. (1965, 1968) for ^{12}C, ^{14}N, ^{16}O, ^{24}Mg and ^{56}Fe targets, and incident protons and α-particles in the energy range from about 10 MeV to 150 MeV which essentially includes all solar flare particle energies of interest. All the lines in Table 3, except the lines at 0.431 and 0.478 MeV, have been observed in the laboratory. These latter two lines have been inferred theoretically from the existence of bound states in ^{7}Li and ^{7}Be which decay by γ-emission and which can be produced in $\alpha\alpha$ reactions (Kozlovsky and Ramaty 1974a).

The cross sections for the reactions $^{12}C(p,p')^{12}C^{*4.43}$, $^{12}C(\alpha,\alpha')^{12}C^{*4.43}$, $^{16}O(p,p')^{16}O^{*6.14}$, and $^{16}O(\alpha,\alpha')^{16}O^{*6.14}$ are given in Figure 10. The

cross sections for the proton induced reactions were summarized by Lingenfelter and Ramaty (1967). The cross sections for the reaction $^{12}C(\alpha,\alpha')^{12}C^{*4.43}$ were taken from the measurements of Correlli et al. (1959), Yavin and Farwell (1959), Mitchell et al. (1964), Morgan and Hobbie (1970), Fawzi (1972) and Smith et al. (1973). The cross sections for the reaction $^{16}O(\alpha,\alpha')^{16}O^{*6.14}$ were taken from Correlli et al. (1959), Yavin and Farwell (1959), Harvey et al. (1964), Blatchley and Bent (1965), and Bergman and Hobbie (1971).

Excited levels in nuclei can be populated not only by direct excitation reactions such as those discussed above, but also by spallation reactions in which protons and α-particles break up heavier nuclei into lighter fragments that emerge from the reaction in excited states. In particular, the level $^{12}C^{*4.43}$ can be populated by the reaction $^{16}O(p,p\alpha)^{12}C^{*4.43}$. The cross section for this reaction, measured by Zobel et al. (1968), is given by the dashed line in Figure 10. As can be seen, above about 30 MeV this cross section is greater than the direct excitation cross section. Because in the solar atmosphere ^{16}O is about twice as abundant as ^{12}C, spallation of ^{16}O makes a very important contribution to 4.43 MeV photon production.

By using these cross sections and the interaction models discussed above, we have calculated the production rates of $^{12}C^*$ and $^{16}O^*$. We must distinguish, however, between reactions induced by accelerated protons or α-particles, and reactions induced by accelerated heavy nuclei. For the former, the Doppler widths of the lines are small ($\sim$ 100 keV), but for the latter the lines are significantly broadened by the motion of

the excited fast nucleus which has lost little kinetic energy in the interaction. Because these lines are so broad that they cannot be resolved from the background with presently available instrumentation, in our treatment we consider the line intensities from proton and α-particle induced reactions only.

The production rates of $^{12}C^{*4.43}$ and $^{16}O^{*6.14}$ in the thin-target model are shown in Figures 11 and 12 for power law and exponential spectra, respectively. We see that for flat spectra, these lines are produced mainly by proton induced reactions, whereas for steep spectra (large values of s), the contributions of the α-particles becomes important. For exponential spectra, proton-induced reactions are the principle source of the excited states at all values of $P_o \geq 25$ MV.

The $^{12}C^{*4.43}$ production due to spallation reactions are also shown in Figures 11 and 12. As seen, these reactions make an important contribution to the total production for essentially all spectra except steep power laws for which the low-threshold direct excitation reactions are the main source of the excited states.

The ratio of the total production of the level $^{12}C^{*4.43}$ to the neutron production is shown in Figure 13 for both the thin and thick-target models as a function of s, for power-law spectra, and P_o, for exponential spectra. As can be seen, for exponential spectra in both the thin and thick-target models $^{12}C^{*4.43}/n$ decreases with increasing P_o. This results from the increase of the neutron production cross section with increasing energy as opposed to the decrease of the excitation cross sections (compare Figures 1 and 10). The same behavior can be

seen for power-law spectra for s smaller than about 4.5 in the thin-target model, and s less than about 6 in the thick-target model. For larger values of s, $^{12}C^{*4.43}/n$ decreases with increasing s because these neutrons are produced mainly in αCNO and CNOα reactions which have lower thresholds than those for prompt gamma-ray production.

The 4.4 and 6.2 MeV lines are the most intense prompt lines and the only prompt lines so far observed for a solar flare. In Table 3 we list the approximate expected intensities relative to the line at 4.43 MeV of the various other gamma-ray lines which might be observed during flares. The most intense of these are the lines at 431 and 478 keV from $^{7}Be^{*}$ and $^{7}Li^{*}$. The cross section for ^{7}Li production in $\alpha\alpha$ reactions is shown in Figure 14 (Kozlovsky and Ramaty 1974b). The cross section for $^{7}Li^{*}$ production is about half of the total ^{7}Li production independent of energy. Similarly, the cross section for $^{7}Be^{*}$ should also be about half of the total ^{7}Be production; and because ^{7}Be and ^{7}Li are produced by mirror reactions their production cross sections should be about equal, even though no data for ^{7}Be production in $\alpha\alpha$ reactions is available.

Using these cross sections we find that the intensities of the lines at 478 keV and 431 keV are approximately the same as the intensity of the 4.43 MeV line. Their Doppler widths, however, are about 30 keV (Kozlovsky and Ramaty 1974a); therefore, they should not be observed individually but rather as a broad spectral feature. Because of this reason and the higher continuum emission around 0.5 MeV, it is more difficult to observe these lines than the 4.43 MeV line.

The gamma-ray lines at 0.72, 1.99, 3.62, 3.84, 5.3, 6.33, and 6.7 MeV listed in Table 2 are produced by spallation reactions. We have used the relative cross sections of Clegg et al. (1961), Foley et al. (1962) and Zobel et al. (1965, 1968)

to scale the intensities to the spallation-produced contribution of the 4.43 MeV line at P_o = 150 MV assuming similar energy dependences of the excitation functions. Similarly, for the lines at 0.845, 1.24, 1.38, 1.78, 2.75 and 7.12 MeV, which are produced by direct excitation, we have used the cross sections of Zobel et al. (1968) and McGowan et al. (1969, 1970) to scale the intensities to the direct excitation contribution of the 4.43 MeV line.

The 1.63 MeV line results from both direct excitation and spallation reactions. The cross section for the reactions $^{20}Ne(p,p')^{20}Ne^{*1.63}$ and $^{14}N(p,p')^{14}N^{*3.94}$ are about 0.5 and 0.15 times the $^{12}C^{*4.43}$ direct excitation cross section, respectively (Oda et al. 1960, Ascuito 1972), and the 3.94 MeV level decays 96% of the time to the 2.31 MeV level. The cross sections for the spallation reactions on ^{16}O and ^{24}Mg which also lead to 1.63 MeV photons are from Zobel et al. (1965, 1968).

The 2.31 MeV line also results from a variety of processes. The 2.31 MeV level in ^{14}N can be populated both by the decay of ^{14}O (99.4% of the time) and $^{14}N^{*3.94}$. The cross section for producing the positron emitter ^{14}O is discussed in Section 7, and the cross section for the excitation of the 3.94 MeV level in ^{14}N was discussed above. The cross section for the direct excitation of the 2.31 MeV level is about 5 to 10% of that of the 3.94 MeV level (Oda et al. 1960), The cross section for the reaction $^{16}O(p,2pn)^{14}N^{*2.31}$ is given by Zobel et al. (1968). Combining all the above processes, we find that the contribution of ^{14}O is about 70% of the total. We note that since the half life of ^{14}O is 70.5 sec, the 2.31 MeV line is delayed with respect to the other prompt lines of Table 3.

In summary, Table 3 shows the most important prompt gamma-ray lines that could be observed from solar flares. The most prominent line is that at 4.4 MeV, but because Doppler broadening of the 6.14 MeV and 6.33 MeV lines makes them essentially indistinguishable, a feature at ~6.2 MeV could be as intense as the 4.4 MeV line. Its width, however, is about 300 keV, while the Doppler width of the 4.4 MeV line is only ~100 keV. The lines at 0.43 MeV and 0.48 MeV are also quite intense, but because of their larger relative Doppler widths (~30 keV) and higher underlying continuum emission, these lines are more difficult to observe. The line at 2.31 MeV, even though close to the 2.225 MeV line, makes a negligible contribution to line emission at this energy (~3%). The iron lines at 0.85 and 1.24 MeV turn out to be surprisingly strong. These lines should be relatively easy to observe with a high resolution detector, since their Doppler widths are only a few keV.

5. Continuum Emission

The radiation mechanisms that can produce continuum emission in the x-ray and gamma-ray regions are bremsstrahlung, Compton scattering and synchrotron radiation but the latter two are not important in solar flares. The magnetic field in flares are not expected to be larger than about 1000 gauss and the energies of the accelerated electrons do not exceed about 100 MeV. Therefore, synchrotron radiation is not expected to produce photons of frequencies greater than a few times 10^{13}Hz and hence this mechanism is unimportant in the x-ray and gamma-ray regions.

Similarly, Compton scattering (Shklovsky 1965) is also not an important radiation mechanism, as can be seen from the following argument. In the solar atmosphere, the largest energy density in radiation fields is that due to the photospheric emission at $T \sim 6000$°K. Since the energy density in this field close to the photosphere is only about 1 erg cm^{-3} which is only a fraction of a percent of the energy density in flare magnetic fields, any accelerated electron will lose at least 100 times more energy by synchrotron emission than by Compton scattering. The synchrotron energy loss is observable in the microwave region. If the energies of the accelerated electrons are smaller than about 100 MeV, the Compton scattered photons will have energies below $\sim$ 20 keV; since the measured energy flux in these x-rays is much larger than that observed in the microwave region, only a very small fraction of this flux can be due to Compton scattering of visible photons. Another possible Compton process would be the scattering of x-rays below about 20 keV into the gamma-ray

region by electrons of a few MeV. But the energy density in these x-rays is smaller than in the visible radiation ($\sim 10^{-2}$ erg cm^{-3} for the 1972, August 4 flare, Dere et al. 1973). Hence also in this case the Compton losses are quite negligible.

We consider now the production of bremsstrahlung in solar flares. In the nonrelativistic region, most of the radiation is produced by the interaction of accelerated electrons with ambient ions. The inverse process, in which accelerated protons interact with ambient electrons has also been considered (Boldt and Serlemitsos 1969). If the accelerated protons have the same velocity as the accelerated electrons, proton-electron bremsstrahlung has the same cross section as electron-proton bremmstrahlung. But for the one flare (1972, August 4) for which we know the proton flux from the gamma-ray observations, it turns out that bremsstrahlung due to proton-electron interaction is negligible in comparison with that due to electron-proton interactions.

Bremsstrahlung can also be produced in electron-electron interactions. This process is negligible in the nonrelativistic region but becomes comparable to electron-proton bremmstrahlung in the relativistic domain (Akhiezer and Berestetskii 1965).

The differential cross section for electron-proton bremsstrahlung is given by (Heitler 1954, Koch and Motz 1959)

$$\frac{d\sigma}{d\epsilon}(\gamma,\epsilon) = \alpha r_o^2 \frac{p'}{p\epsilon} \cdot \left\{ \frac{4}{3} - 2\gamma\gamma' \left(\frac{p^2 + p'^2}{p^2 p'^2} \right) + \frac{k\gamma'}{p^3} + \frac{k'\gamma}{p'^3} - \frac{kk'}{pp'} + \right.$$
$$\left. + L \left[\frac{8}{3} \frac{\gamma\gamma'}{pp'} + \frac{\epsilon^2 (\gamma^2\gamma'^2 + p^2 p'^2)}{p^3 p'^3} + \frac{\epsilon}{2pp'} \left(k \frac{\gamma\gamma' + p^2}{p^3} - k' \frac{\gamma\gamma' + p'^2}{p'^3} + \frac{2\epsilon\gamma\gamma'}{p^2 p'^2} \right) \right] \right\}, \quad (24)$$

where ϵ and γ are the photon energy and initial electron energy, respectively, both in units of the electron rest mass energy,

$\gamma' = \gamma - \epsilon$, $p = (\gamma^2-1)^{1/2}$, $p' = (\gamma'^2-1)^{1/2}$,

and

$$L = 2 \ln\left[\frac{\gamma\gamma'+pp'-1}{\epsilon}\right]; \quad k = \ln\left(\frac{\gamma+p}{\gamma-p}\right); \quad k' = \ln\left(\frac{\gamma'+p'}{\gamma'-p'}\right). \tag{25}$$

The instantaneous photon production rate per unit photon energy ϵ is given by an equation similar to equation (1),

$$q(\epsilon) = n \int dE\ N(E)\ c\beta\ \frac{d\sigma}{d\epsilon}(E,\epsilon), \tag{26}$$

where E is the kinetic energy of the electron. This equation has been evaluated numerically (T. Bai, private communication 1974) assuming a power-law kinetic energy spectrum given by equation (14) and the results are presented in Figure 15 for various spectral indexes s. This figure is for electron-proton bremsstrahlung only. In the subsequent section we shall add the bremsstrahlung due to electron-helium interactions, which, for an assumed He/H ratio of 0.07, increases $q(E)$ by a factor of 1.28. In the nonrelativistic region $q(E)$ can be approximated by a power-law proportional to $E^{-s-0.5}$. In the ultrarelativistic region $q(E)$ is proportional to $E^{-s+0.1}$.

6. Accelerated Particles at the Sun

The energy spectrum of the accelerated nuclei at the Sun can be deduced by comparing the calculated and observed ratios of the intensities of the strongest prompt line at 4.43 MeV to that of the neutron capture line at 2.225 MeV; and the total number of accelerated nuclei can be obtained by comparing the calculated and observed absolute intensities of these lines. The energy spectrum and total number of the accelerated electrons can be obtained by comparing the observed x- and gamma-ray continuum fluxes with the calculated bremsstrahlung intensities. Let us first consider the nuclei.

The ratio of the intensities of the 4.4 MeV and 2.2 MeV lines is given by

$$\frac{\phi_{4.4}}{\phi_{2.2}} = \left(\frac{^{12}C^{*4.43}}{n} \right) (\bar{f})^{-1} \qquad (27)$$

where $(^{12}C^{*4.43}/n)$ is the ratio of the yield of the excited nucleus $^{12}C^{*4.43}$ to the neutron yield shown in Figure 13, and $\bar{f}$ is the 2.2 MeV photon yield per neutron given in Figure 9. By combining these two figures, we can calculate $\phi_{4.4}/\phi_{2.2}$ from equation (27). The results are plotted in Figures 16 and 17, for $^3He/H = 0$ and $^3He/H = 5\times10^{-5}$, respectively. The results of Figure 16 differ only slightly from those of Figure 10 of Ramaty and Lingenfelter (1975a,b) who have used a constant value for the 2.2 MeV photon yield per neutron ($f = 0.2$) instead of the model-dependent results of Figure 9.

Let us compare now the calculations with the data. The observed (Chupp et al. 1975) $\phi_{4.4}/\phi_{2.2}$ ratio of 0.11 ± 0.04 for the 1972, August 4 flare is also shown in Figures 16 and 17. As can be seen, assuming power-law spectra for the particles in the flare region, their spectral index s

should lie between the values of 1.9 ± 0.2 deduced for the thin-target model and 3 ± 0.3 for the thick-target model if there is no ^{3}He in the photosphere; or between 1.7 ± 0.2 and 2.7 ± 0.3 for these models if the photospheric ^{3}He/H ratio is 5×10^{-5}. Similarly, assuming exponential spectra, the implied P_o's should lie between 110 ± 30 MV for the thick-target model and 170 ± 50 MV for the thin-target model if ^{3}He/H = 0; or between 165 ± 55 MV and 250 ± 80 MV for these models if ^{3}He/H = 5×10^{-5}. These spectral parameters are summarized in Table 4. Note, however, that these implied spectra become somewhat steeper if we use a larger He abundance, since, as discussed in Section 2, this increases the neutron production without changing the $^{12}C^{*4.43}$ yield.

Knowing the spectral index for the various models, we can now deduce the total number of protons at the Sun. In Figures 18 and 19 we show the instantaneous and total 2.2 MeV fluxes for these models, for ^{3}He/H = 0 and ^{3}He/H = 5×10^{-5}, respectively. These figures are obtained from equations (21) and (22), where q, Q and $\bar{f}$ are from Figures 4 and 9.

In the thick-target model the time-integrated photon flux from the flare determines the total number of accelerated particles that interact and stop at the Sun. According to Chupp et al. (1975), the 2.2 MeV intensity for the 1972, August 4 flare was about 0.3 photons cm^{-2} s^{-1}. This flux is the average over the time interval of observation (0623 to 0633 UT) which gives a total flux of about 180 photons cm^{-2}. Since the detector on OSO-7 was eclipsed by the Earth before the termination of the gamma-ray event, this is a lower limit to the total flux from the flare. If we assume a duration of $\sim10^3$ seconds for the event, as indicated by the hard x-ray data (van Beek et al. 1973), then the total flux of 2.2 MeV photons was ~300 cm^{-2}. Then from Figure 18 we find that $\bar{N}_p(>30\text{ MeV}) = 8\times10^{32}$ for s = 3, and $\bar{N}_p(>30\text{ MeV}) = 1.0\times10^{33}$ for P_o = 110 MV. The corresponding values for ^{3}He/H = 5×10^{-5}

are about the same, because the effect of a lower $\bar{f}$ is approximately cancelled by a higher neutron yield. Therefore, the total number of protons above 30 MeV released downward into the Sun in the thick-target model is about 10^{33} independent of the spectral form or the ^{3}He/H ratio.

For the thin-target model, the instantaneous gamma-ray observations determine the product of the ambient proton or hydrogen density, n_H, and the instantaneous number of the accelerated particles in the interaction region. From Figure 18 we obtain that $n_H N_p$ (>30MeV) $\simeq 5 \times 10^{43}$ cm^{-3} for s = 1.9, and $n_H N_p$ (>30MeV) $\simeq 8 \times 10^{43}$ cm^{-3} for P_o = 170MV. As before, these values are not significantly effected by the photospheric ^{3}He/H ratio.

We consider now the electrons. The observed x and gamma-ray continuum flux for the 1972, August 4 flare is shown in Figure 20. The lower and upper envelopes of the shaded region are the best fits to the observed x-ray flux at about 0626UT and 0630UT, respectively (van Beek et al. 1973). The data points are from Suri et al. (1975) and they represent the average gamma-ray flux over the time interval 0623UT to 0633UT. Thus, even though the x-ray and gamma-ray spectra were observed by different detectors on different satellites, the observation times were about the same, and there is reasonable agreement between the different observations.

Suri et al. (1975) have discussed some of the implications of the photon spectrum shown in Figure 20. The change of slope around 100 keV has been observed previously in other solar flares (Frost 1969), and it is probably due to a break in the electron spectrum caused by the acceleration mechanism that operates in this energy region. A more novel feature of the spectrum in Figure 20 is the flattening at ~500 keV which leads in the MeV region to an

excess photon flux over the simple extrapolation of the observed flux at lower energies. It is worth noting that a similar flattening was probably observed for the 1967, May 23 flare by Gruber et al. (1973). The absolute photon flux in the MeV region for this flare was almost the same as for the 1972, August 4 event.

Suri et al. (1975) have suggested that this excess could be due to a separate population of electrons which would be accelerated by a second stage of acceleration. Independent of the origin of these electrons, we proceed now to calculate their number and spectrum from the observed gamma-ray continuum.

The line A in Figure 20 represents the instantaneous photon flux obtained from the electron spectrum A in Figure 21 by using equation (26) and the bremsstrahlung cross section given by equation (24). Similarly, the lines B and C represent the photon fluxes obtained from the electron spectra B and C. The spectrum A has a break at about 140 keV which produces the observed break in the photon spectrum at about 100 keV and it has a high energy cutoff at 1 MeV. Both the electron spectra B and C can produce the observed gamma-ray continuum above ~0.5 MeV.

The dashed lines in Figure 21 are some representative proton spectra in the thin-target model obtained by using the parameters of Table 4. Because the gamma-ray lines which determine these parameters are quite insensitive to the proton spectrum below several MeV, while the gamma-ray continuum which determines the electron spectrum has been measured only up to several MeV, there is no common energy region where both the proton and electron spectra are well determined. Nonetheless, the results of Figure 21 seem to suggest that the proton-to-electron ratio at the same energy ranges from about 10 to 10^2. The analytic forms of the spectra shown in Figure 21 are given in Table 5.

Comparison of these implied particle spectra in the solar flare region with the proton spectrum observed in the interplanetary medium from the 1972, August 4 flare is complicated by the possibility that the latter spectrum may have been significantly modified by acceleration in the interplanetary medium.

To obtain an estimate of the number of protons released into the interplanetary medium, the information obtained from the gamma rays in the thin-target model can be combined with data on the path length traversed by the nuclei before their escape from the interaction region. Such information can be obtained from studies of deuterons and helium-3 abundances in accelerated nuclei from flares. The ^{2}H and ^{3}He observations from the 1972, August events (Webber et al. 1975), when compared with calculations of the production of these isotopes in nuclear reactions (Ramaty and Kozlovsky 1974) imply that the amount of matter traversed by relativistic particles is about 1.5 g cm^{-2}. This means that the product $n_H t_1$ is about 3×10^{13} cm^{-3}s, where t_1 is the interaction time of the particles at the Sun. If t_1 is also interpreted as the escape time of the particles from the interaction region, then from the values of $n_H N_p$ determined above, we find that the protons were released into the interplanetary medium at an average rate $N_p(>30\text{MeV})/t_1$ varying from about 1.6 to 3×30^{30} protons s^{-1}. The total number of protons released is the product of this rate and the acceleration time T. As indicated by the x-ray data (van Beek et al. 1973), T is about 10^3 seconds; therefore the total number of protons released above 30 MeV is between about 1.6 to 3×10^{33}. These numbers are larger by only about a factor of 2 to 3 than the number of protons released downward into the Sun in the thick-target model.

The number of protons released from the flare should be compared with estimates of the total number of protons in the interplanetary medium as

obtained from charged particle observations. Ramaty and Lingenfelter (1973a) have estimated this quantity by taking the observed density of protons near Earth and multiplying it by a storage volume in the interplanetary medium which they took to be $\sim 10^{39}$ cm^3. Using this volume and the peak proton flux greater than 30 MeV measured by Kohl et al. (1973), we get about 10^{34} protons. This number is larger by a factor of 3 to 6 than our estimate for the number of protons released in the thin-target model. But since the measured peak proton flux could consist to a large degree of particles accelerated by shocks in the interplanetary medium, it appears that there is no real discrepancy between the number of protons released for the Sun as deduced from the gamma rays and the number observed in interplanetary space.

We now turn briefly to the processes of energy loss by the accelerated particles in the flare region and the problem of whether such processes are the principal source of energy for the heating of a flare. Giovanelli (1946) first suggested that accelerated electrons caused the ionization and excitation responsible for the optical line emission, while Gordon (1954) proposed that accelerated protons were primarily responsible. Detailed studies of the ionization losses and resulting optical emission processes have been made for both accelerated electron (e.g. Neupert 1968; Brown 1973; Somov and Syrovatskii 1974) and proton (e.g. Dubov 1963; Najita and Orrall 1970; Svestka 1970) interactions with the ambient gas in the flare region.

Although estimates (Neupert 1968; Syrovatskii and Shmeleva 1972; Brown 1973) of the electron energy loss, based on measurements of the x-ray emission suggest that sufficient energy for the optical emission may

be available from the electrons alone, an estimate of the relative importance of electron and proton ionization losses has not previously been possible because of the lack of information on the number and spectrum of accelerated protons in the flare region. The gamma ray measurements of Chupp et al. (1973) however, now allow us to at least place some limits on the ratio of total energy loss rates of accelerated protons and electrons in the 1972, August 4 flare.

For the thin-target case the instantaneous energy loss rate for electrons and protons is

$$\dot{W} = \frac{n}{A} \int dE\ N\ (E)\ c\beta dE/dx \qquad (28)$$

where the electron collisional energy loss rate dE/dx for electrons is taken from Berger and Seltzer (1964) and for protons from Barkas and Berger (1964).

For the thick-target case where essentially all the entire kinetic energy of the particle is dissipated in ionization losses the total energy loss is simply

$$W = \int dE\ \bar{N}\ (E)\ E \qquad (29)$$

for both electrons and protons. The energy dissipated by electrons in bremsstrahlung and by protons in inelastic collisions is neglible fraction of the total kinetic energy for the flare accelerated particle.

The minimum energy loss by accelerated electrons in the 1972, August 4 flare can be directly determined from the x-ray emission measured by van Beek et al. (1973) down to about 20 keV, shown in Figure 20. Below this energy thermal emission from the high temperature region of the flare masks the nonthermal emission. As discussed above, assuming that the emission >20 keV

results from accelerated electron bremsstrahlung, the required total electron energy spectrum for the thin-target case is found to be

$$N(E) = 2.1 \times 10^{44} E(\mathrm{MeV})^{-2.5}/n, \qquad (30)$$

in the energy range from ~20 to ~140 keV. The greatest contribution to the energy loss comes from these lowest energy electrons. Using this spectrum in equation (28) we find an instantaneous electron energy loss rate $\dot{W}$ (>20 keV) = 3×10^{28} ergs/sec. Also, as discussed above, if we assume a time of the order of $\sim 10^3$ sec for the duration of the flare we find a total electron energy loss W (>20 keV) $\approx 3 \times 10^{31}$ ergs. A comparable total energy loss is also required to account for the observed emission by electron bremsstrahlung in the thick-target case. As in other flares the energy loss from these electrons exceeds the total radiation energy of the flare, comprising an estimated (Zirin and Tanaka, 1973) total optical emission energy in H_α of $\sim 2 \times 10^{30}$ ergs, with comparable energy emitted in Lyman α and in high temperature thermal emission in soft x-rays. A large fraction of heating energy, however, may remain in the plasma cloud blown off in the explosive phase of the flare.

The most direct estimate of the energy loss of accelerated protons in the flare can be made from the prompt gamma-ray line emission from $^{12}C^{*4.4}$. In the thin-target case, the ratio of the energy loss rate to the 4.4 MeV line intensity at Earth is obtained by dividing equation (28) by equation (12) times $4\pi R^2$, where R = 1A.U. In equation (28) for power-law spectra, we have assumed that below an energy E_c, N(E) is constant, i.e. $N(E) = kE^{-s}$ for $E > E_c$, and $N(E) = kE_c^{-s}$ for $E < E_c$. No such cutoff is assumed for exponential spectra. The ratio $W_p/\phi_{4.4}$ shown in Figure 22 is independent of the ambient gas density; it depends only on the spectral index, and for

power-law spectra, on the cutoff energy E_c. As can be seen from Figure 10, the production of $^{12}C^{*4.43}$ is independent of the assumed cutoff energy if E_c is less than a few MeV.

For power-law spectra in the range $1.7 < s < 2.1$ determined above from the ratio 2.2 MeV to 4.4 MeV line intensities, we see from Figure 22 that $\hat{W}/\phi_{4.4}$ for $E_c = 2.5$ ranges from 1.4×10^{28} to 1.9×10^{28} ergs cm^2/photon. Thus the observed $\phi_{4.4}$ of $\sim 3 \times 10^{-2}$ photons/(cm^2 sec) requires a minimum proton-energy loss rate of $\sim(5 \pm 1) \times 10^{26}$ ergs/sec. There is no reason to believe, however, that the proton spectrum would cut off just below the $^{12}C^{*4.4}$ threshold. If the same spectral index held down to 0.5 MeV or 0.1 MeV, for example, the required proton energy loss rate, derived from Figure 22, would then be $(3 \pm 1.5) \times 10^{27}$ or $(2 \pm 1.6) \times 10^{28}$ ergs/sec respectively. The latter value is comparable to the minimum electron energy loss rate of 3×10^{28} erg/sec. For the exponential spectra, on the other hand, the range 120 MV $< P_o <$ 300 MV gives a proton energy loss rate of only $(4 \pm 1) \times 10^{26}$ erg/sec independent of any assumed cutoff energy. Thus we see that the uncertainty in the low-energy cutoff of the spectrum does not allow us to determine whether or not proton ionization losses make a significant contribution to the heating of the flare region.

A similar situation prevails for the thick-target case. The ratio of the total proton energy loss to time-integrated 4.4 MeV gamma-ray line emission, $W/\bar{\phi}_{4.4}$, obtained by dividing equation (29) by $4\pi R^2$ times equation (13), is also shown in Figure 22. Here, for the thick-target power-law spectra with $2.4 < s < 3.2$, we find a total proton energy loss $W \approx (2 \pm 1) \times 10^{30}$ ergs for the minimum cutoff $E_c = 2.5$ MeV or energy

losses of $\sim(1.1 \pm 0.9)\times10^{31}$ ergs for E_c = 0.5 MeV and $(7 \pm 6.5)\times10^{31}$ ergs for E_c = 0.1 MeV. These are again comparable to the minimum electron loss of $\sim3\times10^{31}$ ergs, but the uncertainty in E_c permits no more quantitative comparison. For exponential spectra, however, with 80 MV < P_o < 220 MV, the total proton energy loss must be only $\sim(2.1 \pm 0.6) \times 10^{29}$ ergs.

7. The Nature of the Positron Annihilation Radiation

Positrons can be produced in solar flares from the decay of π^+ mesons and radioactive nuclei which result from nuclear reactions of accelerated protons and nuclei with the ambient medium. Some solar positrons could also be created by accelerated electrons in e^+-e^- pairs. Annihilation of positrons can produce a gamma-ray line at 0.51 MeV. This line was observed by Chupp et al. (1973) for both the 1972, August 4 and August 7 flares.

The most important positron emitters, their half lives and maximum positron energies are listed in Table 6, together with their main production reactions and their threshold energies. The cross sections for the production of π^+ mesons were given by Lingenfelter and Ramaty (1967).

The cross sections for producing the radioactive nuclei are shown in Figure 23. The cross sections for forming ^{10}C and ^{11}C by spallation of ^{16}O, ^{14}N, and ^{12}C were summarized by Audouze et al. (1967), Meneguzzi et al. (1971) and Mitler (1972). To these cross sections we added the low-threshold reaction $^{14}N(p,\alpha)^{11}C$ measured recently by Jacobs et al. (1974). The cross section for producing ^{12}N by $^{12}C(p,n)^{12}N$ was taken from Rimmer and Fisher (1968). The ^{13}N producing-cross section is the same as in Lingenfelter and Ramaty (1967) except for the low-energy part of the reaction $^{16}O(p,)^{13}N$ which is from Albouy et al. (1962). The cross sections for the reactions $^{14}N(p,n)^{14}O$ and $^{16}O(p,)^{14}O$ are from Audouze et al. (1967) and Meneguzzi et al. (1971). The cross section for ^{15}O production in proton induced reactions is the same as in Lingenfelter and Ramaty (1967). In the numerical calculations we have added the low-threshold reaction $^{12}C(\alpha,n)^{15}O$ which has been discussed in the neutron-production section. The cross section for the reaction $^{16}O(\alpha,n)^{19}Ne$ has not been measured. As discussed in Section 3, we assume that this cross section is the same as that of the reaction $^{12}C(\alpha,n)^{15}O$ which was measured by Nelson et al. (1963).

Using these cross sections we calculate from equations (12) and (13) the positron emitter production for the thin and thick-target models. By way of illustration the instantaneous production rates of positron-emitters in the thin-target model for power-law spectra are shown in Figure 24. As can be seen, for flatter spectra the principal positron source is π^+ mesons, but for steeper spectra ^{11}C is the largest source and the pion contribution is negligible. This effect can also be seen in Figure 25, where the ratio of the pion yield to the total positron-emitter yield (including both pions and radioactive nuclei) is plotted as a function of s or P_o for both interaction models. We see that, as for neutron production, the efficiency of π^+ production is larger in the thick-target model than in the thin-target model. The ratios of the total yield of positron-emitters to the neutron yield are shown in Figure 26 for the various interaction models.

The intensity of the 0.51 MeV line, however, depends not only on the number of positron emitters produced, but also on the decay rate of the positron emitters and on the annihilation rate of the positrons. The half lives against radioactive decay of the various positron emitters are shown in Table 6. Thus, in the early phases of particle acceleration and interaction on time scales less than 20 minutes, ^{11}C is a less important source than the shorter lived (1 to 2 minutes) positron emitters ^{14}O and ^{15}O. At later times, however, ^{11}C can provide delayed positrons after significant nuclear interactions have ceased.

In addition, the annihilation rate of the positrons depends on the density, temperature and state of ionization of the ambient medium. As discussed previously (Stecker 1969, Ramaty and Lingenfelter, 1973b) in a

low-density neutral medium, positrons nearly always annihilate via positronium formation. Only if the ambient density exceeds about 10^{15} cm^{-3} do collisions destroy the ^3S state of positronium at such a rate that free annihilation becomes more important than positronium annihilation (Leventhal 1973). Positron annihilation from a bound state of positronium results in an asymmetric 0.51 MeV line, since 75% of the time positronium annihilates from the ^3S state into 3 photons of energies less than 0.51 MeV, instead of 2 photons at precisely this energy. The 0.51 MeV line from the Sun, however, appears to be symmetric.

As we noted, three-photon annihilation could be reduced by collisions, but the required density of $\geq 10^{15}$ cm^{-3} is quite large. However, if the ambient medium is ionized, the rate of positronium formation is greatly reduced. In Figure 27 we show the rate of positronium formation and free annihilation per positron in a hydrogen plasma of unit density as a function of its temperature (C. Werntz and C.Crannell, private communication 1973).

As can be seen, if the temperature is greater than about 10^6 °K, most of the positrons annihilate without forming positronium. This is not an unreasonable temperature for the annihilation region. From the observed upper limit on the width of the 0.51 MeV line, however, the temperature in the annihilation region should be less than $\sim 10^7$ °K (Chupp et al. 1975).

According to the observations of the 1972, August 4 flare, the rise time of the 0.51 MeV line was, within instrumental errors, similar to or perhaps even shorter than the rise time of the 2.2 MeV line (Chupp et al. 1975). The latter was about 100 seconds, consistent with the expected lag between the production of the neutrons and the formation of the 2.2 MeV

line (see Table 2). Assuming that the time dependence of the production rate of the positron emitters is the same as that of the neutrons, it follows that the lag between the production of the positron emitters and the formation of the 0.51 MeV line should also not be longer than about 100 seconds. From Figure 27, this result implies that the density of the ambient medium in the annihilation region is at least 10^{12} cm^{-3}. Furthermore if the positrons are of nuclear origin, then from Table 6 it follows that they should mainly result from π^+ mesons and short lived radioactive nuclei (^{15}O,^{14}O).

The observed average flux in the 0.51 MeV line for the flare of 1972, August 4 was about 0.06 photons $cm^{-2}s^{-1}$ (Chupp et al. 1975). Hence the observed $\phi_{0.51}/\phi_{2.2}$ ratio was about 0.2.

Let f' be the 0.51 MeV photon yield per positron defined in the same way as the 2.2 MeV photon yield per neutron, $\bar{f}$, in equation (21). As discussed in Section 3, $\bar{f}$ ranges from about 0.1 to 0.2. The maximum value of f' is 2. But because part of the positrons can escape from the Sun before they annihilate, and a fraction of the positrons can be trapped at the Sun in low density regions where the annihilation time is long, f' can be considerably less than 2.

According to our discussion in Section 6, for power law spectra s~2 in the thin-target model, and s~3 in the thick-target model. For these spectral parameters, from Figure 25 we see that the bulk of the positron emitters are π^+ mesons, and from Figure 26 we get that the positron emitter-to-neutron ratio is about 0.2. The observed ratio, $\phi_{0.51}/\phi_{2.2} \simeq 0.2$ then implies that $f' \simeq \bar{f}$, i.e. the 0.51 MeV yield per positron is about the same as the 2.2 MeV yield per neutron. In view of the uncertainties involved

in the deductions of f', this is not an unreasonable result. We can also deduce f' for the various values of P_o obtained in Section 6, and in all cases we find acceptable values ($0.1 < f' < 2$). For these exponential spectra the contribution of π^+ mesons to the total positron production is greater than about 50% in all cases, except in the thick-target model with no ^{3}He in the photosphere where they contribute only about 25% of the positrons. A definite test of the possibility that the bulk of the positrons are due to π^+ mesons would be the observation of gamma rays from π° decay. We give estimates of the expected flux of such gamma rays in Section 8.

As mentioned above, prompt 0.51 MeV photons could also result from positrons produced in e^+-e^- pairs. The cross section for pair production by relativistic electrons on ambient protons is given by (Heitler 1954)

$$\sigma \text{ pair} \simeq \frac{28}{27\pi}\left(\alpha r_o\right)^2 \left[\ln\left(\frac{1}{4}\gamma\right)\right]^3 \qquad (31)$$

Using this cross section, the instantaneous pair production rate was calculated (T. Bai, private communication 1974) from equation (12) for the thin-target model with power-law spectra. The results are shown in Figure 28 for various spectral indexes s and high-energy cutoffs, E_T, of the assumed electron spectrum.

As we have seen in Section 6, the continuum gamma-ray emission from the flare of 1972, August 4 is consistent with an electron spectrum which above about 1 MeV is given by curves B or C in Figure 20. If we consider the spectrum B, and assume that the 0.51 MeV photon yield per positron, f', has its maximum value of 2, then from Figure 28 we find that for the 1972, August 4 flare the 0.51 MeV photon flux from pair production ranges from about 8×10^{-5} to 6×10^{-4} photons $cm^{-2}s^{-1}$, depending on the assumed high

energy cutoff. These values are smaller by factors of 10^2 to 10^3 than the observed flux of about 0.06 photons $cm^{-2}s^{-1}$ (Chupp et al. 1975). Pair production therefore accounts for less than 1% of the observed 0.51 MeV line intensity.

8. High Energy Gamma Rays and Neutrons

In addition to line emissions, nuclear reactions in solar flares also produce π° mesons which decay into high energy gamma rays. Each π° meson yields two photons with energy spectrum centered about 67.5 MeV. Using the π° production cross sections in proton-proton (Lingenfelter and Ramaty 1967) and proton-α particle reactions (Stecker 1970), we have calculated the yields of π° mesons in the thin and thick-target models for power-law and exponential spectra. The results are shown in Figure 29. The total π°-decay gamma-ray flux can be obtained from this figure by using the formula

$$\phi_{\pi^\circ} = \phi_{2.2} \left(\frac{2\pi_o}{n}\right) \bar{f}^{-1}, \qquad (32)$$

where $\phi_{2.2}$ is the observed 2.2 MeV line intensity and $\bar{f}$ is the average photon yield per neutron given in Figure 9.

No high-energy gamma rays have been observed from solar flares. Nonetheless, the following values of ϕ_{π° can be calculated for the 1972, August 4 flare: For $^3He/H = 5\times10^{-5}$, the parameters of Table 4 yield:

$3\times10^{-3} \leq \phi_{\pi^\circ} \leq 0.13$ for the thick-target exponential model,

$0.035 \leq \phi_{\pi^\circ} \leq 0.37$ for the thin-target exponential model,

$0.13 \leq \phi_{\pi^\circ} \leq 0.42$ for the thick-target power-law model, and

$0.25 \leq \phi_{\pi^\circ} \leq 0.7$ for the thin-target power-law model.

These fluxes should be compared with the bremsstrahlung that is expected at high energies from the electron spectra shown in Figure 21. For the spectra B and C we get $\phi(>30\ \text{MeV}) \simeq 0.07$ ph $cm^{-2}s^{-1}$ and $\phi(>30\ \text{MeV}) \simeq 10^{-3}$ ph $cm^{-2}s^{-1}$, respectively. We see that high-energy gamma rays from π° decay could be observable from solar flares. Moreover, the characteristic broad maximum of these gamma-rays' energy spectrum makes them easily distinguishable from a possible bremsstrahlung continuum.

Finally, we also present the expected high energy neutron fluxes at Earth for our various interaction models. In Figure 30 we give the ratio of the time-averaged neutron flux $\phi_{\hat{n}}$ to the time-averaged 2.2 MeV line intensity for these models. The time dependence of these two fluxes, however, are quite different, as was discussed by Lingenfelter and Ramaty (1967). Nonetheless, we see that for certain parameters, ϕ_n can become as large or even larger than $\phi_{2.2}$, and hence potentially detectable for large solar flares. We note that ϕ_n in Figure 30 has been calculated under the assumption that the neutrons are produced isotropically at the Sun. However, ϕ_n is greatly reduced if the neutrons are produced with initial velocities predominantly toward the Sun.

The detection of gamma-rays from π° decay or high energy neutrons would provide spectral information on accelerated particles in the several hundreds MeV/nucleon range. In contrast, the nuclear deexcitation lines and the 2.2 MeV line which is produced by lower energy neutrons, provide information on the primary particles mainly in the 10 to 100 MeV/nucleon region.

9. Summary

The observed gamma-ray lines from the 1972, August 4 flare, at 0.5, 2.2, 4.4 and 6.2 MeV are due to positron annihilation, neutron capture on hydrogen, and deexcitation of excited states in ^{12}C, ^{16}O and ^{16}N, respectively. The strongest line is at 2.2 MeV. It is due to fast neutrons produced by nuclear reactions of flare accelerated particles with the ambient solar atmosphere. These neutrons are thermalized and captured by ambient protons in the photosphere to produce deuterons and 2.2 MeV gamma rays. Photospheric ^3He competes with the protons in capturing neutrons. Because captures on ^3He do not lead to photon emission, the observation of 2.2 MeV line emission from the Sun implies that the ^3He abundance in the photosphere cannot be much larger than that observed in the solar wind ($^3He/H \sim 5 \times 10^{-5}$).

We have evaluated in detail the yield of neutrons and excited nuclei from nuclear reactions of accelerated particles with the ambient solar atmosphere. For the 1972, August 4 flare the neutrons are produced mainly in $p\alpha$ and αp reactions by accelerated particles with energies greater than about 30 MeV/nucleon. The observed gamma rays at 4.4 and ~6.2 MeV are principally due to proton induced interactions. Reactions induced by fast nuclei lead to Doppler broadened lines which cannot be distinguished from the continuum. We have determined the relative importance of other prompt lines that might be observed from solar flares in addition to the 4.4 MeV line and the 6.2 MeV feature. The most promising candidates are at 0.85, 1.24, 1.63, 1.78, 2.31 and 5.3 MeV. Of particular interest are the iron lines at 0.85 and 1.24 MeV which have very narrow Doppler widths of only a few keV.

The positrons which produce the 0.51 MeV line are due to π^+ mesons and radioactive nuclei. We have evaluated in detail the production of mesons

and radioactive nuclei in nuclear reactions of accelerated charged particles with ambient nuclei. The relatively prompt nature of the 0.51 MeV line seems to favor positron production from π^+ decay in the initial phase of the 1972, August 4 event. The 0.51 MeV line emission observed late in the 1972, August 7 event is very likely due to delayed positrons from radioactive nuclei. The spectral region around 0.5 MeV is complicated by the possibility that some of the positrons decay into 3 photons from the triplet state of positronium, and that a strong feature at ~.46 MeV is produce by the ^{7}Li and ^{7}Be lines. A detector with very good energy resolution is required to resolve the various structures in this energy region.

From the comparison of the calculated and observed ratios of the line at 4.4 MeV to the line at 2.2 MeV it is possible to deduce the spectrum of the accelerated particles in the flare region. For the 1972, August 4 flare the spectral index s defined in equation (14) is 1.9 ± 0.2 for the thin-target model and 3 ± 0.3 for the thick-target model if there is no ^{3}He in the photosphere; or 1.7 ± 0.2 and 2.7 ± 0.3 for these models if the photospheric ^{3}He/H ratio is 5×10^{-5}. The characteristic rigidity P_o defined in equation (15) is 170 ± 50 MV for the thin-target model and 110 ± 30 MV for the thick-target model if ^{3}He/H = 0; or 250 ± 80 MV and 165 ± 55 MV for these models if ^{3}He/H = 5×10^{-5}. The total number of protons above 30 MeV released downward into the Sun in the thick-target model is about 10^{33}. For the thin-target model about 2×10^{33} protons of energies greater than 30 MeV escape from the flare region if relativistic particles traverse about 1.5 g cm^{-2} as deduced from deuteron and helium-3 abundances in the accelerated particle fluxes. The energy loss rate of protons with energies greater than 2.5 MeV is about 5×10^{26} erg s^{-1} and the total energy

deposited by these protons at the Sun is $\sim 5 \times 10^{29}$ erg. However, if the proton spectrum as deduced from the gamma-ray observations is extrapolated down to 0.1 MeV, the protons deposit an energy comparable to that deposited by electrons of energies greater than 20 keV. From the x-ray observations, the rate of energy loss of these electrons is $\sim 3 \times 10^{28}$ erg s^{-1}, and the total energy deposited by them is $\sim 3 \times 10^{31}$ erg.

For the flare of 1972, August 4, a gamma-ray continuum has been observed at energies greater than about 0.5 MeV, and it appears that it is produced by a separate population of electrons in this energy range. The number of these electrons is lower than the number of protons of the same energy by about a factor of 10 to 10^2, but their spectrum could be the same as that of the protons. This result may have significant implications on particle acceleration in solar flares.

Finally, high energy neutrons and gamma-rays from π° decay could be detected from flares such as the 1972, August 4 event. We expect a minimum π°-decay gamma-ray flux of 3×10^{-3} photons $cm^{-2} s^{-1}$, and, if the neutrons are produced isotropically at the Sun, a time integrated high energy neutron flux comparable to the time-integrated 2.2 MeV line intensity. The detection of these high-energy gamma-rays and neutrons would provide spectral information on the accelerated particles in the region of several hundred MeV. The presently observed nuclear excitation lines and the 2.2 MeV line provide information on particles mainly below 100 MeV.

In closing, we wish to note that essentially all the observational data used in this paper has been obtained from one large solar flare. As we have tried to show, this very limited data already contains a great deal of

information not only on the physics of nuclear interactions in flares but also on solar physics in general. We hope, therefore, that more data will be forthcoming during the next solar maximum, and that solar gamma-ray astronomy will be a vigorously explored discipline of solar physics.

References

Akhiezer, A.I. and Berestetskii, V.B.: 1965, Quantum Electrodynamics, Interscience Publishers, New York.

Albouy, M.G., Cohen, J.P., Gusakow, M., Poffe, N., Serbolle, H., and Valentin, L.: 1962, Phys. Letters 2, 306.

Ascuito, R.J.: 1972, Nuclear Phys. 192, 97.

Ashery, D.: 1969, Nuclear Phys. A136, 481.

Audouze, J., Ephere, M., and Reeves, H.: 1967, High-Energy Nuclear-Reactions in Astrophysics, ed. by B.S.P. Shen (W.A. Benjamin, New York), p. 255.

Bair, J.K. and Willard, H.B.: 1962, Phys. Rev. 128, 299.

Bair, J.K. and Haas, F.X.: 1973, Phys. Rev. C 7, 1356.

Bair, J.K.: 1973, Phys. Rev. C 8, 120.

Barkas, W.H. and Berger, M.J.: 1964, Tables of Energy Losses and Ranges of Heavy Charged Particles, NASA SP-3013 (National Aeronautics and Space Administration, Washington, D.C.).

Berger, M.J. and Seltzer, S.M.: 1964, Tables of Energy Losses and Ranges of Electrons and Positrons, NASA SP-3012 (National Aeronautics and Space Administration, Washington, D.C.).

Bergman, C. and Hobbie, R.K.: 1971, Phys. Rev. C 3, 1729.

Biermann, L., Haxel, O., and Schluter, A.: 1951, Z. Naturforsch, 6a, 47.

Bland, C.J.: 1966, Nuovo Cimento 44B, 427.

Blatchley, D.E. and Bent, R.D.: 1965, Nuclear Phys. 61, 641.

Blatt, J.M. and Weisskopf, V.F.: 1952, Theoretical Nuclear Physics, (John Wiley & Sons, New York).

Boldt, E.A. and Serlemitsos, P.J.: 1969, Ap. J. 157, 557.

Brown, J.C.: 1973, Solar Phys. 31, 143.

Cameron, A.G.W.: 1973, Space Sci. Rev. 15, 121.

Cheng, C.C.: 1972, Space Sci. Rev. 13, 3.

Chupp, E.L.: 1964, AAS-NASA Symposium on the Physics of Solar Flares, NASA SP-50 (National Aeronautics and Space Administration, Washington, D.C., p. 445.

Chupp, E.L., Forrest, D.J., Higbie, P.R., Suri, A.N., Tsai, C., and Dunphy, P.P.: 1973, Nature 241, 333.

Chupp, E.L, Forrest, D.J., and Suri, A.N.: 1975, Proc. of IAU/COSPAR Symposium No. 68, Solar γ, x and EUV Radiations, edited by S. Kane, to be published.

Clegg, A.B., Foley, K.J., Salmon, G.L, and Segel, R.E.: 1961, Proc. Phys. Soc. 78, 681.

Correlli, J.C., Bleuler, E., and Tendam, D.J.: 1959, Phys. Rev. 116, 1184.

Dere, K.P., Horan, D.M., and Kreplin, R.W.: 1973, World Data Center Rept. UAG-28 part II, Collected Data Reports on August 1972 Solar Terrestrial Events, edited by H.E. Coffey, p. 298.

Dolan, J.F. and Fazio, G.G.: 1965, Rev. Geophys. 3, 319.

Dubov, E.E.: 1963, Izv. Krym. Astrofiz. Obs.29, 86.

Fawzi, M.A.: 1972, Z. Physik 250, 120.

Foley, K.J., Salmon, G.L. and Clegg, A.B.: 1962, Nuclear Phys. 31, 43.

Frost, K.J.: 1969. Ap. J. Letters 158, L159.

Furukawa, M. and Tanaka, S.: 1961, J. Phys. Soc. Japan 16, 129.

Gibbons, J.H. and Macklin, R.L.: 1959, Phys. Rev. 114, 571.

Giovanelli, R.G.: 1946, Nature 158, 81.

Gordon, I.M.: 1954, Doklak. Akad. Nauk SSSR 94, 813.

Gruber, D.E., Peterson, L.E., and Vette, J.I.: 1973, High Energy Phenomena on the Sun, edited by R. Ramaty and R.G. Stone, NASA SP-342, (National Aeronautics and Space Administration, Washington, D.C.), p. 147.

Haas, F.X. and Bair, J.K.: 1973, Phys Rev. C. 7, 2432.

Harvey, B.G., Rivet, E.J., Springer, H., Meriwether, J.R., Jones, W.B., Elliot, J.H., and Darriulat, P.: 1964, Nuclear Phys. 52, 465.

Heitler, W.: 1954, The Quantum Theory of Radiation, Oxford University Press, London.

Hess, W.N.: 1958, Rev. Mod. Phys. 39, 368.

Hess, W.N.: 1962, 5th Interamerican Seminar on Cosmic Rays (La Paz Bolivia), p. 17.

Ito, K., Okazoe, H., and Yoshimori, M.: 1968, Can. J. Phys. 46, S780.

Ito, K. and Okazoe, H.: 1969, Acha. Phys. Hung 29, Suppl. 2, 679.

Jacobs, W.W., Bodansky, D., Chamberlin, D., and Oberg, D.L.: 1974, Phys. Rev. C 9, 2134.

Koch, H.W. and Motz, J.W.: 1959, Rev. Mod. Phys. 31, 920.

Kohl, J.W., Bostrom, C.O., and Williams, D.J.: 1973, World Data Center Rept. UAG-28 part II, Collected Data Reports on August 1972 Solar Terrestrial Events, H.E. Coffey, editor, p. 330.

Kozlovsky, B. and Ramaty, R.: 1974a, Ap. J. Letters 191, L43.

Kozlovsky, B. and Ramaty, R.: 1974b, Astron. and Astrophys. 34, 477.

Kozlovsky, B. and Ramaty, R.: 1974c, Astron. and Astrophys, in press.

Kuzhevskii, B.M.: 1968, Sov. Astron. 12, 595.

Lapointe, S.M.: 1960, unpublished thesis, Cornell University.

Leventhal, M.: 1973, Ap. J. Letters 183, L147.

Lingenfelter, R.E.: 1969, Solar Phys. 8, 341.

Lingenfelter, R.E., Flamm, E.J., Canfield, E.H., and Kellman, S.: 1965a, J. Geophys. Res. 70, 4077.

Lingenfelter, R.E., Flamm, E.J., Canfield, E.H., and Kellman, S.: 1965b, J. Geophys. Res. 70, 4087.

Lingenfelter, R.E. and Ramaty, R.: 1967, High Energy Nuclear Reactions in Astrophysics, edited by B.S.P. Shen,(W.A. Benjamin, New York), p. 99.

McGowan, F.K., Milner, W.Y., Kim, H.J., and Hyatt, W.: 1969, Nuclear Data Tables A6, 353.

McGowan, F.K., Milner, W.Y., Kim, H.J., and Hyatt, W.: 1970, Nuclear Data Tables A8, 199.

Meneguzzi, M., Audouze, J., and Reeves, H.: 1971, Astron. and Astrophys. 15, 337.

Meyer, J.P.: 1972, Astron. and Astrophys. Suppl. 7, 417.

Meyerhof, W.E. and Tombrello, T.A.: 1968, Nuclear Phys. A109, 1.

Mitchel, G.E., Carter, E.B., and Davis, R.H.: 1964, Phys. Rev. 133, B1434.

Mitler, H.E.: 1972, Astrophys. and Space Sci. 17, 186.

Morgan, J.F. and Hobbie, R.K.: 1970, Phys. Rev. C1, 155.

Morrison, P.: 1958, Nuovo Cimento 7, 858.

Najita, K. and Orrall, F.Q.: 1970, Solar Phys. 15, 176.

Nelson, J.W., Carter, E.B., Mitchell, G.E., and Davis, R.H.: 1963, Phys. Rev. 129, 1723.

Neupert, W.M.: 1968, Ap. J. Letters 153, L59.

Oda, Y., Takeda, M., Takano, T., Yamazaki, T., Hu, C., Kikuchi, K., Kobayashi, S., Matsuda, K., and Nagahara, Y.: 1960, J. Phys. Soc. Japan 15, 760.

Ramaty, R. and Lingenfelter, R.E.: 1969, Ap. J. 155, 587.

Ramaty, R. and Lingenfelter, R.E.: 1973a, High Energy Phenomena on the Sun, edited by R. Ramaty and R.G. Stone, NASA SP-342 (National Aeronautics and Space Administration, Washington, D.C.), p. 301.

Ramaty, R. and Lingenfelter, R.E.: 1973b, Conference Papers, 13th International Cosmic Ray Conference, University of Denver, Colorado, p. 1590.

Ramaty, R. and Kozlovsky, B.: 1974, Ap. J. 193, 729.

Ramaty, R. and Lingenfelter, R.E.: 1975a, Proc. of the IAU/COSPAR Symposium No. 68, Solar γ, x and EUV Radiations, edited by S. Kane, to be published.

Ramaty, R. and Lingenfelter, R.E.: 1975b, Proc. of 6th Leningrad Symposium on Particle Acceleration and Nuclear Reactions in Space, to be published.

Reppin, C., Chupp, E.L., Forrest, D.J., and Suri, A.N.: 1973, Conference Papers, 13th International Cosmic Ray Conference, University of Denver, Denver, Colorado, p. 1577.

Rimmer, E.M. and Fisher, P.S.: 1968, Nuclear Phys. A108, 561.

Sekharan, K.K., Divatia, A.S., Mehta, M.K., Kerekatte, S.S., and Nambiar, K.B.: 1967, Phys. Rev. 156, 1187.

Shklovsky, I.S.: 1965, Soviet Astronomy A.J. 8, 538.

Smith, S.M., Tibell, G., Cowley, A.A., Goldberg, D.A., Pugh, H.G., Reichart, W., and Wall, N.S.: 1973, Nuclear Phys. A207, 273.

Somov, B.V. and Syrovatskii, S.I.: 1974, Solar Phys, in press.

Stecker, F.W.: 1969, Astrophys. Space Sci. 3, 479.

Stecker, F.W.: 1970, Astrophys. and Space Sci. 6, 377.

Suri, A.N., Chupp, E.L., Forrest, D.J., and Reppin, C.: 1975, Solar Phys., to be published.

Svestka, Z.: 1970, Solar Phys. 13, 471.

Syrovatskii, S.I.: 1959, Soviet Astronomy A.J. 3, 22.

Syrovatskii, S.I. and Shmeleva, O.P.: 1972, Soviet Astronomy A.J. 16, 273.

Tanaka, S. and Furukawa, M.: 1959, J. Phys. Soc. Japan 14, 1269.

van Beek, H.F., Hoyng, P., and Stevens, G.A.: 1973, World Data Center Rept. UAG-28 part II, Collected Data Reports on August 1972 Solar Terrestrial Events, H.E. Coffey, editor, p. 319.

Walton, R.B., Clement, J.D., and Boreli, F.: 1957, Phys. Rev. 107, 1065.

Wang, H.T. and Ramaty, R.: 1974, Solar Physics 36, 129.

Wang, H.T.: 1975, Ph.D. Thesis, University of Maryland.

Webber, W.R., Roelof, E.C., McDonald, F.B., Teegarden, B.J., and Trainor, J.: 1975, Ap. J.,(to be published).

Yavin, A.I. and Farwell, G.W.: 1959, Nuclear Phys. 12, 1.

Zirin, H. and Tanaka, K.: 1973, Solar Phys. 32, 173.

Zobel, W., Maienschein, F.C., and Scroggs, R.J.: 1965, Second Symposium on Protection Against Radiation in Space, edited by A. Reetz, NASA SP-71 (National Aeronautics and Space Administration, Washington, D.C., p. 341.

Zobel, W., Maienschein, F.C., Todd, J.H., and Chapman, G.T.: 1968, Nuclear Science and Engineering 32, 392.

TABLE 1

NEUTRON PRODUCING REACTIONS

	Reaction			Threshold (MeV/nucleon)
1.	$p+^{1}H$	→	$n+p+\pi^{+}$	292.3
2.	$p+^{4}He$	→	$^{3}He+p+n+(\pi)$	25.7
		→	$^{2}H+2p+n+(\pi)$	32.6
		→	$3p+2n+(\pi)$	35.4
3.	$p+^{12}C$	→	n+...	19.6
	$p+^{13}C$	→	n+...	3.2
4.	$p+^{14}N$	→	n+...	6.3
5.	$p+^{16}O$	→	n+...	16.6
	$p+^{18}O$	→	n+...	2.5
6.	$p+^{20}Ne$	→	n+...	15.9
7.	$p+^{56}Fe$	→	n+...	5.5
8.	$\alpha+^{4}He$	→	$^{7}Be+n$	9.5
9.	$\alpha+^{12}C$	→	n+...	2.8
	$\alpha+^{13}C$	→	n+...	---
10.	$\alpha+^{14}N$	→	n+...	1.5
11.	$\alpha+^{16}O$	→	n+...	3.8
	$\alpha+^{18}O$	→	n+...	0.21
12.	$\alpha+^{20}Ne$	→	n+...	2.16
	$\alpha+^{22}Ne$	→	n+...	0.15
13.	$\alpha+^{56}Fe$	→	n+...	1.37
14.	$\alpha+^{25}Mg$	→	n+...	---
15.	$\alpha+^{26}Mg$	→	n+...	---
16.	$\alpha+^{29}Si$	→	n+...	0.43

--- exoergic

TABLE 2

Most probable neutron capture densities, capture times, τ_c, and $\lambda = \tau_c^{-1} + \tau_d^{-1}$, where τ_d is the neutron mean life.

E_n(MeV)	$\langle n \rangle$ (cm^{-3})	τ_c(sec)		λ^{-1}(sec)	
		$He^3/H = 5 \times 10^{-5}$	$He^3/H = 0$	$He^3/H = 5 \times 10^{-5}$	$He^3/H = 0$
1	7×10^{16}	119	214	105	173
10	1.2×10^{17}	69	125	64	110
100	3×10^{17}	28	50	27	47

TABLE 3

PROMPT GAMMA RAY LINES

Photon Energy (MeV)	Origin	Production Modes	Approximate Relative Intensity
0.431	$^{7}Be^{*0.431} \rightarrow$ g.s.	$^{4}He(\alpha,n)^{7}Be^{*0.431}$	1
0.478	$^{7}Li^{*0.478} \rightarrow$ g.s.	$^{4}He(\alpha,p)^{7}Li^{*0.478}$ $^{4}He(\alpha,n)^{7}Be \xrightarrow{12\%} {}^{7}Li^{*0.478}$	1
0.72	$^{10}B^{*0.72} \rightarrow$ g.s.	$^{12}C(p,2pn)^{10}B^{*0.72}$ $^{16}O(p,\ )^{10}B^{*0.72}$	0.1
0.845	$^{56}Fe^{*0.845} \rightarrow$ g.s.	$^{56}Fe(p,p')^{56}Fe^{*0.845}$	0.2
1.24	$^{56}Fe^{*2.08} \rightarrow {}^{56}Fe^{*0.845}$	$^{56}Fe(p,p')^{56}Fe^{*2.08}$	0.2
1.38	$^{24}Mg^{*1.37} \rightarrow$ g.s.	$^{24}Mg(p,p')^{24}Mg^{*1.37}$	0.1
1.63	$^{20}Ne^{*1.63} \rightarrow$ g.s. $^{14}N^{*3.94} \rightarrow N^{*2.31}$ $^{23}Na^{*2.07} \rightarrow {}^{23}Na^{*0.44}$	$^{20}Ne(p,p')^{20}Ne^{*1.63}$ $^{14}N(p,p')^{14}N^{*3.94}$ $^{16}O(p,2pn)^{14}N^{*3.94}$ $^{24}Mg(p,2p)^{23}Na^{*2.67}$	0.2
1.78	$^{28}Si^{*1.78} \rightarrow$ g.s.	$^{28}Si(p,p')^{28}Si^{*1.78}$	0.2
1.99	$^{11}C^{*1.99} \rightarrow$ g.s.	$^{12}C(p,pn)^{11}C^{*1.99}$	0.07
2.31	$^{14}N^{*2.31} \rightarrow$ g.s.	$^{14}N(p,p')^{14}N^{*3.94} \rightarrow {}^{14}N^{*2.31}$ $^{14}N(p,n)^{14}O \rightarrow {}^{14}N^{*2.31}$ $^{16}O(p,2pn)^{14}N^{*2.31}$	0.3
2.75	$^{16}O^{*8.88} \rightarrow {}^{16}O^{*6.14}$	$^{16}O(p,p')^{16}O^{*8.88}$	0.07
~3.62	$^{13}C^{*3.68} \rightarrow$ g.s. $^{6}Li^{*3.56} \rightarrow$ g.s.	$^{16}O(p,3pn)^{13}C^{*3.68}$ $^{12}C(p,\ )^{6}Li^{*3.56}$	0.07
3.84	$^{13}C^{*3.85} \rightarrow$ g.s.	$^{16}O(p,3pn)^{13}C^{*3.84}$	0.07
4.43	$^{12}C^{*4.43} \rightarrow$ g.s.	$^{12}C(p,p')^{12}C^{*4.43}$ $^{12}C(\alpha,\alpha')^{12}C^{*4.43}$ $^{16}O(p,p\alpha)^{12}C^{*4.43}$	1
~5.3	$^{15}O^{*5.26} \rightarrow$ g.s. $^{15}N^{*5.28} \rightarrow$ g.s. $^{15}N^{*5.31} \rightarrow$ g.s.	$^{16}O(p,pn)^{15}O^{*5.26}$ $^{16}O(p,2p)^{15}N^{*5.28}$ $^{16}O(p,2p)^{15}N^{*5.31}$	0.3
6.14	$^{16}O^{*6.14} \rightarrow$ g.s.	$^{16}O(p,p')^{16}O^{*6.14}$ $^{16}O(\alpha,\alpha')^{16}O^{*6.14}$	0.5
6.33	$^{15}N^{*6.33} \rightarrow$ g.s.	$^{16}O(p,2p)^{15}N^{*6.33}$	0.5
~6.7	$^{11}B^{*6.76} \rightarrow$ g.s.	$^{12}C(p,2p)^{11}B^{*6.76}$ $^{12}C(p,2p)^{11}B^{*6.81}$ $^{12}C(p,pn)^{11}C^{*6.50}$	0.07
7.12	$^{16}O^{*7.12} \rightarrow$ g.s.	$^{16}O(p,p')^{16}O^{*7.12}$	0.2

TABLE 4

Deduced Spectral Parameters for the 1972, August 4 Flare

$^3He/H$	s	P_o(MV)
	Thick-Target	
0	2.7 - 3.3	80 - 140
$5x10^{-5}$	2.4 - 3.0	110 - 220
	Thin-Target	
0	1.7 - 2.1	120 - 220
$5x10^{-5}$	1.5 - 1.9	170 - 330

TABLE 5

Average Particle Spectra at the Sun for the 1972, August 4 Flare

Energy Range	nN(E) (particles $MeV^{-1}cm^{-3}$)
Electrons	
$0.02\ MeV < E < 0.14\ MeV$	$2.1 \times 10^{44}\ E(MeV)^{-2.5}$
$0.14\ MeV < E < 1\ MeV$	$2.9 \times 10^{43}\ E(MeV)^{-3.5}$
$1\ MeV < E$	$1.3 \times 10^{43}\ E(MeV)^{-2}$ $2.3 \times 10^{42}\ \exp[\ -E(MeV)/5\ ]$
Protons	
$2.5\ MeV < E < 200\ MeV$	$1.6 \times 10^{45}\ E(MeV)^{-3}$ $1.9 \times 10^{43}\ (dP/dE)\ \exp[-P(MV)/170]$

TABLE 6

Principal Positron Emitters

Positron Emitter	Half Life	Maximum Positron Energy (MeV)	Production Mode	Threshold (MeV)
μ^+	1.5×16^{-6} sec	53	$p+^{1}H \rightarrow \pi^+ \ldots$	292.3
			$p+^{4}He \rightarrow \pi^+ \ldots$	185
			$\pi^+ \rightarrow \mu^+ + \nu$	-----
^{10}C	19 sec	1.9	$p+^{16}O \rightarrow ^{10}C+\ldots$	41.4
			$p+^{14}N \rightarrow ^{10}C+\ldots$	17.1
			$p+^{12}C \rightarrow ^{10}C+\ldots$	34.4
^{11}C	20.5 min	0.92	$p+^{16}O \rightarrow ^{11}C+\ldots$	27.5
			$p+^{14}N \rightarrow ^{11}C+\ldots$	3.1
			$p+^{12}C \rightarrow ^{11}C+\ldots$	17.9
^{12}N	0.011 sec	16.4	$p+^{12}C \rightarrow ^{12}N+n$	19.6
^{13}N	10 min	1.19	$p+^{16}O \rightarrow ^{13}N+\ldots$	5.5
			$p+^{14}N \rightarrow ^{13}N+\ldots$	9.0
^{14}O	71 sec	1.8(99.4%)	$p+^{16}O \rightarrow ^{14}O+\ldots$	30.7
		4.1(0.6%)	$p+^{14}N \rightarrow ^{14}O+n$	6.3
^{15}O	2.06 min	1.74	$p+^{16}O \rightarrow ^{15}O+\ldots$	14.3
			$\alpha+^{12}C \rightarrow ^{15}O+n$	2.8
^{19}Ne	17.4 sec	2.2	$\alpha+^{16}O \rightarrow ^{19}Ne+n$	3.75

FIGURE CAPTIONS

1. Neutron production cross sections

2. Partial neutron production modes in the thin-target model with power-law spectra

3. Partial neutron production modes in the thin-target model with exponential spectra

4. Total neutron production in the thin and thick-target models with power-law and exponential spectra

5. Probabilities for neutron escape, decay, and capture in the solar atmosphere (solid lines), and photon yields per neutron (dashed lines) for no ^{3}He in the photosphere

6. Probabilities for neutron escape, decay, and capture in the solar atmosphere (solid line), and photon yields per neutron (dashed lines) for $^3\mathrm{He/H} = 5\times10^{-5}$

7. Neutron production energy spectra in the thin-target model with power-law spectra

8. Neutron production energy spectra in the thin-target model with exponential spectra

9. The average, $\bar{f}$, 2.2 MeV photon yield per neutron in the thin and thick-target model, with power-law and exponential spectra, and with $^3\mathrm{He/H} = 0$ and $^3\mathrm{He/H} = 5\times10^{-5}$ in the photosphere.

10. $^{12}C^*$ and $^{16}O^*$ production cross sections

11. $^{12}C^*$ and $^{16}O^*$ partial production modes in the thin-target model with power-law spectra

12. $^{12}C^*$ and $^{16}O^*$ partial production modes in the thin-target model with exponential spectra

13. Ratios of the $^{12}C^{*4.43}$ yield to the total neutron yield for the thin and thick-target models, and power-law and exponential spectra.

14. ^{7}Li production cross section in $\alpha\alpha$ reactions

15. Instantaneous bremsstrahlung emission from electrons with power-law spectra

16. Ratios of the 4.4 MeV line intensity to the 2.2 MeV line intensity in the thin and thick-target models, with power-law and exponential spectra, and with $^3\mathrm{He/H} = 0$ in the photosphere. The shaded region is the data of Chupp et al. (1975)

17. Ratios of the 4.4 MeV line intensity to the 2.2 MeV line intensity in the thin and thick-target models, with power-law and exponential spectra, and with $^3He/H = 5x10^{-5}$ in the photosphere. The shaded area is the data of Chupp et al. (1975).

18. The 2.2 MeV line intensity at Earth in the thin and thick-target models for power-law and exponential spectra and $^3He/H = 0$.

19. The 2.2 MeV line intensity at Earth in the thin and thick-target models for power-law and exponential spectra and $^3He/H = 5x10^{-5}$

20. The observed hard x-ray and gamma-ray continuum emission from the 1972, August 4 flare. The shaded area is data from van Beek et al. (1973), and the data points are from Suri et al. (1974). Curves A, B and C are the bremsstrahlung spectra produced by the corresponding electron spectra shown in Figure 21.

21. Instantaneous electron and proton numbers at the Sun. The electron spectra A, B and C (solid lines) produce the corresponding bremsstrahlung spectra in Figure 20. The dashed lines are proton numbers deduced from line emissions in the thin-target model with $^3He/H = 0$.

22. Energy loss per 4.4 MeV photon at Earth in the thin and thick-target models with power-law and exponential spectra. In both models the power-law spectra are of the form kE^{-S} for $E>Ec$ and kEc^{-S} for $E<Ec$.

23. Radioactive positron emitter production cross sections.

24. Partial positron production modes in the thin-target model with power-law spectra

25. Ratios of the π^+ meson yields to the total positron yields for the thin and thick-target models, and the power-law and exponential spectra

26. Ratios of the total positron yield to the total neutron yield for the thin and thick-target models, and power law and exponential spectra

27. Positron free-annihilation rate and positronium formation rate in a hydrogen plasma

28. Instantaneous pair production rates by relativistic electrons

29. Ratios of the gamma-ray yield from π° decay to the total neutron yield for the thin and thick-target models and power-law and exponential spectra

30. Ratios at Earth of the time-integrated fluxes of neutrons to 2.2 MeV photons, in the thin and thick-target models with power-law and exponential spectra for isotopic neutron release at the Sun and $^3He/H = 5x10^{-5}$

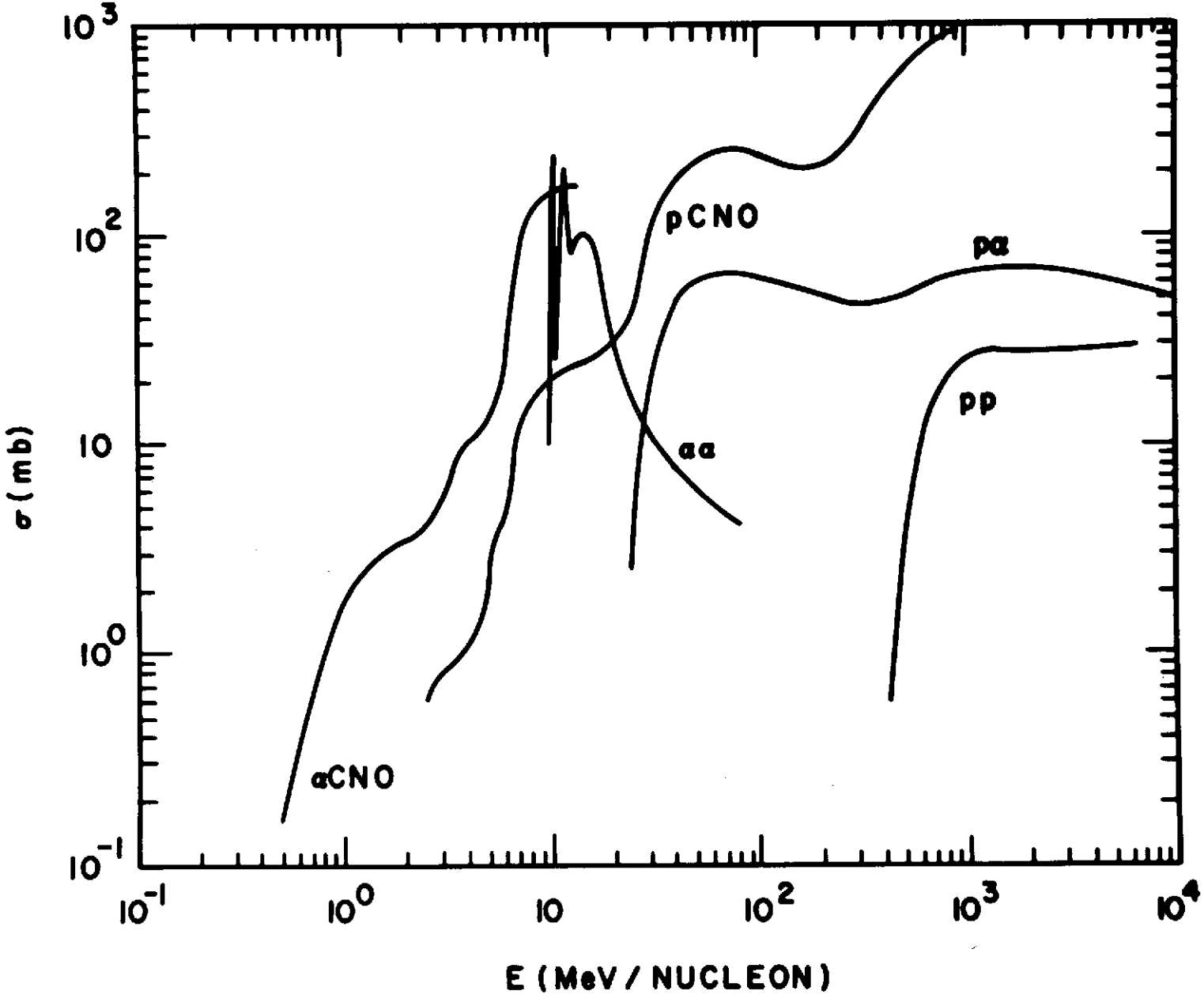
10^3
10^2
10
10^0
10^{-1}
σ (mb)
pCNO
pα
αα
pp
αCNO
10^{-1}
10^0
10
10^2
10^3
10^4
E (MeV / NUCLEON)

FIGURE 1

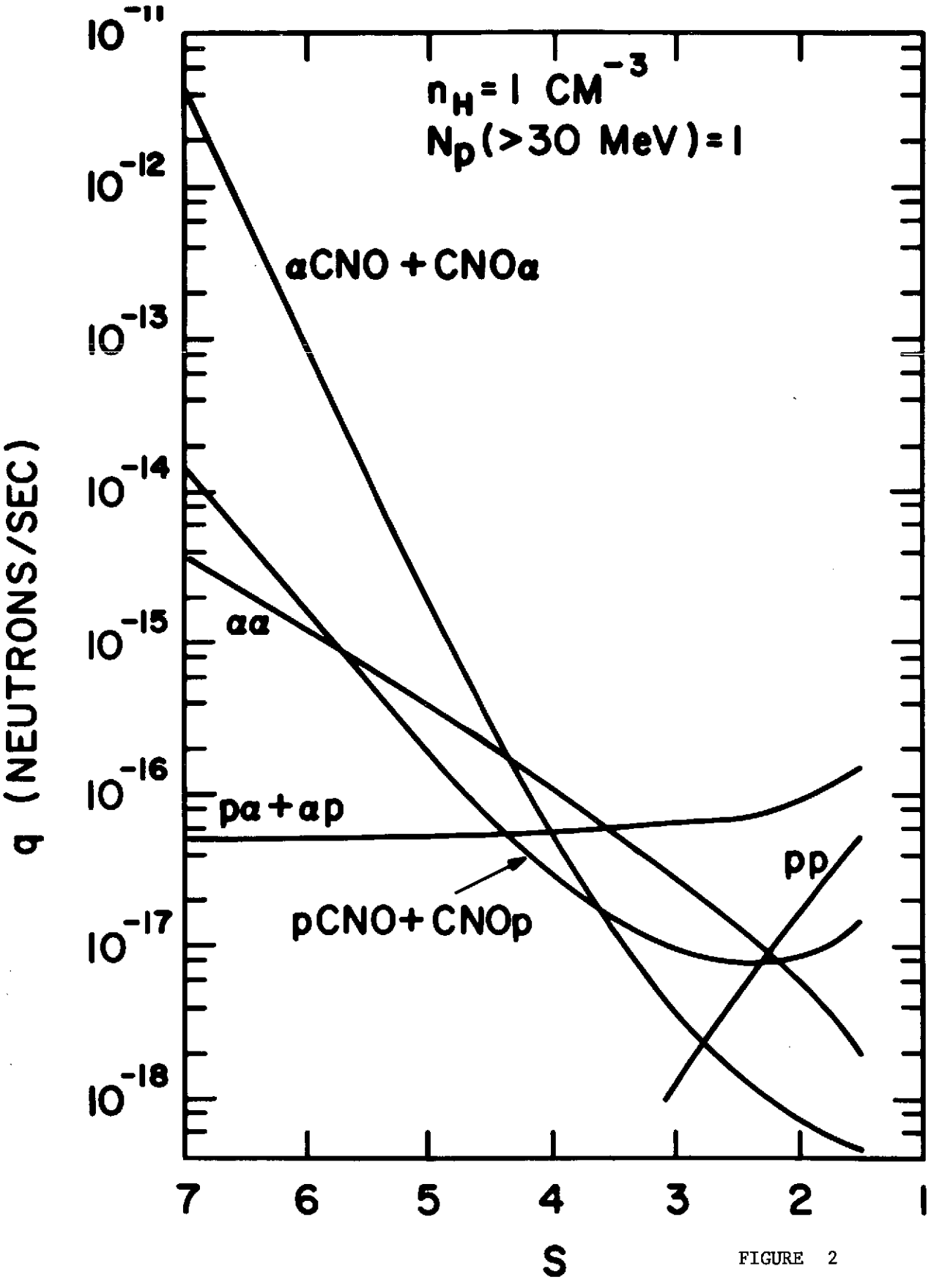
$n_H = 1\ CM^{-3}$
$N_p(>30\ MeV) = 1$
αCNO + CNOα
αα
pα + αp
pCNO + CNOp
pp
q (NEUTRONS/SEC)
10^{-11}
10^{-12}
10^{-13}
10^{-14}
10^{-15}
10^{-16}
10^{-17}
10^{-18}
7
6
5
4
3
2
1
S

FIGURE 2

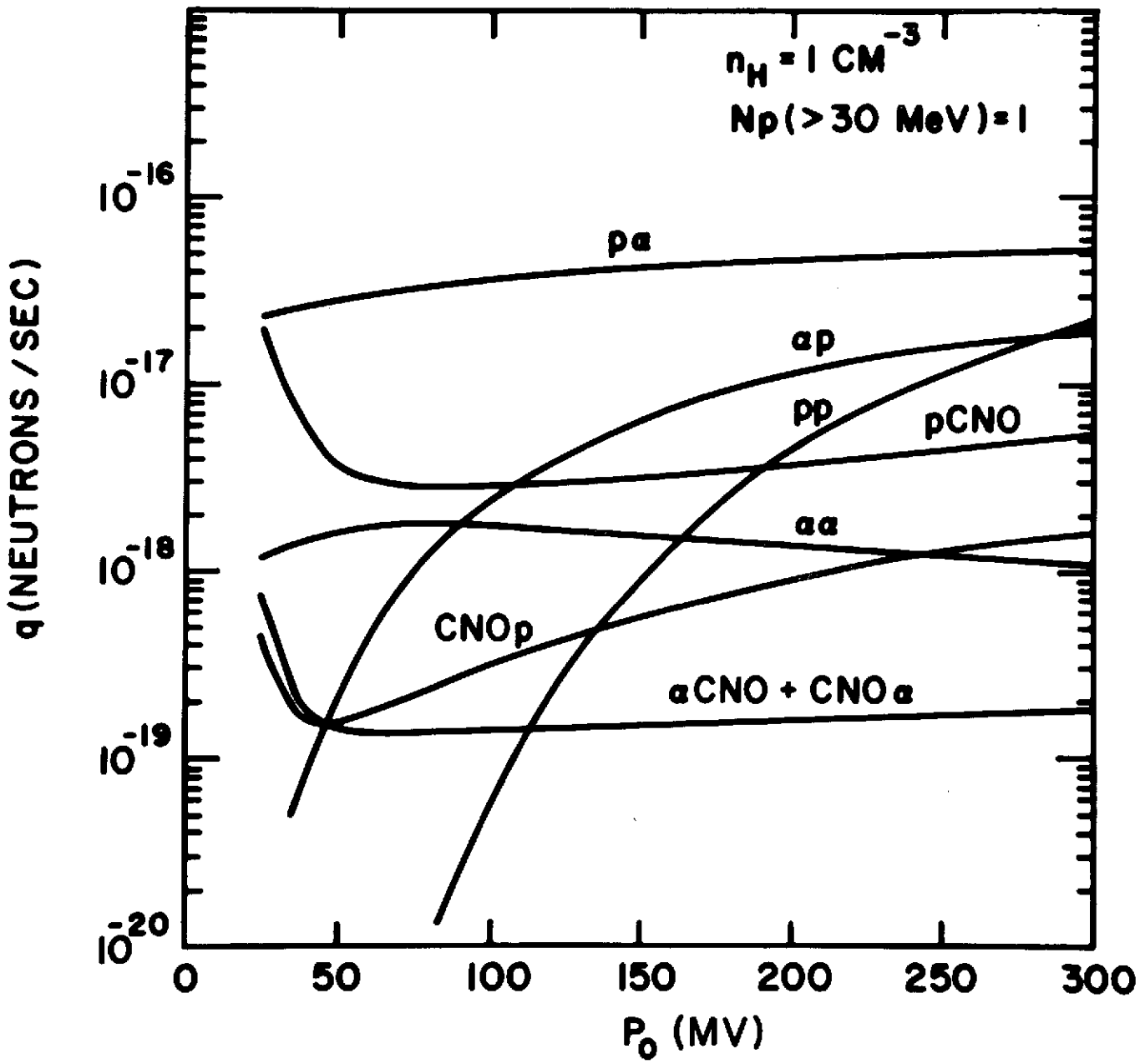
$n_H = 1\ CM^{-3}$
Np(>30 MeV)=1
pα
αp
pp
pCNO
αα
CNOp
αCNO + CNOα
q(NEUTRONS/SEC)
10^{-16}
10^{-17}
10^{-18}
10^{-19}
10^{-20}
0
50
100
150
200
250
300
P_0 (MV)

FIGURE 3

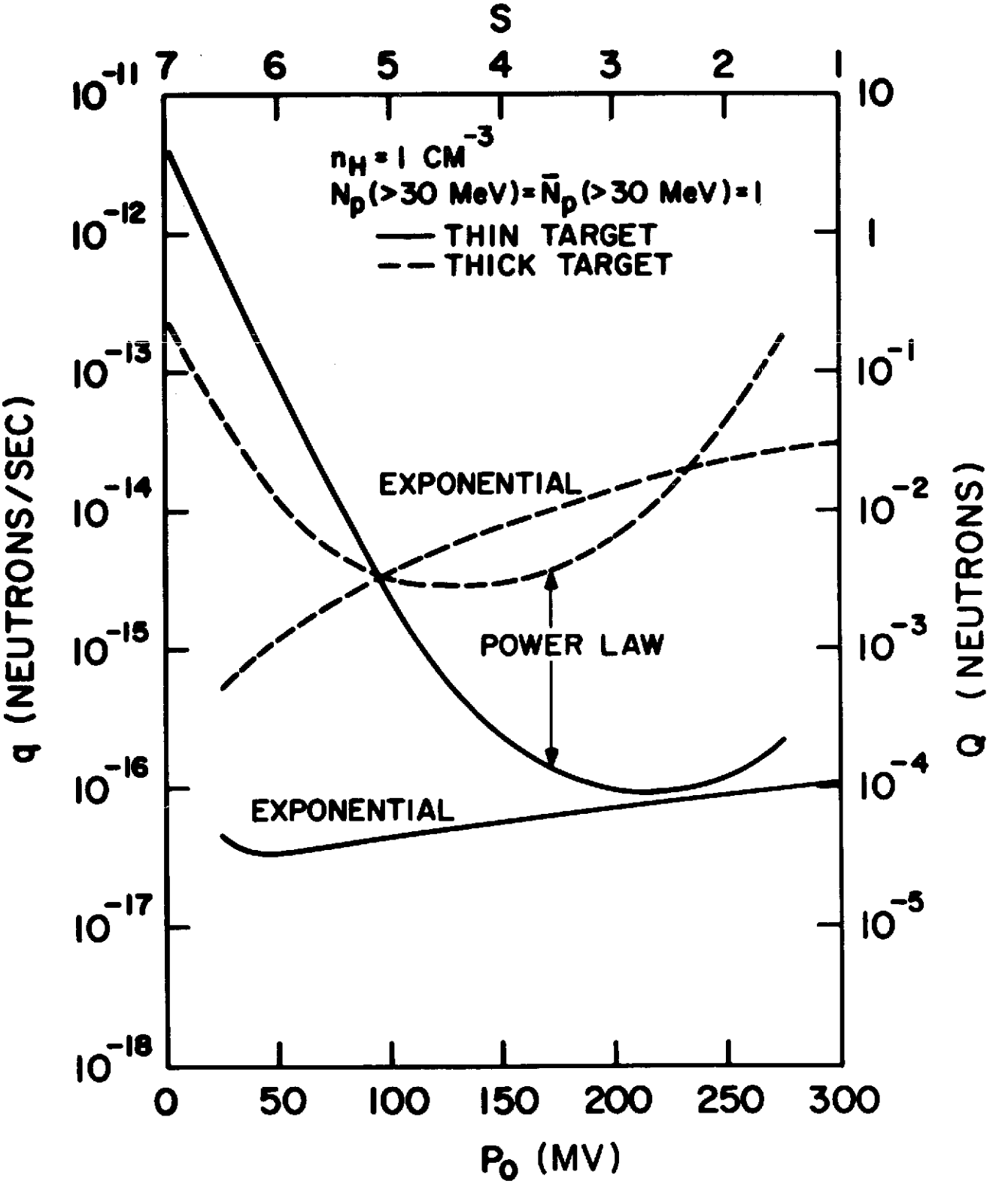
S
7
6
5
4
3
2
1
10^{-11}
10^{-12}
10^{-13}
10^{-14}
10^{-15}
10^{-16}
10^{-17}
10^{-18}
10
1
10^{-1}
10^{-2}
10^{-3}
10^{-4}
10^{-5}
$n_H = 1\ CM^{-3}$
$N_p(>30\ MeV) = \bar{N}_p(>30\ MeV) = 1$
THIN TARGET
THICK TARGET
EXPONENTIAL
POWER LAW
EXPONENTIAL
q (NEUTRONS/SEC)
Q (NEUTRONS)
0
50
100
150
200
250
300
P_0 (MV)

FIGURE 4

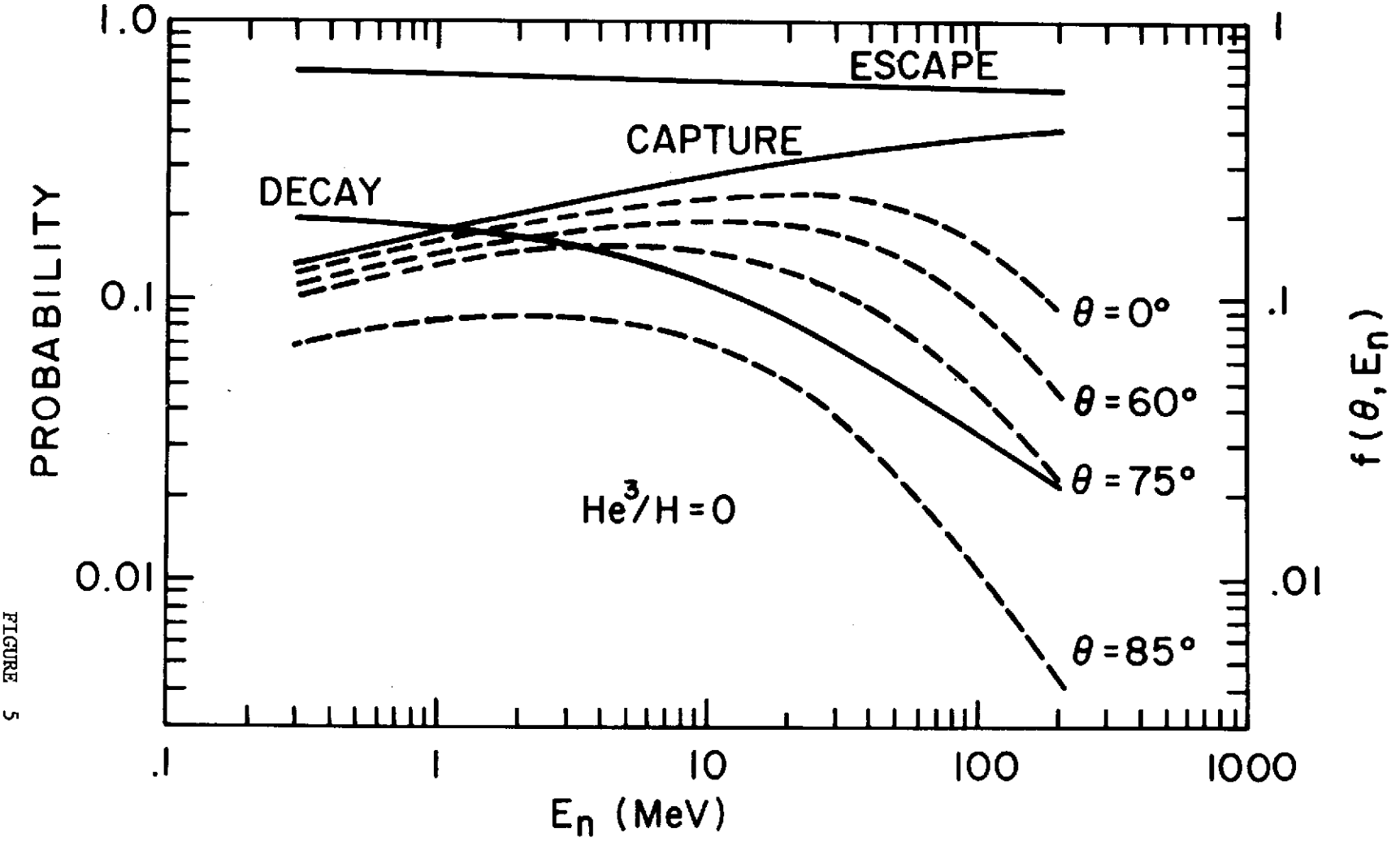
1.0
0.1
0.01
PROBABILITY
ESCAPE
CAPTURE
DECAY
θ = 0°
θ = 60°
θ = 75°
θ = 85°
He³/H = 0
1
.1
.01
f(θ, En)
.1
1
10
100
1000
En (MeV)

FIGURE 5

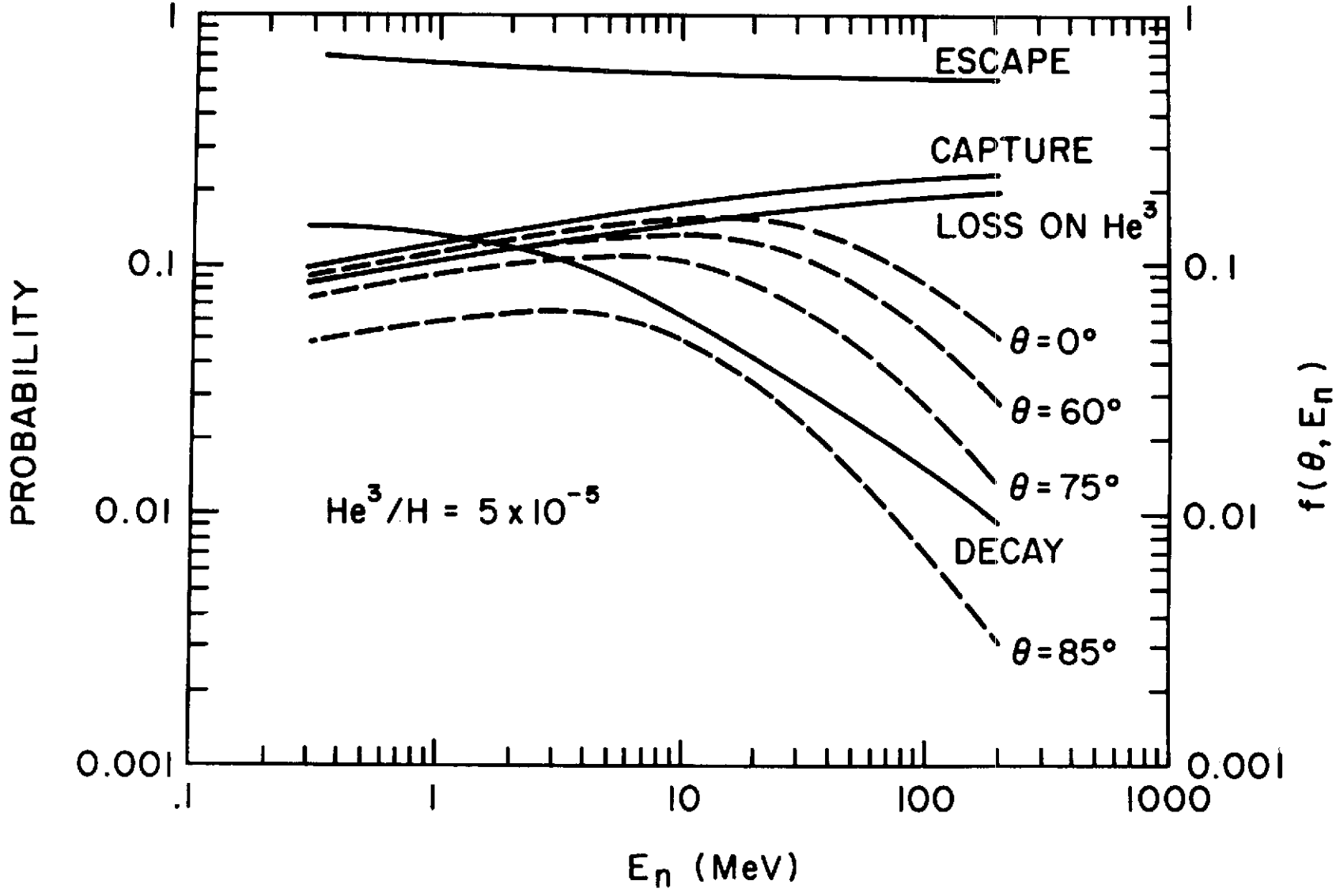
PROBABILITY
1
0.1
0.01
0.001
ESCAPE
CAPTURE
LOSS ON He3
θ = 0°
θ = 60°
θ = 75°
θ = 85°
DECAY
He3/H = 5 x 10-5
.1
1
10
100
1000
En (MeV)
f(θ, En)

FIGURE 6

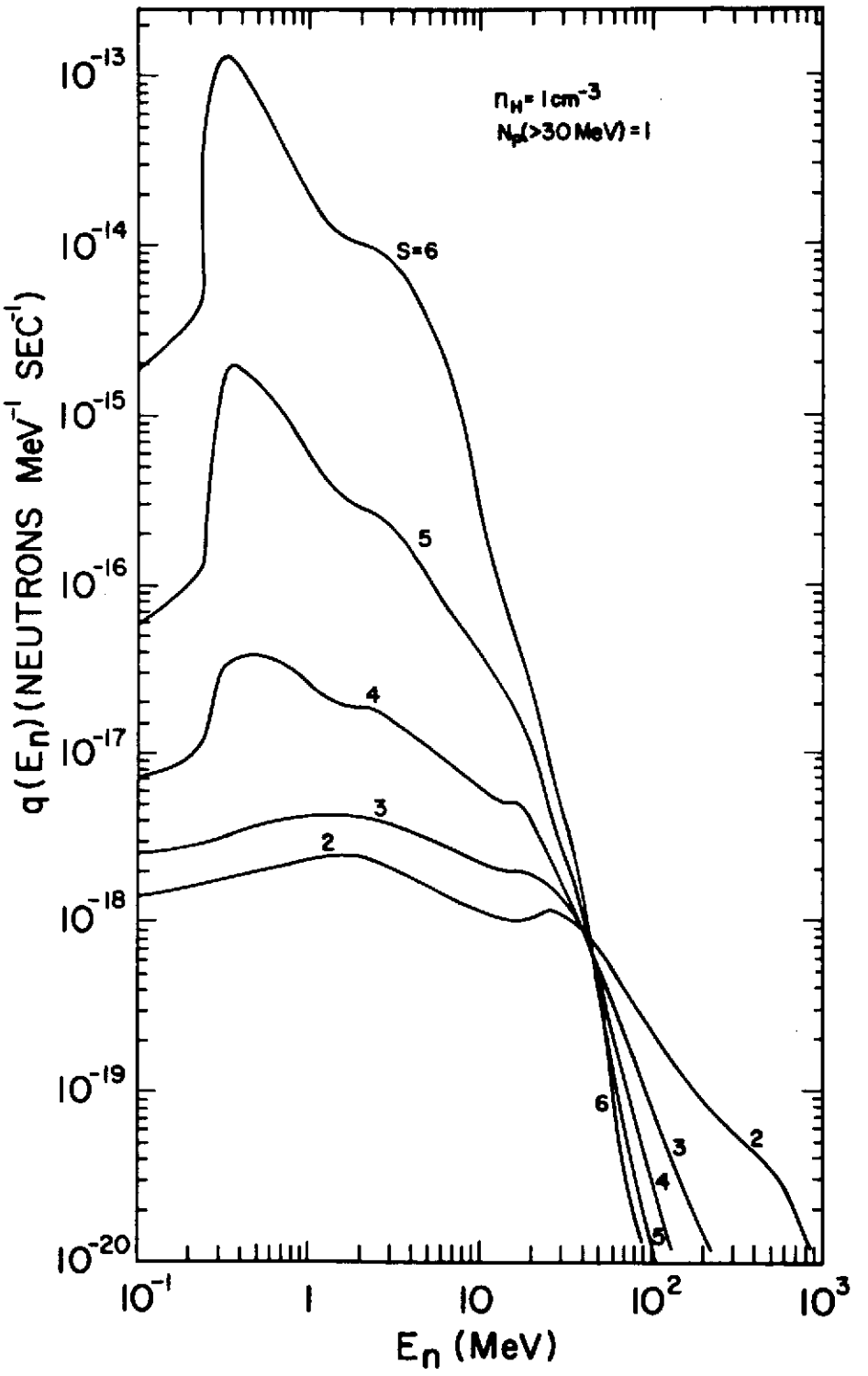
$n_H = 1\,cm^{-3}$
$N_p(>30\,MeV) = 1$
S=6
5
4
3
2
6
3
4
5
2
10^{-13}
10^{-14}
10^{-15}
10^{-16}
10^{-17}
10^{-18}
10^{-19}
10^{-20}
$q(E_n)$(NEUTRONS MeV^{-1} SEC^{-1})
10^{-1}
1
10
10^2
10^3
E_n (MeV)

FIGURE 7

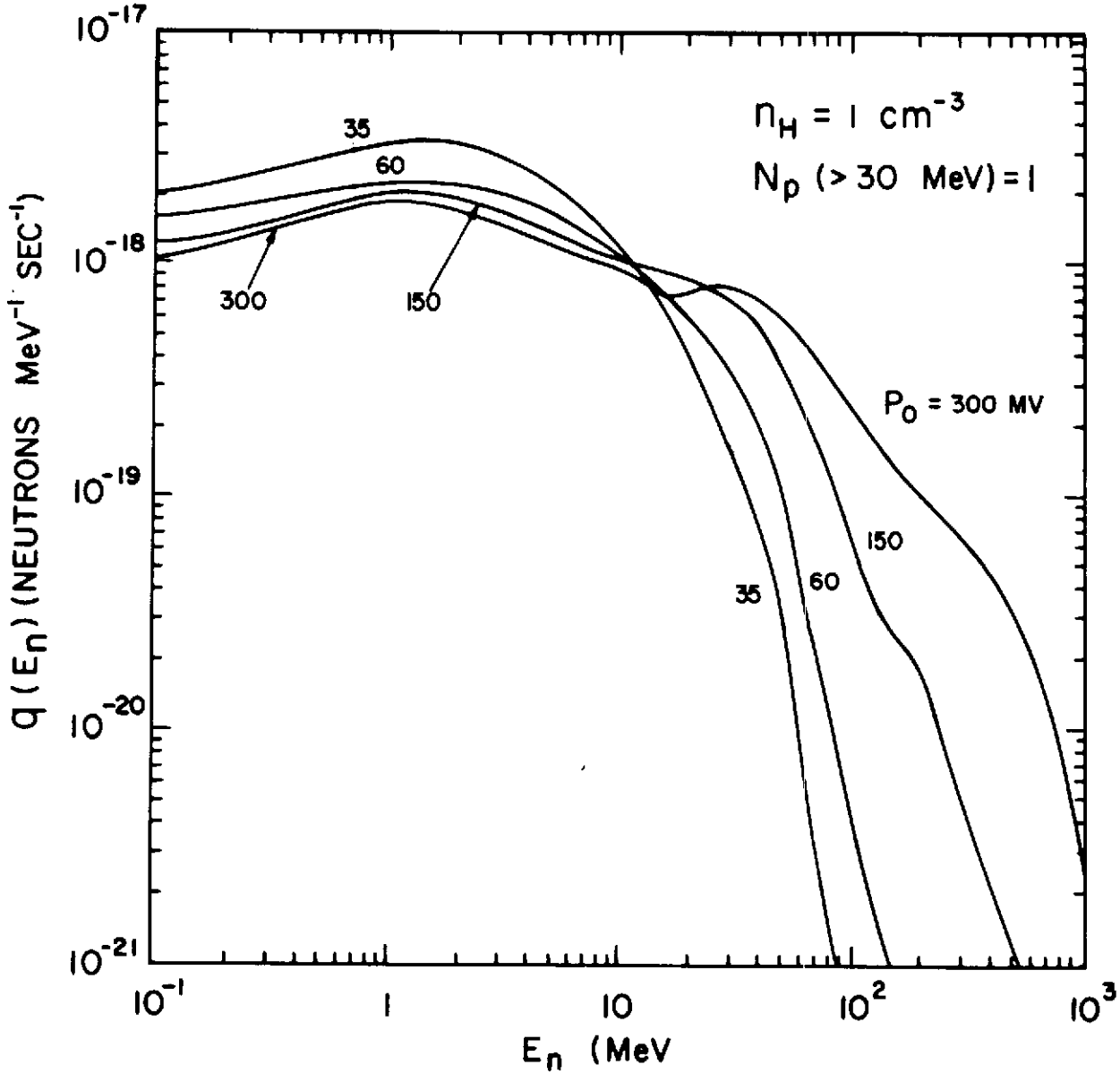
10^{-17}
10^{-18}
10^{-19}
10^{-20}
10^{-21}
$q(E_n)$ (NEUTRONS MeV^{-1} SEC^{-1})
n_H = 1 cm^{-3}
N_p (> 30 MeV) = 1
35
60
150
300
P_0 = 300 MV
10^{-1}
1
10
10^2
10^3
E_n (MeV

FIGURE 8

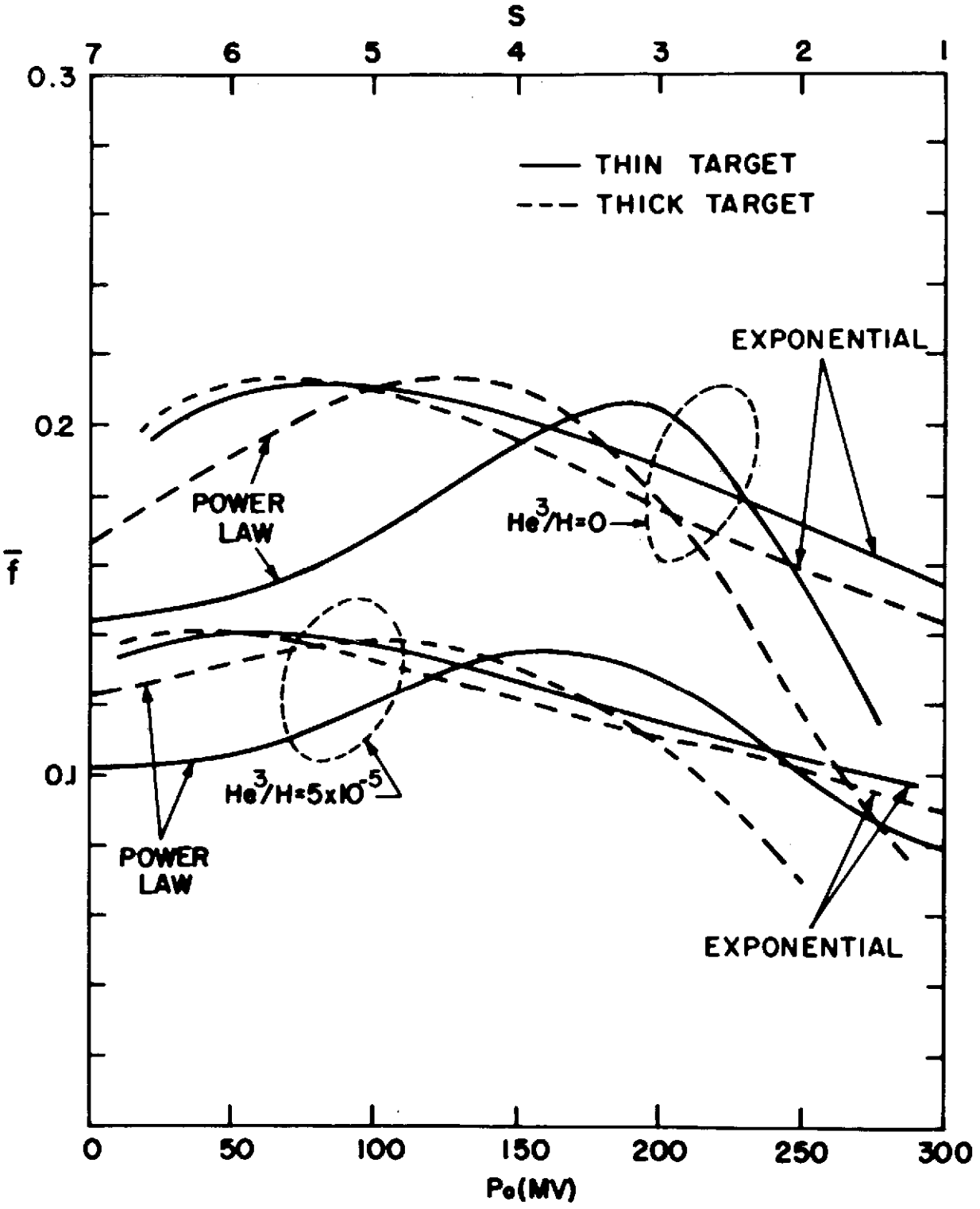
S
7
6
5
4
3
2
1
0.3
0.2
0.1
$\bar{f}$
THIN TARGET
THICK TARGET
EXPONENTIAL
POWER LAW
$He^3/H=0$
$He^3/H=5\times10^{-5}$
POWER LAW
EXPONENTIAL
0
50
100
150
200
250
300
P_o(MV)

FIGURE 9

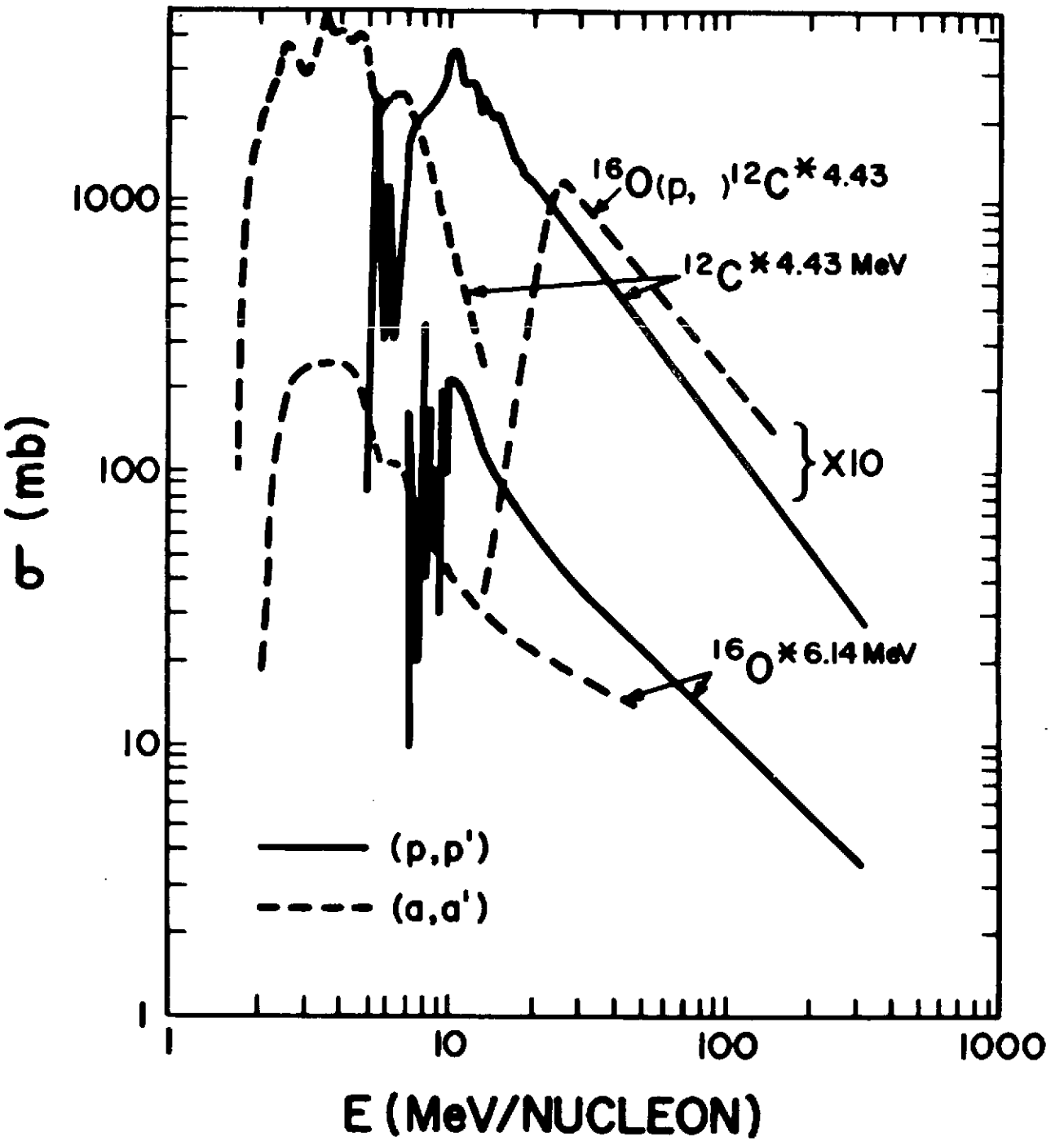
σ (mb)
1000
100
10
1
10
100
1000
E (MeV/NUCLEON)
$^{16}O(p,\ )^{12}C^{*}4.43$
$^{12}C^{*}4.43$ MeV
}X10
$^{16}O^{*}6.14$ MeV
(p,p')
(a,a')

FIGURE 10

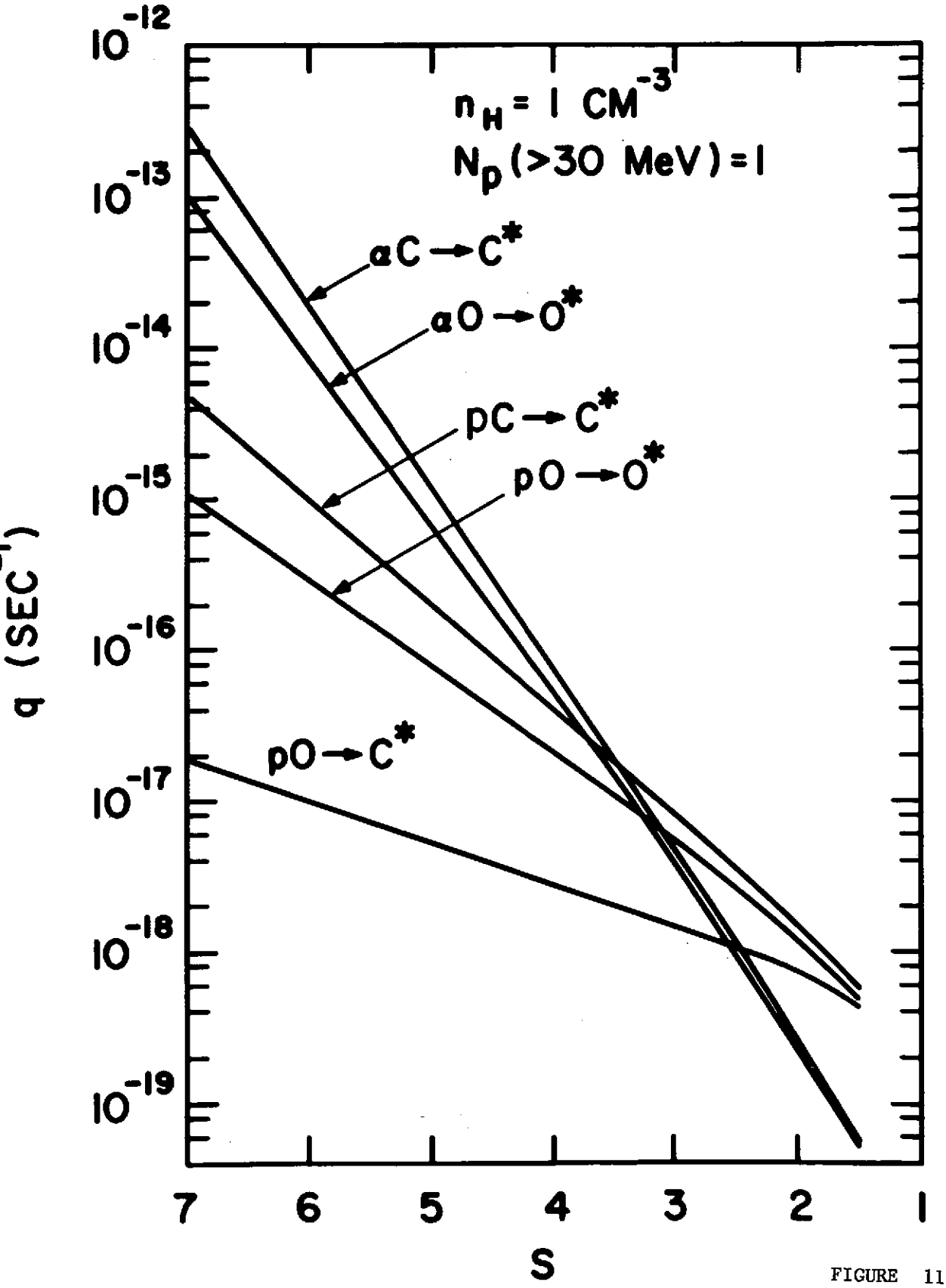
10^{-12}
10^{-13}
10^{-14}
10^{-15}
10^{-16}
10^{-17}
10^{-18}
10^{-19}
q (SEC^{-1})
$n_H = 1$ CM^{-3}
N_p (>30 MeV) = 1
αC → C*
αO → O*
pC → C*
pO → O*
pO → C*
7
6
5
4
3
2
1
S

FIGURE 11

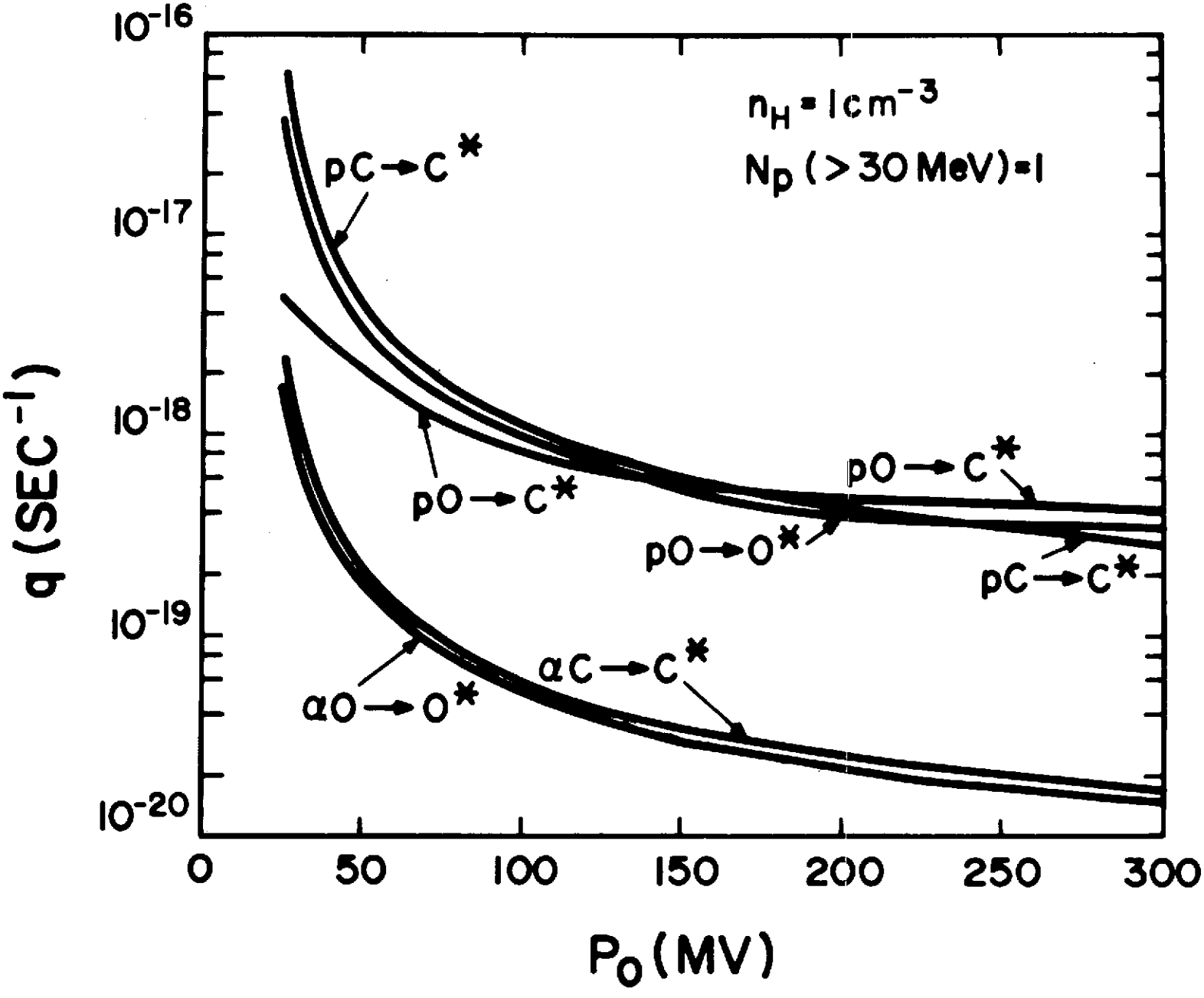
10^{-16}
10^{-17}
10^{-18}
10^{-19}
10^{-20}
q (SEC^{-1})
$n_H = 1 cm^{-3}$
N_p (>30 MeV)=1
pC → C*
pO → C*
pO → C*
pO → O*
pC → C*
αC → C*
αO → O*
0
50
100
150
200
250
300
P_0 (MV)

FIGURE 12

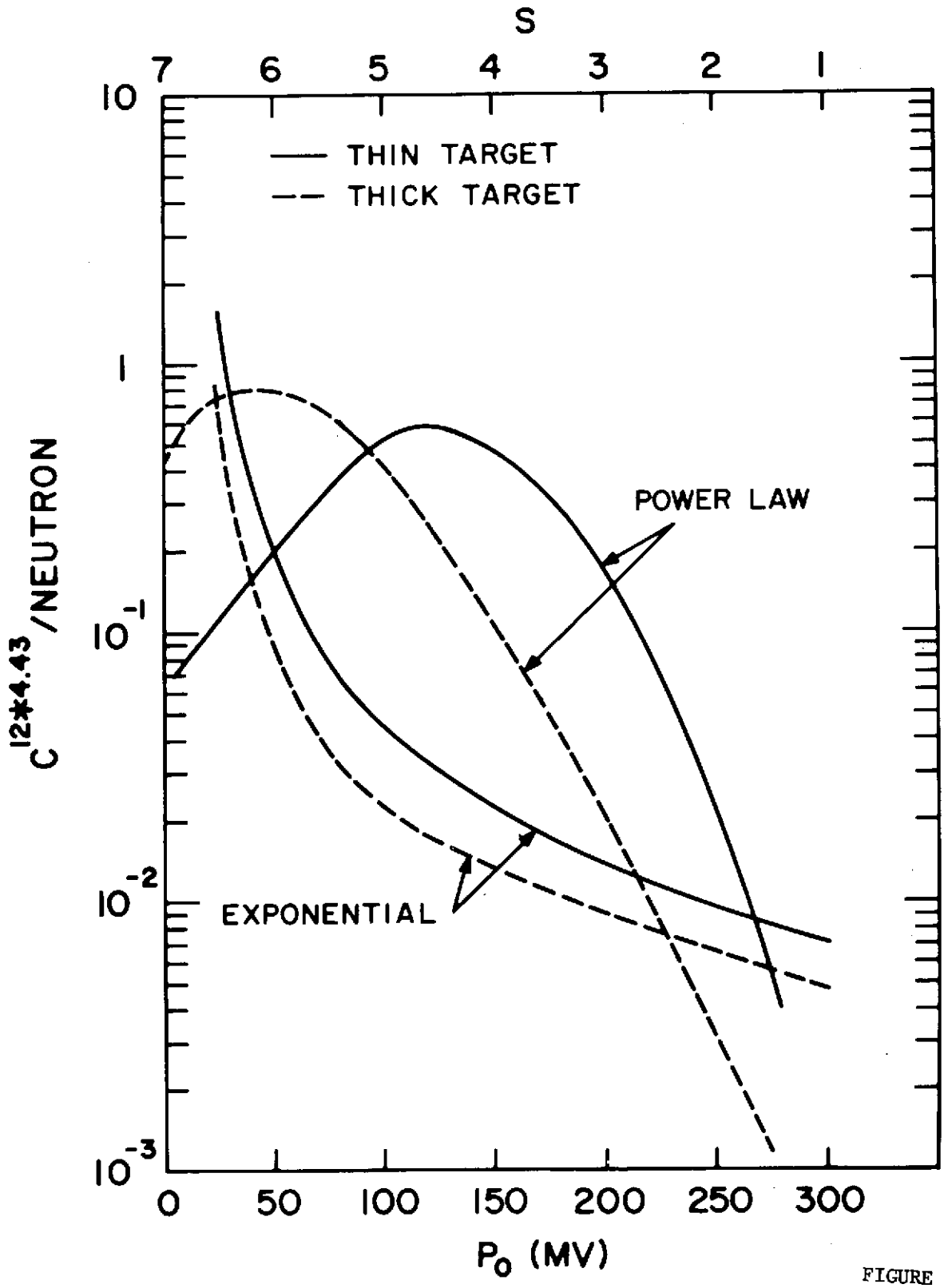
S
7
6
5
4
3
2
1
10
THIN TARGET
THICK TARGET
1
POWER LAW
10^{-1}
$C^{12*4.43}$/NEUTRON
10^{-2}
EXPONENTIAL
10^{-3}
0
50
100
150
200
250
300
P_0 (MV)

FIGURE 13

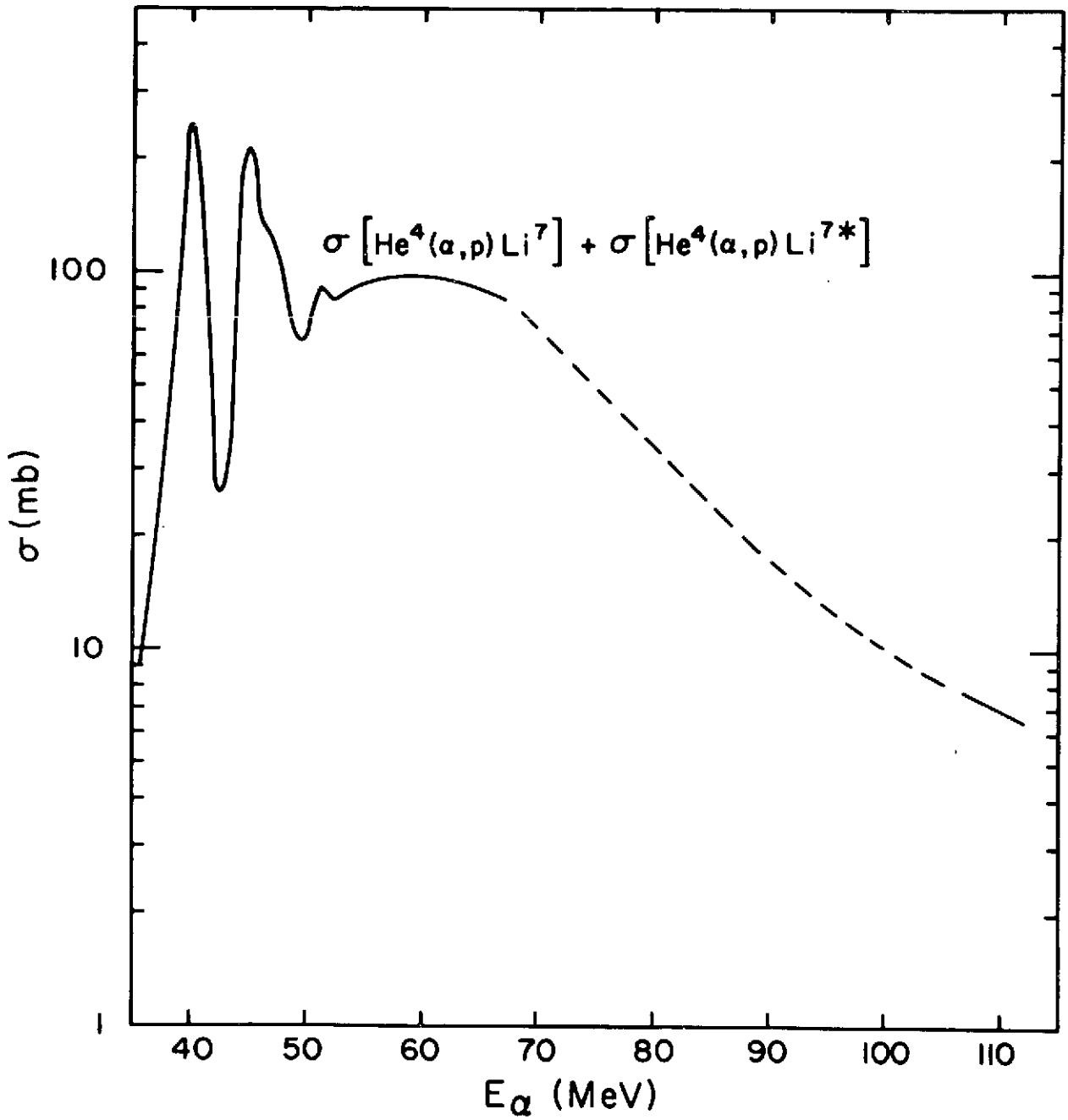
σ [He⁴(α,p) Li⁷] + σ [He⁴(α,p) Li⁷*]
100
10
1
σ (mb)
40
50
60
70
80
90
100
110
Eα (MeV)

FIGURE 14

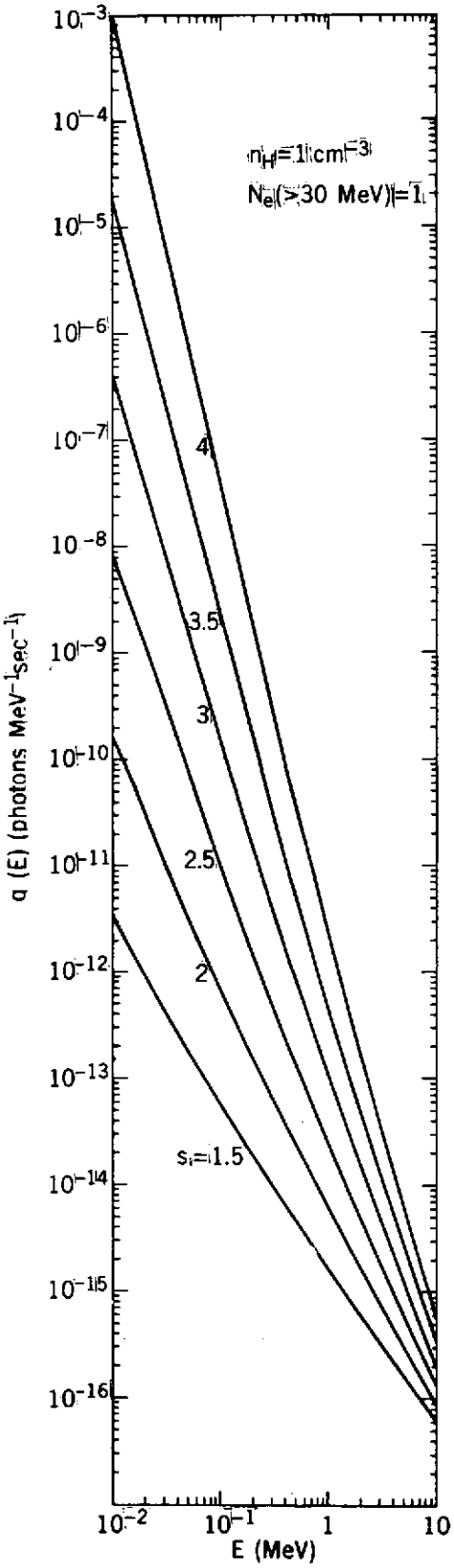
10^{-3}
10^{-4}
10^{-5}
10^{-6}
10^{-7}
10^{-8}
10^{-9}
10^{-10}
10^{-11}
10^{-12}
10^{-13}
10^{-14}
10^{-15}
10^{-16}
n_H=1 cm^{-3}
N_e(≥30 MeV)=1
4
3.5
3
2.5
2
s_i=1.5
10^{-2}
10^{-1}
1
10
E (MeV)
q (E) (photons MeV^{-1}sec^{-1})

FIGURE 15

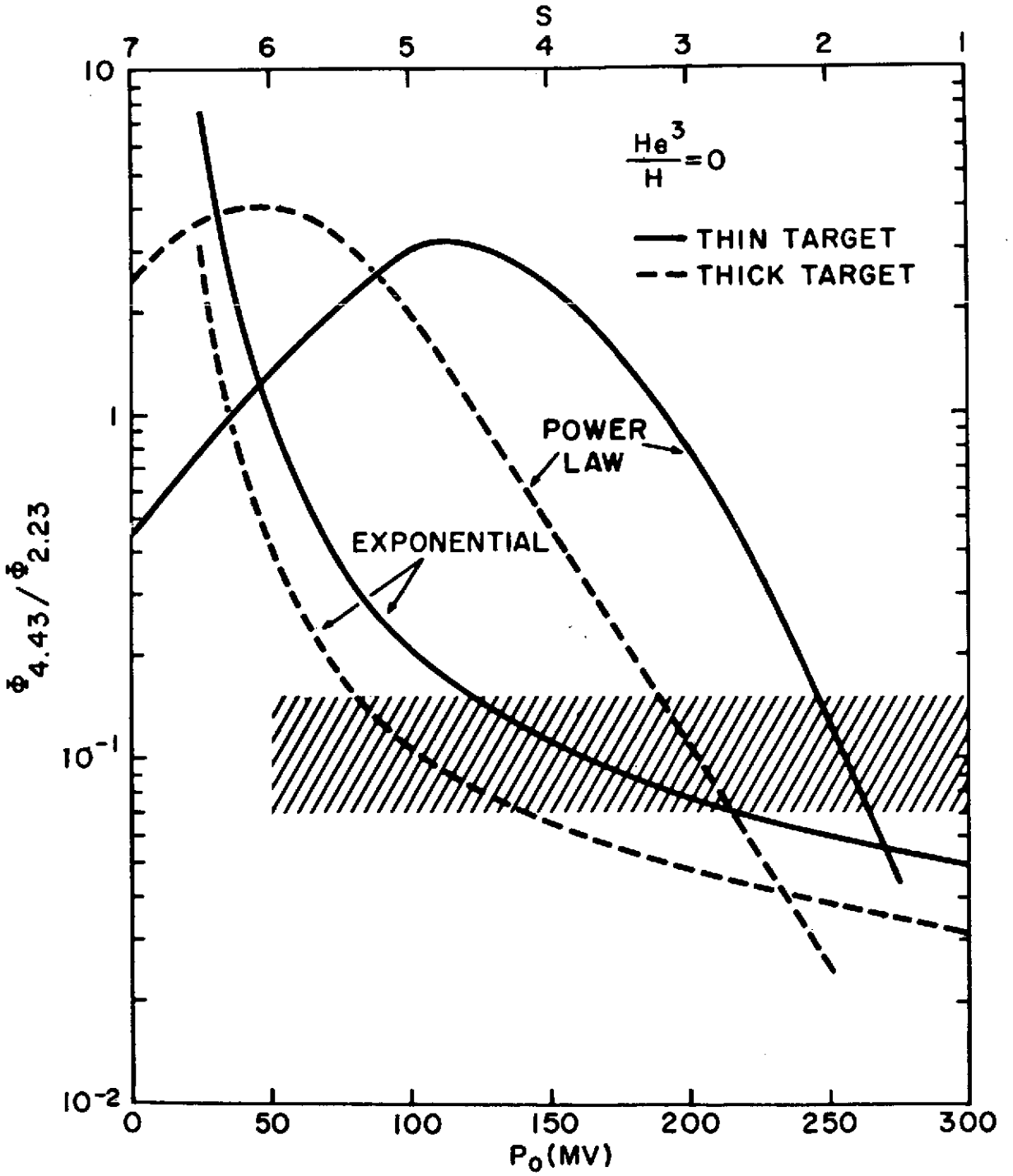
S
7
6
5
4
3
2
1
10
$\frac{He^3}{H}=0$
THIN TARGET
THICK TARGET
POWER LAW
EXPONENTIAL
1
10^{-1}
10^{-2}
$\Phi_{4.43}/\Phi_{2.23}$
0
50
100
150
200
250
300
P_0(MV)

FIGURE 16

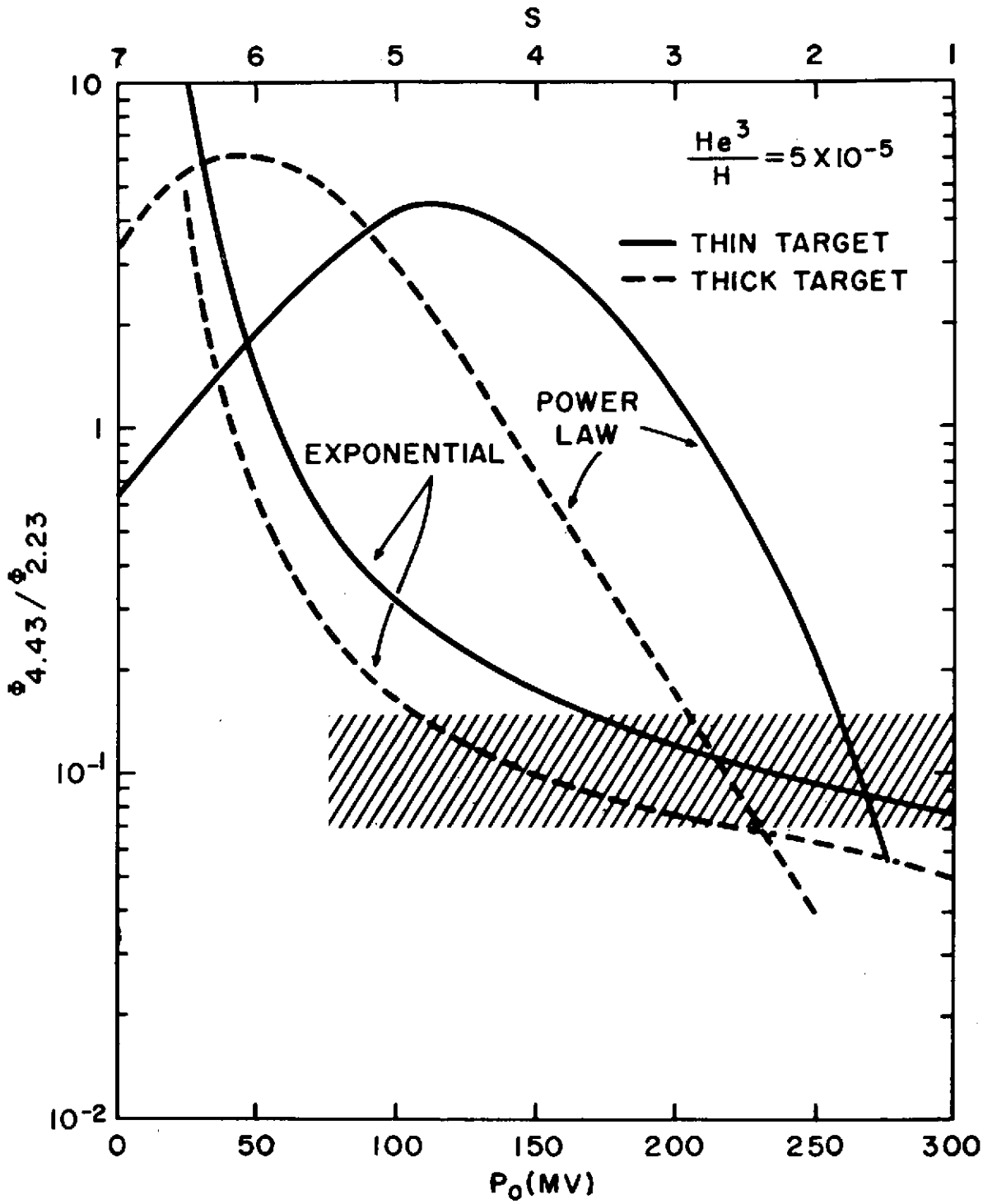
S
7
6
5
4
3
2
1
10
1
10^{-1}
10^{-2}
$\frac{He^3}{H} = 5 \times 10^{-5}$
THIN TARGET
THICK TARGET
POWER LAW
EXPONENTIAL
$\Phi_{4.43}/\Phi_{2.23}$
0
50
100
150
200
250
300
P_0(MV)

FIGURE 17

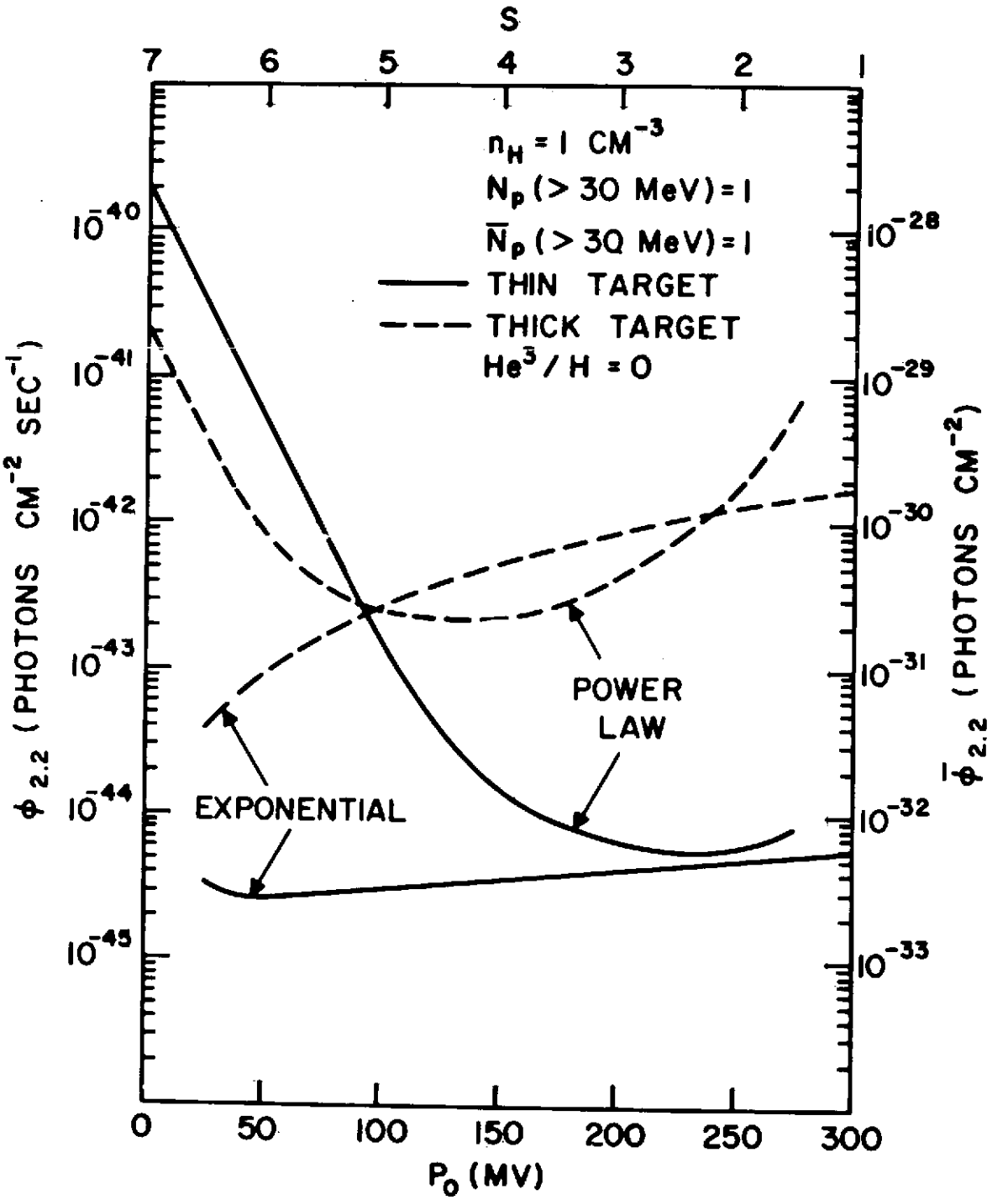
S
7
6
5
4
3
2
1
$n_H = 1\ CM^{-3}$
$N_p (> 30\ MeV) = 1$
$\bar{N}_p (> 30\ MeV) = 1$
THIN TARGET
THICK TARGET
$He^3 / H = 0$
POWER LAW
EXPONENTIAL
$\phi_{2.2}$ (PHOTONS CM^{-2} SEC^{-1})
$\bar{\phi}_{2.2}$ (PHOTONS CM^{-2})
10^{-40}
10^{-41}
10^{-42}
10^{-43}
10^{-44}
10^{-45}
10^{-28}
10^{-29}
10^{-30}
10^{-31}
10^{-32}
10^{-33}
0
50
100
150
200
250
300
P_0 (MV)

FIGURE 18

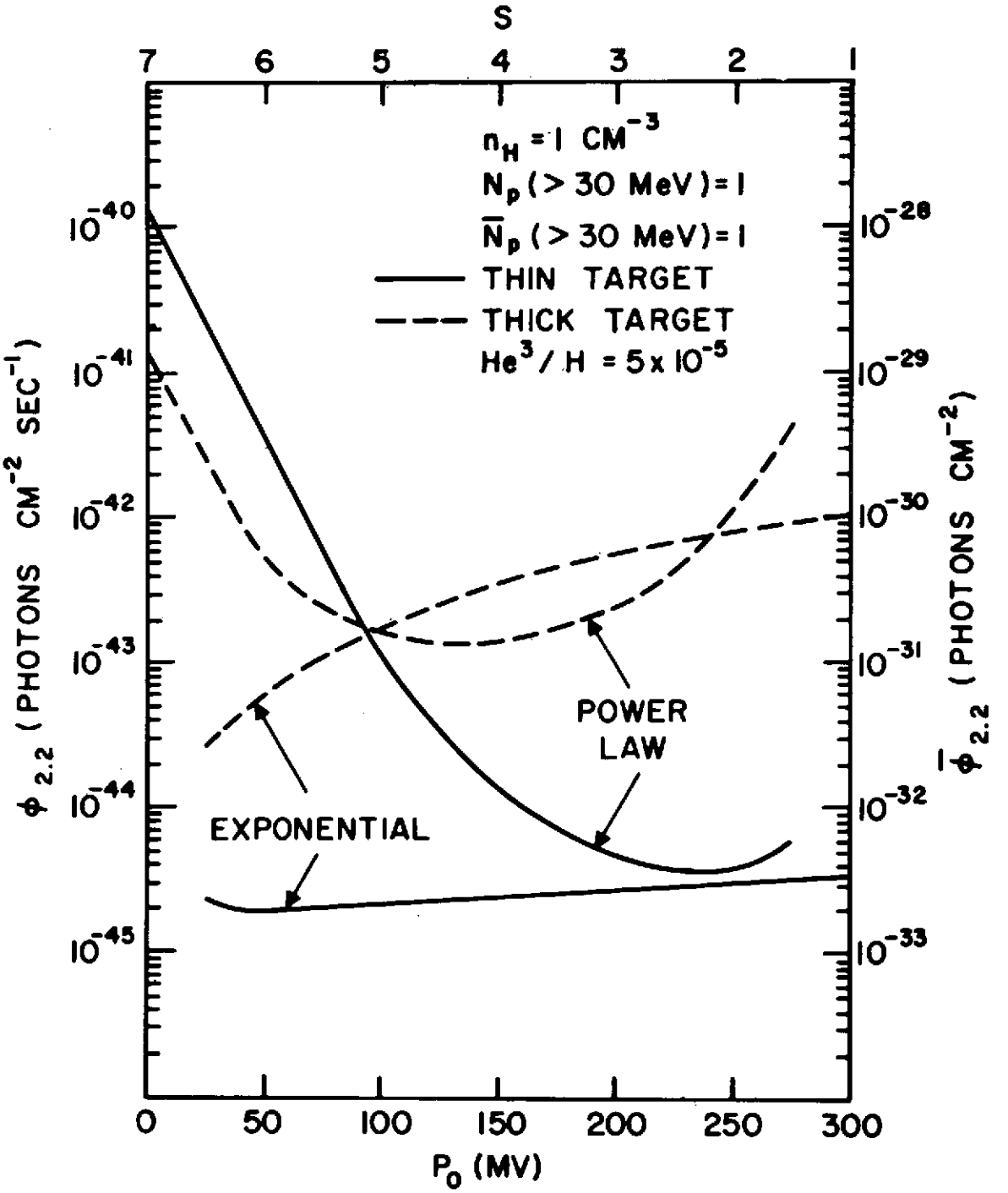
S
7
6
5
4
3
2
1
$n_H = 1\ CM^{-3}$
$N_p (> 30\ MeV) = 1$
$\bar{N}_p (> 30\ MeV) = 1$
THIN TARGET
THICK TARGET
$He^3 / H = 5 \times 10^{-5}$
POWER LAW
EXPONENTIAL
$\phi_{2.2}$ (PHOTONS CM^{-2} SEC^{-1})
$\bar{\phi}_{2.2}$ (PHOTONS CM^{-2})
10^{-40}
10^{-41}
10^{-42}
10^{-43}
10^{-44}
10^{-45}
10^{-28}
10^{-29}
10^{-30}
10^{-31}
10^{-32}
10^{-33}
0
50
100
150
200
250
300
P_0 (MV)

FIGURE 19

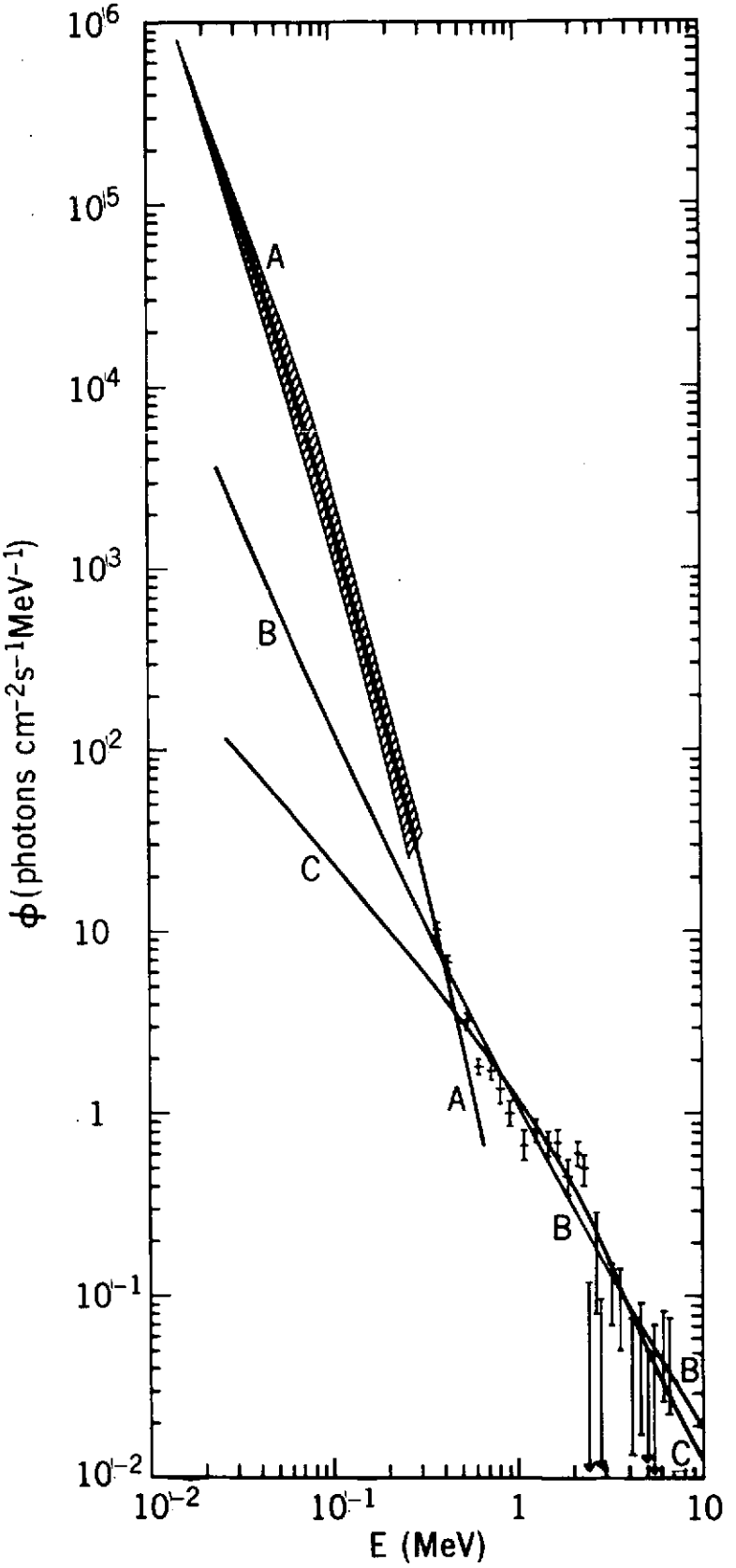
10^6
10^5
10^4
10^3
10^2
10
1
10^{-1}
10^{-2}
ϕ(photons cm^{-2}s^{-1}MeV^{-1})
A
B
C
A
B
B
C
10^{-2}
10^{-1}
1
10
E (MeV)

FIGURE 20

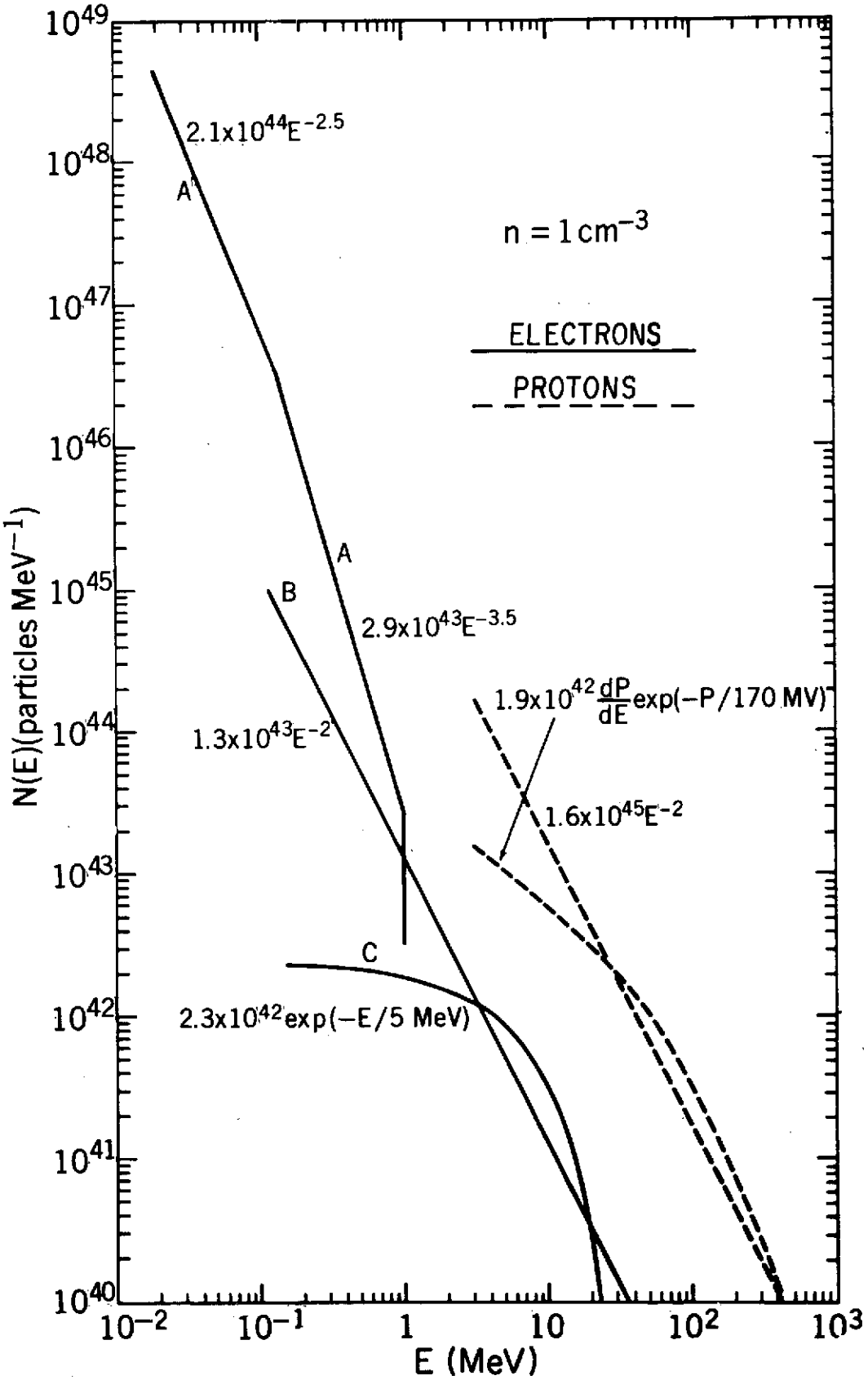
10^{49}
10^{48}
10^{47}
10^{46}
10^{45}
10^{44}
10^{43}
10^{42}
10^{41}
10^{40}
N(E)(particles MeV^{-1})
$2.1\times10^{44}E^{-2.5}$
A'
$n = 1\,cm^{-3}$
ELECTRONS
PROTONS
A
B
$2.9\times10^{43}E^{-3.5}$
$1.9\times10^{42}\frac{dP}{dE}\exp(-P/170\,MV)$
$1.3\times10^{43}E^{-2}$
$1.6\times10^{45}E^{-2}$
C
$2.3\times10^{42}\exp(-E/5\,MeV)$
10^{-2}
10^{-1}
1
10
10^{2}
10^{3}
E (MeV)

FIGURE 21

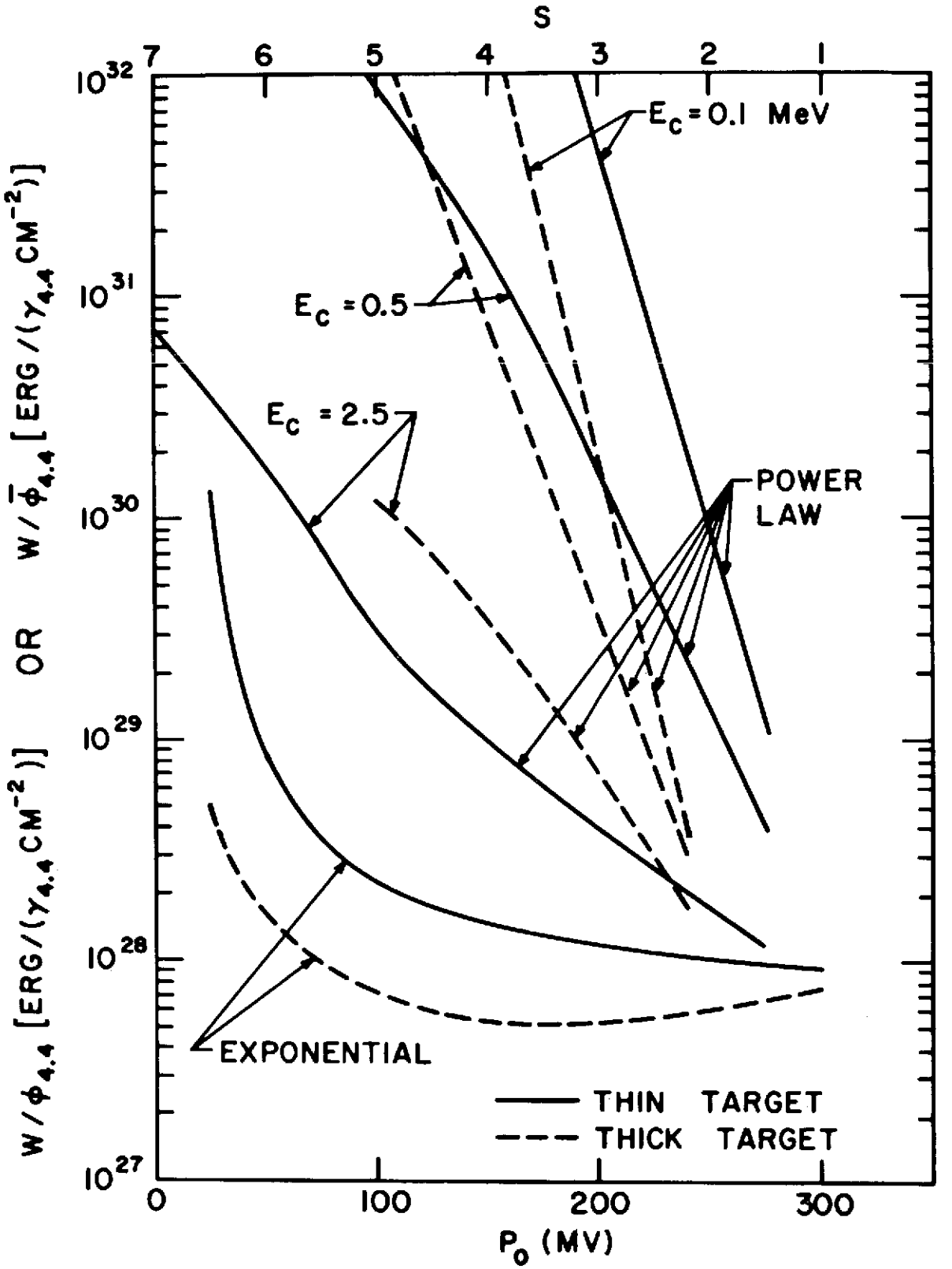
S
7
6
5
4
3
2
1
10^{32}
10^{31}
10^{30}
10^{29}
10^{28}
10^{27}
E_c = 0.1 MeV
E_c = 0.5
E_c = 2.5
POWER LAW
EXPONENTIAL
THIN TARGET
THICK TARGET
0
100
200
300
P_0 (MV)
$W/\phi_{4.4}$ [ERG/($\gamma_{4.4}$ CM^{-2})] OR $W/\bar{\phi}_{4.4}$ [ERG/($\gamma_{4.4}$ CM^{-2})]

FIGURE 22

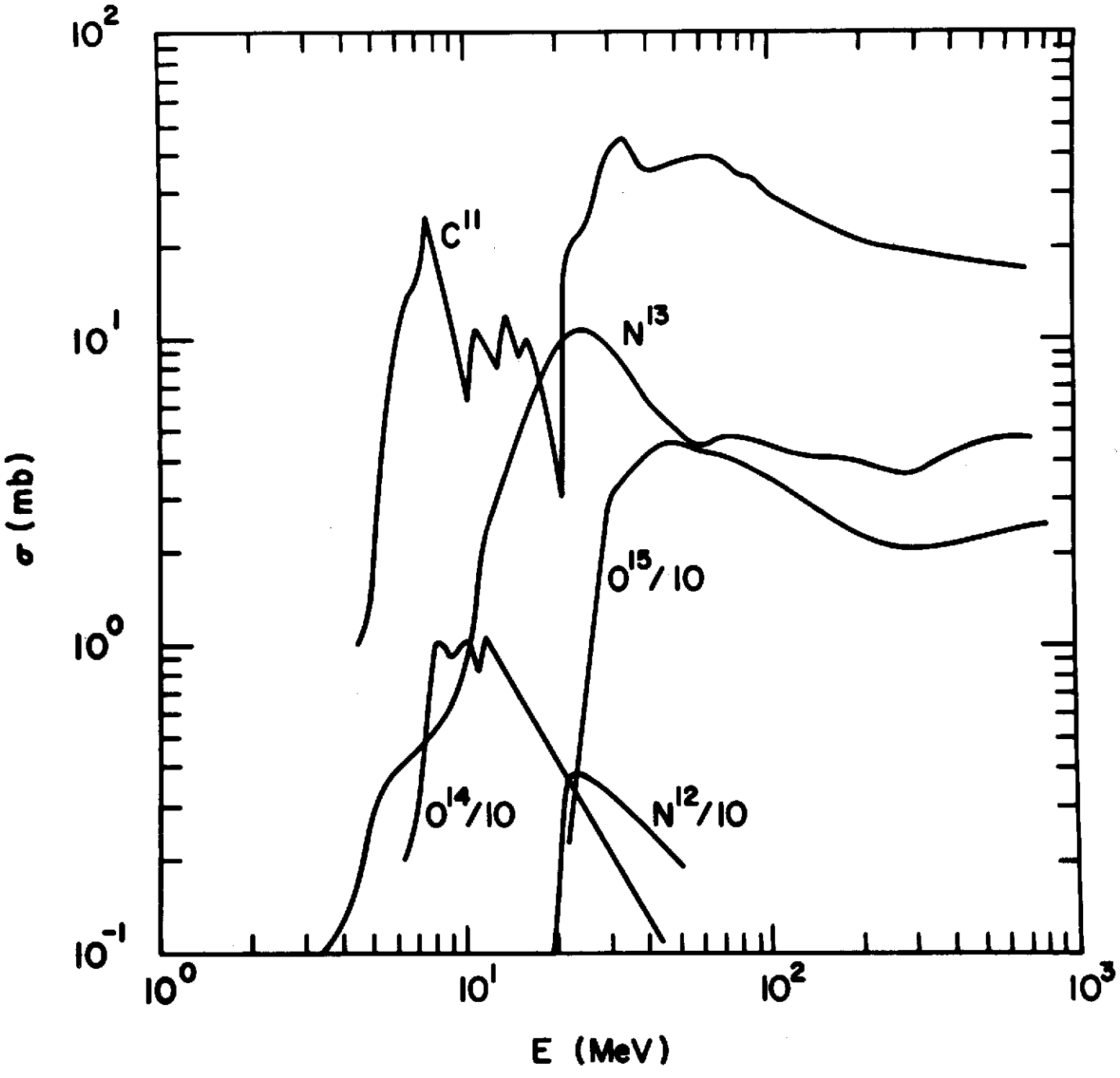
10^2
10^1
10^0
10^{-1}
σ (mb)
C^{11}
N^{13}
$O^{15}/10$
$O^{14}/10$
$N^{12}/10$
10^0
10^1
10^2
10^3
E (MeV)

FIGURE 23

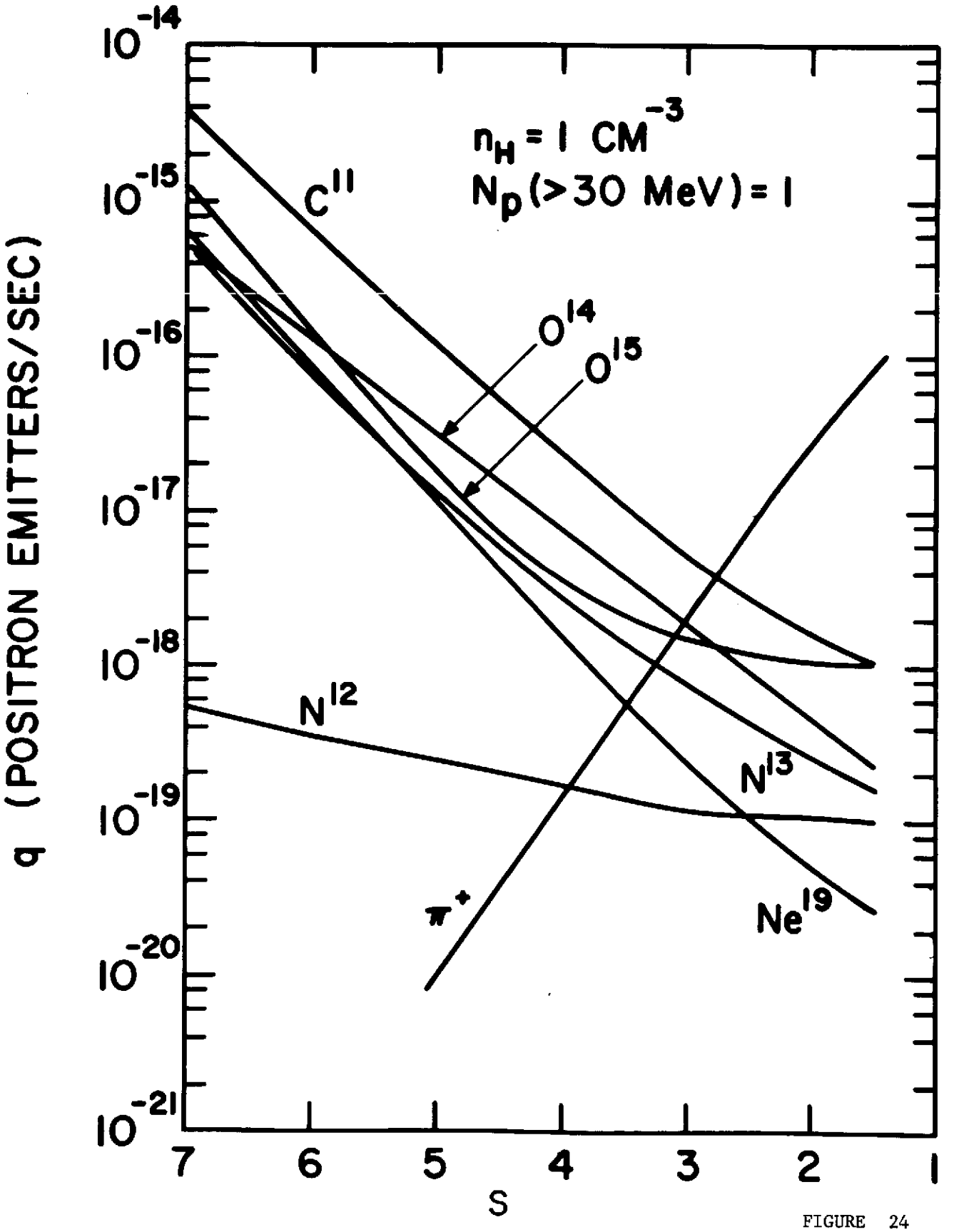
q (POSITRON EMITTERS/SEC)
10^{-14}
10^{-15}
10^{-16}
10^{-17}
10^{-18}
10^{-19}
10^{-20}
10^{-21}
$n_H = 1\ CM^{-3}$
$N_p(>30\ MeV) = 1$
C^{11}
O^{14}
O^{15}
N^{12}
N^{13}
Ne^{19}
π^+
7
6
5
4
3
2
1
S

FIGURE 24

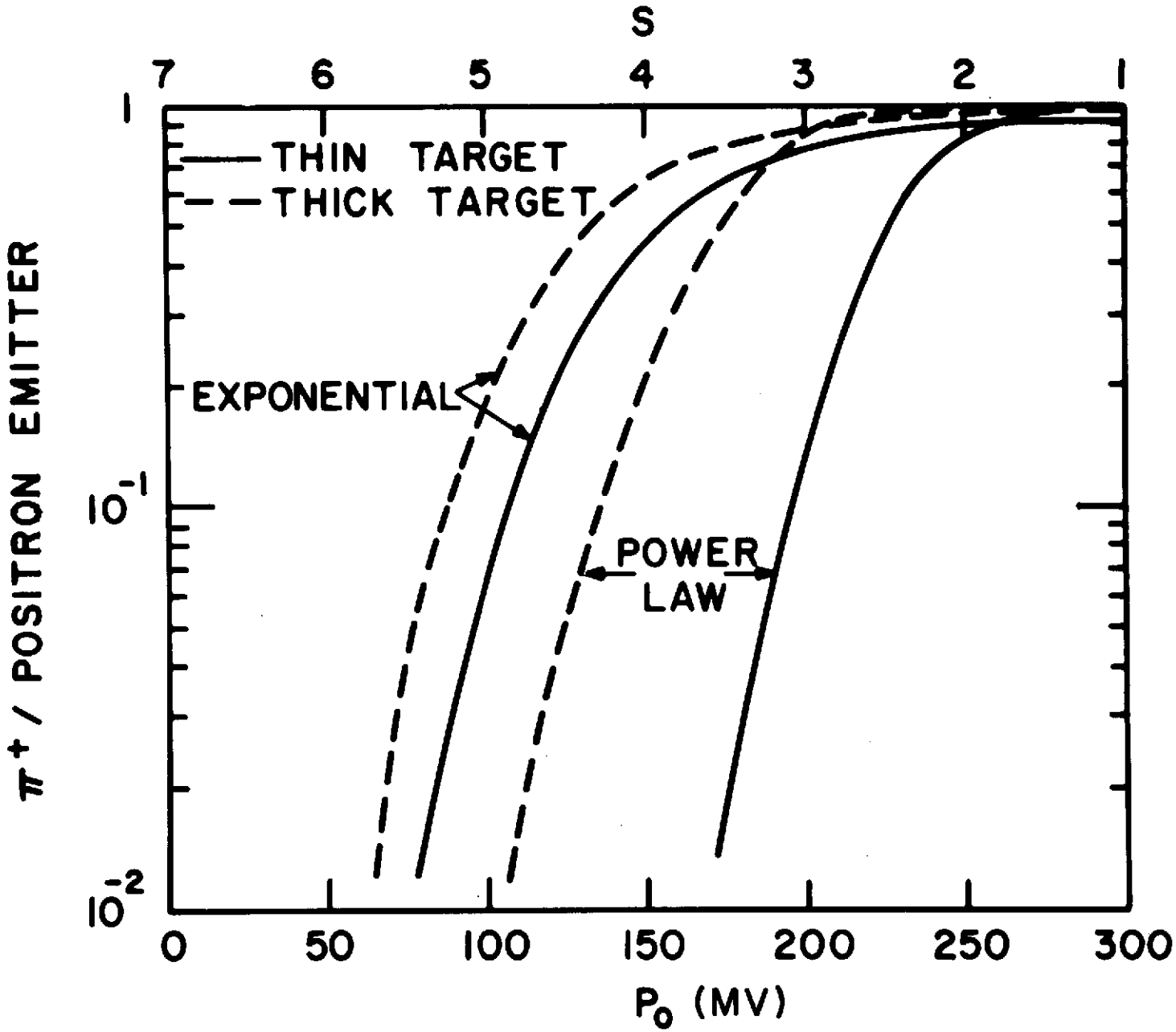
S
7
6
5
4
3
2
1
THIN TARGET
THICK TARGET
EXPONENTIAL
POWER LAW
π^+ / POSITRON EMITTER
10^{-1}
10^{-2}
0
50
100
150
200
250
300
P_0 (MV)

FIGURE 25

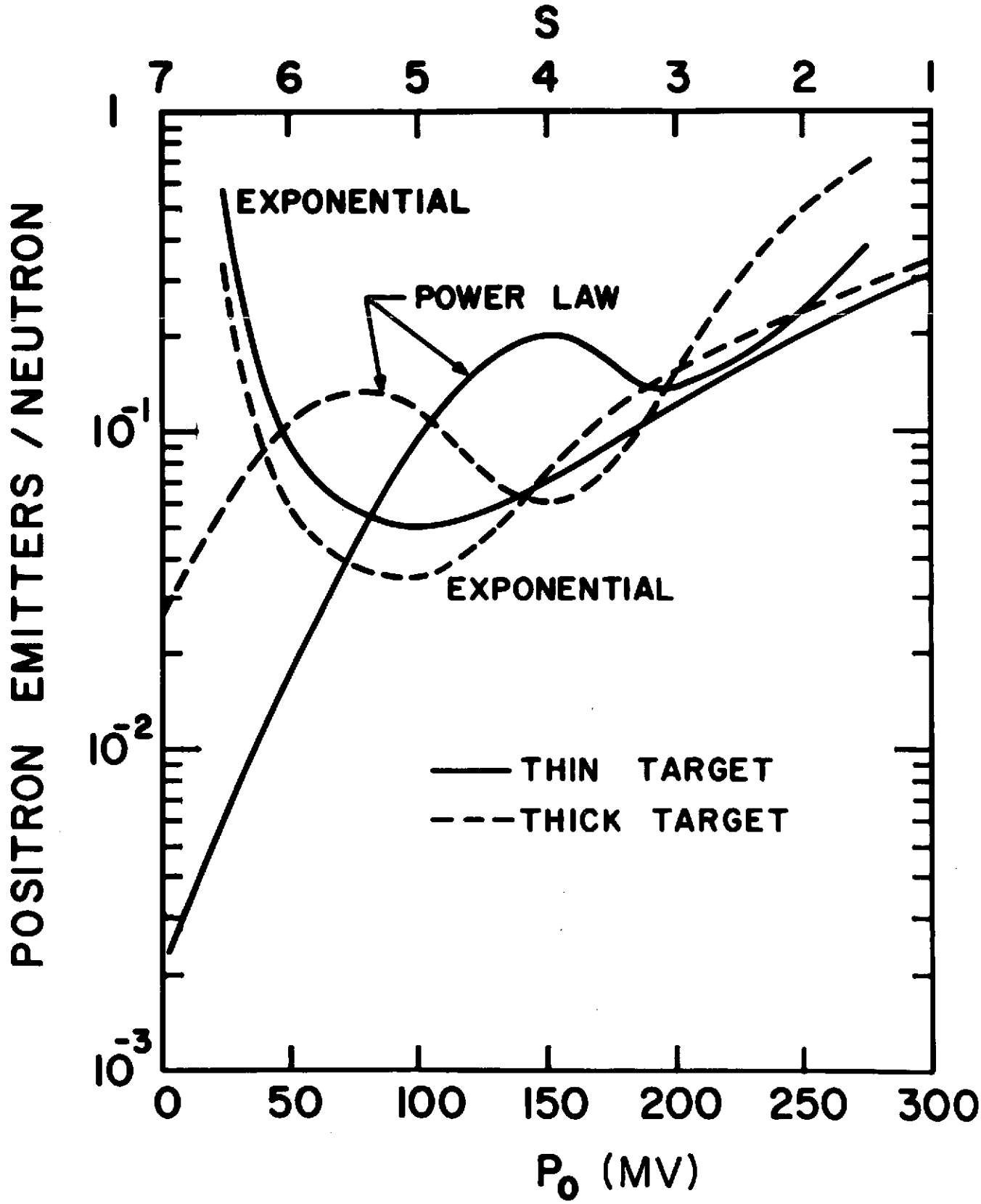
S
7
6
5
4
3
2
1
1
10^{-1}
10^{-2}
10^{-3}
POSITRON EMITTERS / NEUTRON
EXPONENTIAL
POWER LAW
EXPONENTIAL
THIN TARGET
THICK TARGET
0
50
100
150
200
250
300
P_0 (MV)

FIGURE 26

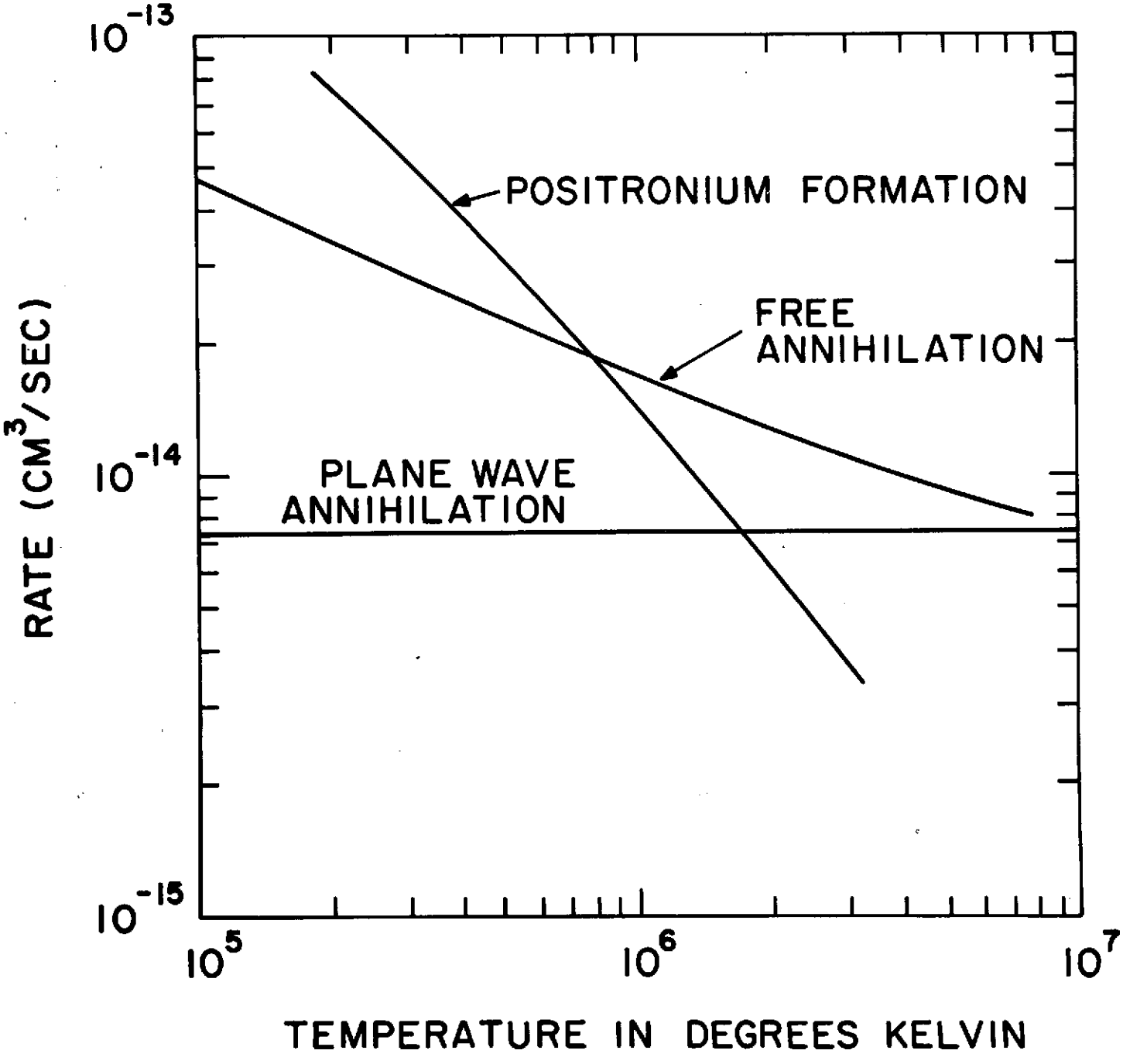
10^{-13}
10^{-14}
10^{-15}
RATE (CM^3/SEC)
POSITRONIUM FORMATION
FREE ANNIHILATION
PLANE WAVE ANNIHILATION
10^5
10^6
10^7
TEMPERATURE IN DEGREES KELVIN

FIGURE 27

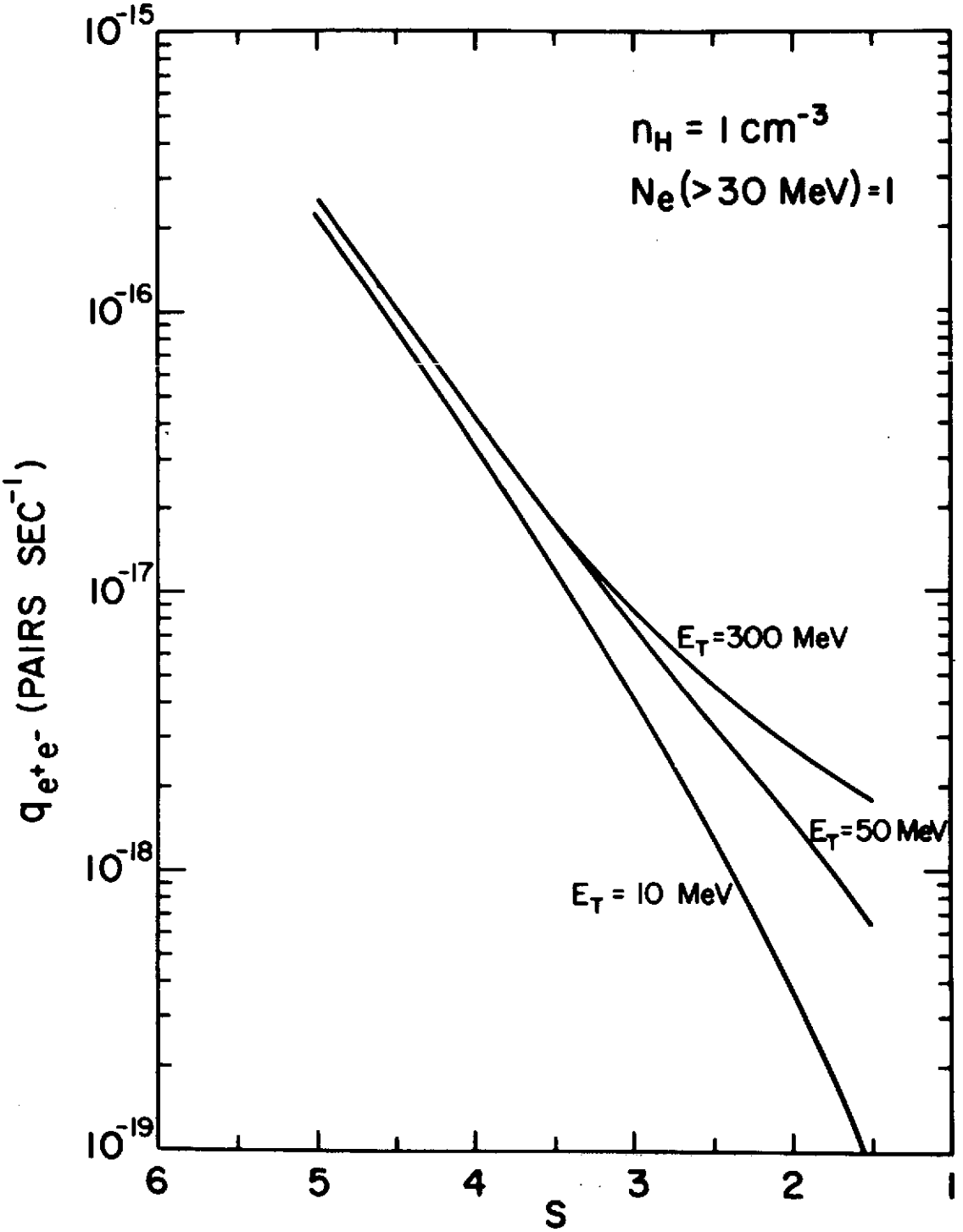
10^{-15}
10^{-16}
10^{-17}
10^{-18}
10^{-19}
$q_{e^+e^-}$ (PAIRS SEC^{-1})
$n_H = 1\ cm^{-3}$
$N_e(>30\ MeV) = 1$
E_T=300 MeV
E_T=50 MeV
E_T = 10 MeV
6
5
4
3
2
1
S

FIGURE 28

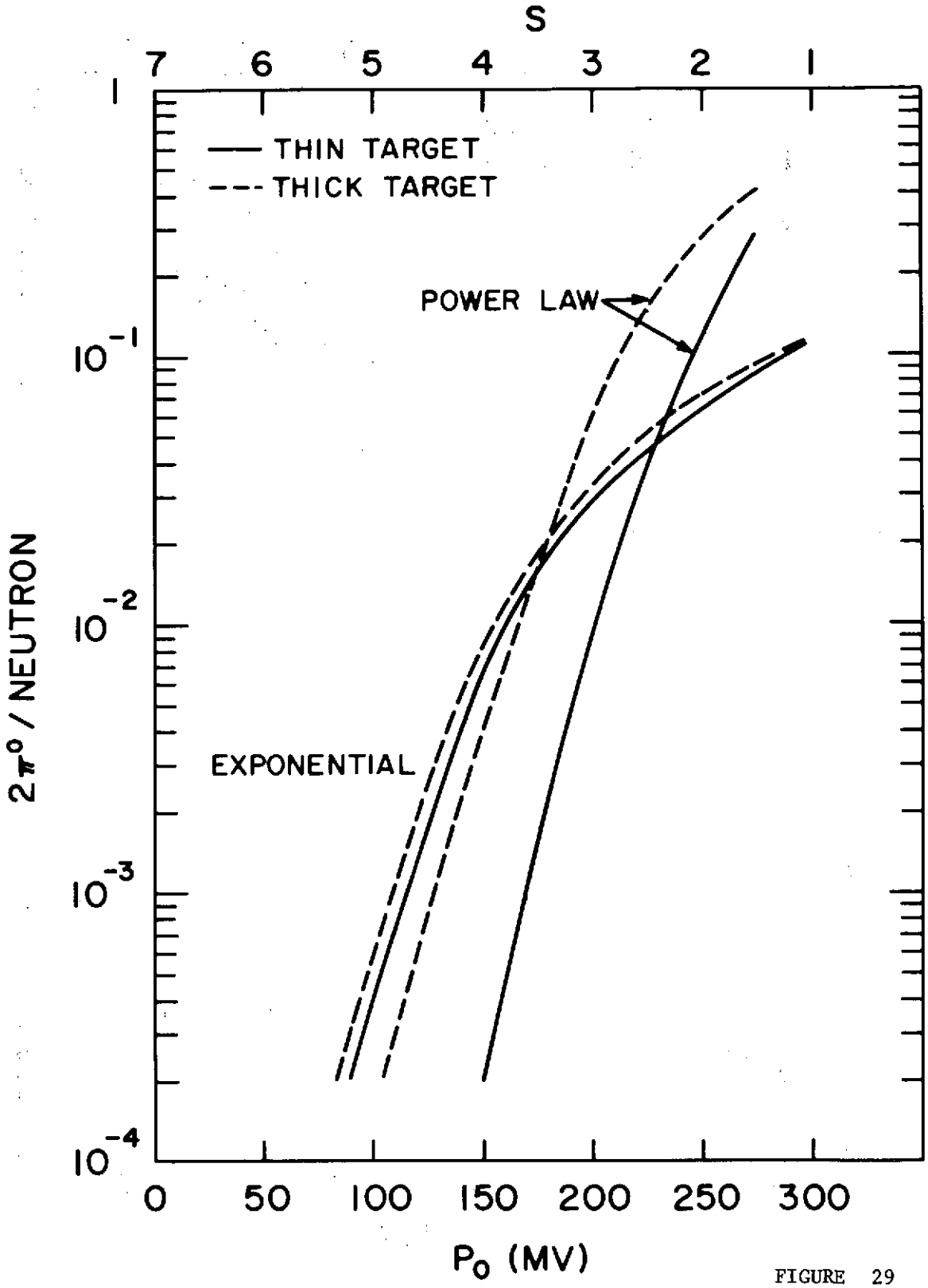
S
7
6
5
4
3
2
1
THIN TARGET
THICK TARGET
POWER LAW
EXPONENTIAL
$2\pi^0$ / NEUTRON
10^{-1}
10^{-2}
10^{-3}
10^{-4}
0
50
100
150
200
250
300
P_0 (MV)

FIGURE 29

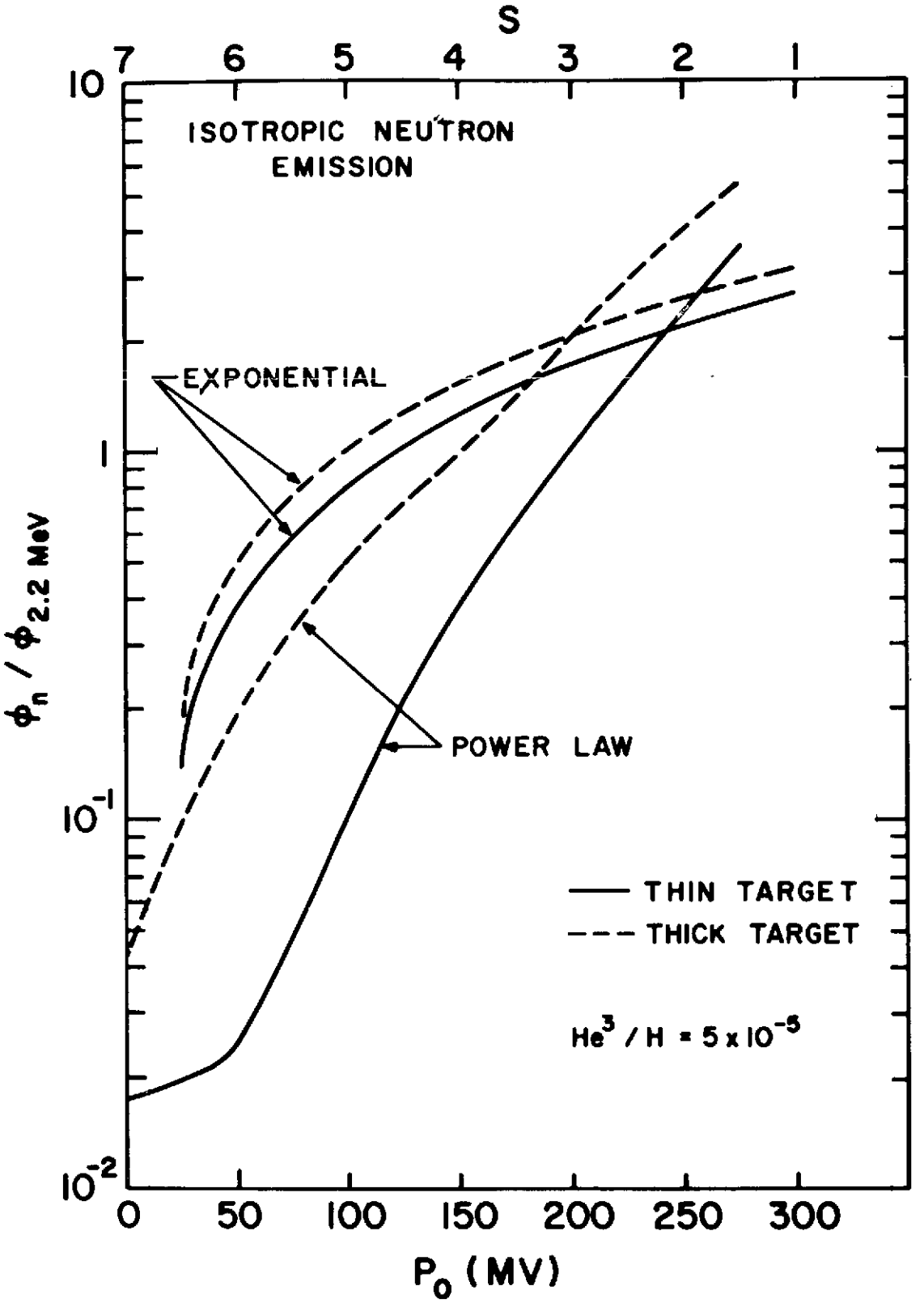
S
7
6
5
4
3
2
1
ISOTROPIC NEUTRON EMISSION
EXPONENTIAL
POWER LAW
THIN TARGET
THICK TARGET
$He^3 / H = 5 \times 10^{-5}$
$\phi_n / \phi_{2.2\ MeV}$
10^{-1}
10^{-2}
0
50
100
150
200
250
300
P_0 (MV)

FIGURE 30